ISSN 1880-8468

Technical Report of
International Development Engineering

国際開発工学報告

TRIDE-2014-05 June 5, 2014

Abstracts of Bachelor Theses
Presented in Feburary 2014

Department of International Development Engineering,
Graduate School of Science and Engineering,
Tokyo Institute of Technology
http://www.ide.titech.ac.jp/TR

Preface

Bachelor theses of Department of International Development Engineering, Tokyo Institute of Technology were presented successfully on August 5, 2013 and February 28, 2014, respectively. This technical report consists of the abstracts of those theses.

Technical Report of International Development Engineering
TRIDE-2014-03b

Table of Contents

(Completing in September 2013)

天然ゼオライトによる重金属の吸着

..... 陳　子和/ Chen Zihe 1

Selective Catalytic Reduction of Nitrogen Oxide by Propene over Ceria-Zirconia

..... Bantan Furat Mohmmedalia 3

有機酸を分解する新規酵母を接種した高速コンポスト化

..... 荒谷 彰吾 5

タケを原料としたエタノール生成のための前処理の効果

..... 松尾 遼 7

鉄筋コンクリートの電着工法に対する鉄およびアルミニウム陽極の適応

..... 平井　雄之 9

(Completing in March 2014)

東京－熊谷間における夏季東京湾海風の年代変化

..... 寝占　祐太 11

Application of Thermal Image Velocimetry to Dust Devil-Like Vortex

..... 張 逸群 13

WRF-CHEMを用いた関東域海風挙動のシミュレーション

..... 三井 智章 15

実都市幾何における三次元熱放射過程を考慮したLES数値解析

..... 吉田 祐麻 17

直接・間接排出に着目した市町村別CO2排出量の可視化

..... 王　旭陽 19

塩害及び中性化におけるフライアッシュを用いた
海水練り鉄筋コンクリートの寿命予測

..... 易　成 21

FOSS GIS の実現可能性の研究：ルアンパバーン世界遺産地域のケース

..... 片桐　隆介 23

ニッケル水素電池におけるパルス充電のduty比及び電流値が
充放電効率に及ぼす影響
..... 高　健太　25

Passenger Characteristics and Mode Choice Competition between High Speed Rail and Air Transport in China
..... 康 書陽　27

タイの工業団地立地に対する交通インフラの影響
..... 齋藤　亘　29

梁集合体のジオメトリが凝着力に及ぼす影響
..... 島原　森　31

干満帯における電気防食を適用した欠陥を有する塗装鋼材の劣化に関する
実験的検討
..... 志村 恭平　33

菜種油・大豆油系廃食油を原料としたバイオディーゼル生成に対する
遊離脂肪酸除去の影響
..... 石 振強　35

開発途上国における鉄道貨物輸送実態の国際比較
..... 祖田 真志　37

湖沼汚泥由来の人工ゼオライトによるクロム（Ⅲ）の除去
..... 高松 貴大　39

Development of motion capture software for simultaneous measurement system of radio channel response and body motion
..... 陳 高超　41

大域的射影変換を用いた画像マッチングに関する研究
..... 陳　陽　43

基礎の沈下によって引き起こされる盛土中央の圧力減少
(Central pressure drop underneath embankments caused by basal settlement)
..... 中村 淳一郎　45

銀イオンによる殺菌効果の定量的評価
..... 日比生 拓也　47

Development of channel sounder with universal software radio platform
(汎用ソフトウェア無線機を用いた電波伝搬測定装置の開発)
..... 閔 天楊 49
温度がシリコンゴムとガラスの弾性接触における凝着ヒステリシスに
及ぼす影響
..... 傅 冠达 51
複雑地形における津波の遡上解析に関する研究
..... 松本 光希 53
給水養生装置の電気化学的補修工法への適用に関する研究
..... 山本　周 55

モンゴル産天然ゼオライトによる重金属の吸着

Student Number: 08B16049, Name: Zihe Chen, Supervisor: Ryuichi EGASHIRA and Hiroaki HABAKI

1. Introduction

The contamination of the acid mine drainage solution by heavy metals has been regarded as a serious issue to cause the water or soil pollution. Natural zeolites have been studied as a potency to remove the heavy metals from the solutions[1,2]. The natural zeolite generally contains some kinds of cations, which might influence the removal efficiency of the heavy metals from the solution. In this study the natural zeolite from Mongol was used as adsorbent, and the effects of the cations in the zeolite on removal of the model heavy metals were studied.

2. Experimental

2.1. Zeolite source

The sample of natural zeolite used was obtained from Tsagaan Tsav deposit in Dornogovi province of Mongolia, which was rich in clinoptilolite and the same zeolite sample as used in the previous studies [1, 2]. The zeolites were crushed, ground and passed through 150×150 μm sieves. Then it was preserved in the desiccators with a saturated aqueous solution of ammonium chloride at the room temperature, defined as the zeolite1. To identify the species of the cations in the zeolite1, 1 g of the zeolite1 was contacted with the 1M ammonium acetate solution of 20×10^{-6} m^3 at 298 K for 10 days, and the obtained solution was analyzed. The zeolite1 of 1 g was treated by contacting with 1M sodium acetate solution of 20×10^{-6} m^3 at 298 K for 10 days, and washed by pure water several times, filtered from water and dried for 1 day, defined as the zeolite2.

2.2. Batch adsorption run

Batch adsorption runs were conducted by mixing 1 g of the zeolite1 or zeolite2 with 20×10^{-6} m^3 of synthetic solutions containing the specified concentrations of heavy metal ions. The conditions of adsorption run are shown in **Table 1**. Copper (Cu), zinc (Zn), and manganese (Mn) were selected as model heavy metals. After equilibration, the obtained solutions were measured to determine the concentrations of the metals in the solutions, which were not only the mentioned heavy metals but also the cations dissolved from the zeolites. The analytical grade reagents of sulfide salts, such as $CuSO_4\cdot5H_2O$, $ZnSO_4\cdot7H_2O$ and $MnSO_4\cdot5H_2O$ (Wako Pure Chemical Industries, Ltd.), were used as the sources of the metals since the mine wastewater generally contains sulfate ions. The aqueous phases were analyzed by ICP-AES (SPS 7800 Series, Seiko Instruments Inc.) to determine the concentrations of the metals.

Table 1 Experimental conditions of adsorption run

Mass of initial solution, L_0 [m^3]	20×10^{-6}
Initial concentration of metals, C_0 [kmol/m^3]	1.5×10^{-3}-1.1×10^{-1}
Mass of initial zeolite, S_0 [g]	1
Contacting time, t [h]	240
Temperature, T [K]	303

3. Result and Discussion

3.1. Cations dissolved from zeolite

In the solution obtained by contacting the zeolite1 and ammonium acetate solution, the species and amounts of metals dissolved from the zeolite1 were listed in **Table 2**. Sodium (Na) calcium (Ca), potassium (K), magnesium (Mg) and strontium (Sr) were detected and the concentration of Na was the largest, followed by Ca, K, Mg and Sr. In the solutions at adsorption equilibrium with the zeolite1, the model heavy metal of Cu, Zn or Mn, and 5 cations of Na, K, Ca, Mg and Sr were detected. When the zeolite2 was used, the same kinds of metals were detected as well.

Table 2 Species and concentrations of cations dissolved from zeolite1 [kmol/kg-zeolite]

Na	K	Ca	Mg	Sr
8.6×10^{-4}	9.6×10^{-5}	2.3×10^{-4}	8.8×10^{-5}	1.6×10^{-5}

Figure 1 shows the effects of the concentration of the heavy metal in the solution on the concentrations of Na for both zeolites, in which the results of Zn were presented as an example. The concentrations of Na increased with the Zn concentration and showed the constant values in the range of C_{Zn}>0.002kmol/m^3. The concentration of Na was larger with the zeolite2 than that with the zeolite1. The operation to contact the zeolite1 with the solution of sodium acetate might be able to exchange some cations in the zeolite1 with Na. This tendency was observed in the cases of Mg and Cu.

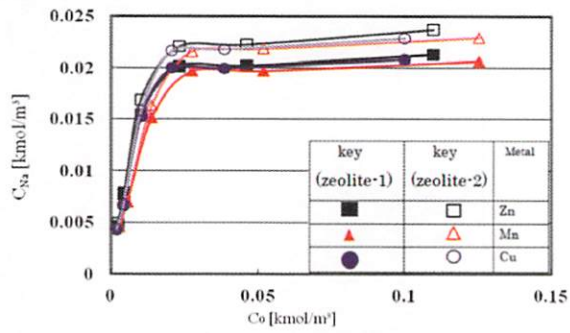

Fig.1 Ion-exchanging isotherm of Na

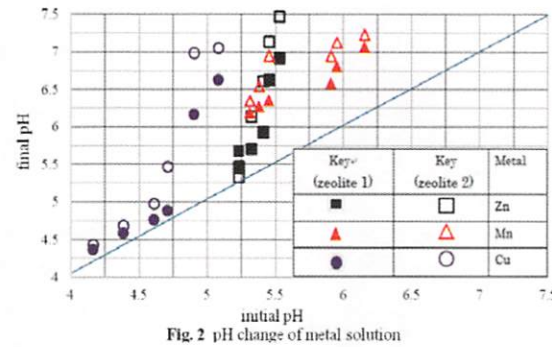

Fig. 2 pH change of metal solution

3.2. pH change

Figure 2 shows the effects of the metal concentrations on the pH at equilibrium. The equilibrium pH was always higher than the initial pH, and decreased with an increment of the metal concentrations. The pH range

increased in the order of the results with Cu, Mn and Zn. The zeolites should adsorb the proton ion to enhance pH and the increment was larger with smaller metal concentration. The pH was higher with the zeolite2 than that with the zeolite1.

3.3. Numerical relationships

The material balance of metal i is represented by,

$$L_0 \cdot C_{i,0} + S_0 \cdot q_{i,0} = L \cdot C_i + S \cdot q_i \quad (1)$$

where L_0, $C_{i,0}$, S_0, $q_{i,0}$, L, C_i, S and q_i are the volume of the initial solution, initial molar concentration of metal i, initial mass of zeolite, mole of metal i per unit mass of zeolite, volume of the solution at equilibrium, molar concentration of metal i at equilibrium, mass of zeolite at equilibrium, and mole of metal i per unit mass of zeolite at equilibrium, respectively. The q_i of each heavy metal was determined by Eq. (2) with the assumptions of $S=S_0$, $L=L_0$, and $q_{i,0}=0$. The yield of metal i, Y_i, was defined as,

$$Y_i = 1 - LC_i / L_0 C_{i,0} \quad (2)$$

The adsorption isotherm of the Langmuir model is expressed as,

$$q_i = q_{m,i} \cdot K_i \cdot C_i / (1 + K_i \cdot C_i) \quad (3)$$

where $q_{m,i}$ is the adsorbed moles of metal i per unit mass of zeolite at saturation, and K_i is the Langmuir constant of metal i.

3.4. Yields of heavy metals

Figure 3 shows the yields of metal i with both of zeolites. The Y_is of all metals simply decreased with an increment of the metal concentrations. In the range of lower metal concentrations, Y_i attained more than 0.9 in all cases. The Y_i of Zn was the largest, followed by Mn and Cu. The Y_i were higher with the zeolite2 than those with the zeolite1.

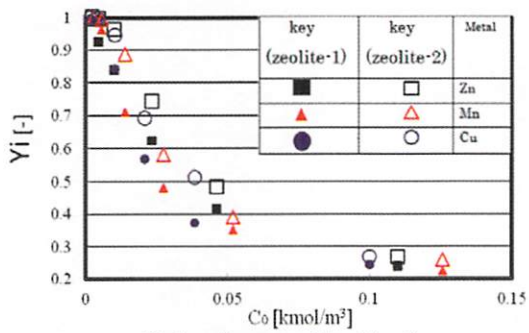

Fig.3 Recovery of Zn , Mn , Cu

3.5.Adsorption isotherm

Figures 4 and **5** show the adsorption isotherms of the heavy metals with both zeolites. Both zeolites adsorbed all kinds of heavy metals. For each zeolite, q_i of Zn was the largest, followed by Mn and Cu. The q_i was larger with the zeolite2 than that with the zeolite1. The measured results were fitted by the Langmuir model to obtain $q_{m,i}$ and K_i, as listed in **Table 3**. The $q_{m,i}$ of Cu was approximately the same as in the previous study[2], however $q_{m,i}$s of Zn and Mn were larger in this study than those in the previous study. This might be caused by the difference in the equilibrium pH. The higher pH should enhance the adsorption of the cations. The pH with Zn was the largest followed by those of Mn and Cu, and pHs of Zn and Mn were larger than those in previous study. The $q_{m,i}$s were larger with the zeolite2 than those with zeolite1. The exchange of cations in zeolite should affect on the adsorption because the divalent cations should generally adsorb more than the univalent cations. Moreover the treatment with sodium acetate solution made the pH larger at equilibrium, causing larger q_i. Then the zeolite2, in which the cations were exchanged by Na, might show higher adsorbability of the heavy metals. However these effects were not so significant and the contribution degrees of these effects were unidentified.

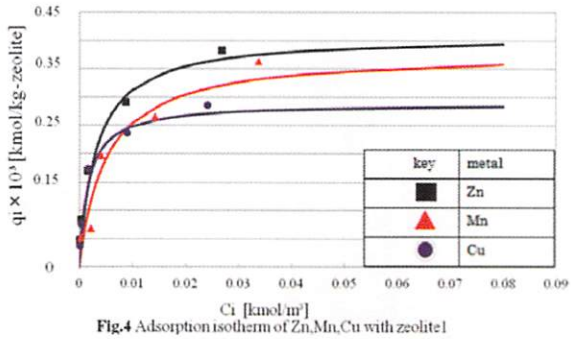

Fig.4 Adsorption isotherm of Zn,Mn,Cu with zeolite1

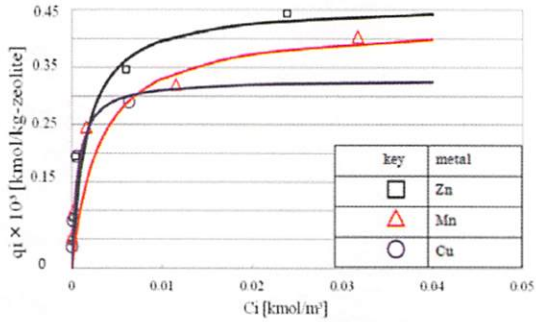

Fig.5 Adsorption isotherm of Zn,Mn,Cu with zeolite2

Table 3 Langmuir parameters for each heavy metal

Zeolite1		Cu	Zn	Mn
$q_{m,i}$	[kmol/kg-Zeo]	2.9×10^{-4}	4.1×10^{-4}	3.8×10^{-4}
$K_{L,i}$	[m³/kmol]	6×10^{2}	3.2×10^{2}	2×10^{2}
Zeolite2				
$q_{m,i}$	[kmol/kg-Zeo]	3.3×10^{-4}	4.6×10^{-4}	4.3×10^{-4}
$K_{L,i}$	[m³/kmol]	1.58×10^{3}	6.2×10^{2}	3×10^{2}

4. Conclusion

The natural zeolite from Mongolia could remove copper, zinc and manganese from the solution. The zeolite treated by the solution of high concentration of sodium acetate could improve its adsorbability of these heavy metals. This might be attributed to the exchange of some cations in the cations with univalent cation of sodium in the zeolite by the treatment. This treated zeolite enhanced the pH in the solution, improving the adsorbability as well. However the effects were not clarified and further study is necessary.

Reference

[1] Bolortamir Ts, *et al.*, *J. Chem. Eng. Japan*, **41**, 1003–1009 (2008)

[2] Egashira R., et al., *J. Chem. Eng. Japan*, **46**, 50–55 (2013)

[3] Motsi, T.*et al. Int. J. Miner. Process*, **92**, 42–48 (2009)

[4] Web site "Database of Zeolite Structures" http://www.iza-structure.org/databases/

[5]American Mineralorgist,Volume 86,page 431-437.2001

プロペンを還元剤とした CeO_2-ZrO_2 複合触媒による NO 選択還元

学籍番号：08-20000　氏名：バンタン フラート　指導教官：日野出 洋文

１　はじめに

高い燃料効率及び CO_2 の低排出ガスを有するディーゼルエンジンが未来の輸送およびリモート発電似広く使われていると予測する[1]。しかし、酸性雨や光化学スモッグの原因物質の一つであるリーンバーンエンジン排気中の NOx の低減が大きな課題である。さまざまな対策方法の中に、炭化水素による NOx の選択還元触媒（HC-SCR）が同時に NOx と未燃炭化水素を除去することができ移動発生源に由来する窒素酸化物を除去するために効果的かつ経済的な技術であることが証明されている。現在のパフォーマンスは、特に商用アプリケーションでは、その低温領域での性能は十分ではないため、希薄燃焼条件下での C_3H_6-SCR は、過去数十年の間に大きな注目を集めている。HC-SCR 反応が、NO_2 生成反応及び NO_2 と炭化水素の反応によって進行しているという機構が多くの研究者によって提案されている［2]。

上記の課題を解決するために CeO_2-ZrO_2 複合触媒の NO 選択還元に対する活性を本研究のテーマとして調べられた。CeO_2 は無害で経済的な材料であり、酸素貯蔵物質として注目されている。CeO_2 の存在により、NO から NO_2 への酸化反応を促進し、NO の還元性が増加させると報告された。ZrO_2 の CeO_2 への添加によって低温領域での CeO_2 の酸素貯蔵能力、酸化還元性、耐熱性、優れた触媒活性を向上させる[3]。

２　触媒調製および実験

触媒は２つの方法によって調製した：①機械的混合法、②共沈法である。機械的混合法では、JRC-ZRO-（３，５，６）と JRC-CEO-（１，２）の５つの触媒を前駆体として使った。５つの前駆体を５５０℃で焼成してから、各触媒の活性実験が行われた。その結果を基づいて、機械的混合法に使用された触媒は JRC-ZRO-６と JRC-CEO-（１，２）であった。１対１の質量比で JRC-CEO-1 と JRC-ZRO-6（以下 CeO_2(1)-ZrO_2(6)で省略）と１対１の質量比で JRC-CEO-2 と JRC-ZRO-6（以下 CeO_2(2)-ZrO_2(6)で省略）を混ぜた（上記の触媒を混ぜるにはエタノールを使用した）。共沈法では、硝酸ジルコニル二水和物 $ZrO(NO_3)_2 \cdot 2H_2O$(Wako)と硝酸二アンモニウムセリウムⅣ $Ce(NH_4)_2(NO_3)_6$（Kanto Chemical）が前駆体として使用し、同じモル比で混ぜた。硝酸ジルコニル二水和物を 70ml のイオン交換水に溶解して、pH を 0.5～1.0 に調整するために HNO_3 溶液を添加した（硝酸二アンモニウムセリウムⅣ の粒子が均一に溶解するために、pH を調整する必要がある）。その後、硝酸二アンモニウムセリウムⅣを溶解し、溶液中に最終的に 9～11 の pH を調整する NH_3 溶液を添加する。各調製工程は、30 分の攪拌時間が必要である。さらに、ビーカーの上に配置する時計皿により、溶媒の蒸発を防止した。空気中で 8 時間の熟成をした後、時計皿を取り外して、イオン交換水を用いて加水分解を行った。乾燥のための前処理として濾過（真空フィルタリング）を行った。次いで試料を 100℃で約 8 時間乾燥した。乾燥した触媒をメノウ乳鉢で粉砕し、電気炉で焼成するために焼成ボートに詰められる。焼成は、空気雰囲気下 550℃で 4 時間行った。共沈法の触媒の結果は($Zr_{0.5}Ce_{0.5}O_2$)である。焼結現象があるので、焼成後の触媒は、乳鉢で再び粉砕した。出来上がった全て混合サンプルが粉砕した後、 円形ペレット触媒に成形されて、篩いを用いて触媒の粒径が、0.71～1.00 ミリメートルに調整されている。機械的混合法の場合では、焼成前と焼成後の触媒の活性を比較するために、焼成前と焼成後の活性実験を行った。

活性実験は固定床流通反応装置で行われた。反応ガスは、1500ppm の NO、10％の O_2、1500 ppm の C_3H_6、及び He をバランスガスとしてから構成されていた。0.9～1.4g の触媒に 13000 h^{-1} の空間速度（約４mL/s の総ガス流量）を流した。温度は 150～550℃まで段階的に変更した。NO と NO_2 濃度は、窒素酸化物分析計（島津製作所、NOA-7000）によ

って分析された。N_2O 分析は、ガスクロマトグラフ（GL サイエンス、GC-323w）を用いて、CO_2 および CO 分析には、ガスクロマトグラフ（GL サイエンス、GC-390）が使用された。触媒を評価するために、TG -DTA、XRD、窒素吸着（オートゾーブ 1MP/ TSU、BET 分析）が使用された。

3 結果と考察

図 1 では、機械的混合法の前駆体によって NO から N_2 への還元活性実験結果を示している。その中で最も活性の高い触媒は JRC-ZRO-6 であった。その結果を基づいて、JRC-ZRO の前駆体の中から JRC-ZRO-6 を選択した。一方、JRC-CEO はほぼ同じ結果を示したため、両方を試すことにした(以下の図で BC:焼成前、AC:焼成後の意味を示している)。

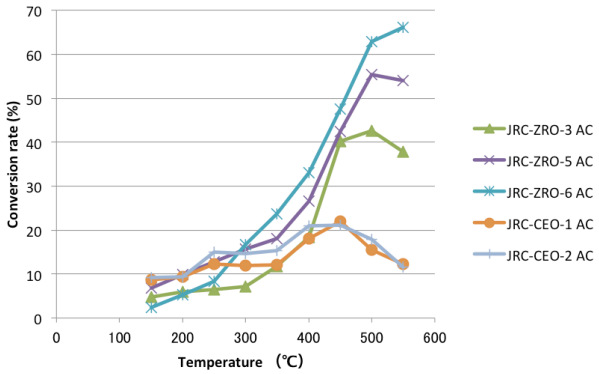

図 1 機械的混合法の前駆体のプロペンを還元剤としての NO から N_2 への還元活性実験結果

図 2 では機械的混合法および共沈法によって調製された触媒の NO から N_2 への還元活性実験結果、図 3 では 2 つの方法によって調製された触媒の C_3H_6 から CO_2 への酸化活性実験結果を示している。両図では焼成後の $CeO_2(1)$-ZrO_2 (6)が最も高い活性を表している。他の機械的混合法の触媒はほぼ同じ結果を示しているが、共沈法の触媒は NO から N_2 への還元活性の最も低い活性を表している。それらの結果から、共沈法によって、ジルコニアの NOx 還元に対する活性が低下すると考えられる。一方、機械的混合法の触媒は比較的に高い活性を示したが、混合比の調整によって活性がより向上できると考えられる。焼成前後のデータを比較すると、焼成も触媒活性に影響することが分かった。

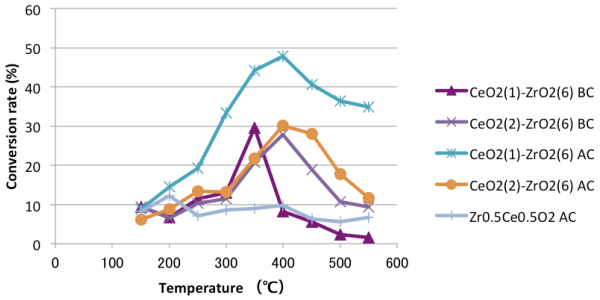

図 2 機械的混合法及び共沈法のプロペンを還元剤としての NO から N_2 への還元活性実験結果

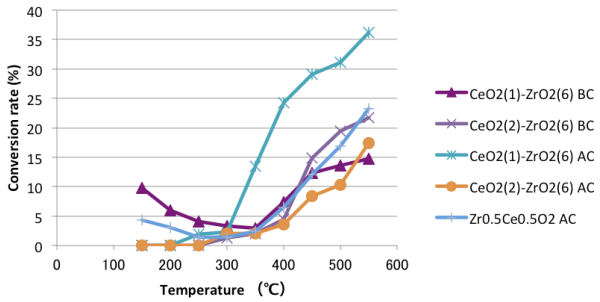

図 3 機械的混合法及び共沈法のプロペンを還元剤としての C_3H_6 から CO_2 への還元活性実験結果

4 結論

機械的混合法で調製した触媒がプロペンを還元剤としてセリア-ジルコニアによる NO から N_2 への選択還元を示した。 機械的混合法が共沈法より高い活性を表した。機械的混合法の中では $CeO_2(1)$-$ZrO_2(6)$ が最も活性の高い触媒であった。その理由としては、焼成や比率の影響があると予測されている。比率を変化することによってさらなる高い活性が得られると思われている。

参考文献

[1] Jie Liu, Environ. Sci. Technol., 47, 4528 (2013)
[2] R.Burch, T.C. Watling, Appl.Catal.B, 11, 207 (1997)
[3] S.Matsumoto, Catalysis Today, 90, 3-4, (2004)

High-speed composting by inoculation of novel yeast that degrades organic acids

Student Number: 09-00962 Name: Shogo ARAYA Supervisor: Kiyohiko NAKASAKI

1 Introduction

Managing the ever-increasing waste materials produced in our society has become an essential area of study in recent years. Among waste materials, organic fractions such as food waste originating from households, restaurants, and food processing factories can be reclaimed as compost for agricultural use. One of the significant characteristics of food waste composting is that the pH decreases in the early stages of composting, and it is well known that the low pH inhibits vigorous organic matter degradation in the composting.

In this study, a yeast strain RB1, which has a high ability of degrading organic acids, was used as an inoculum in order to prevent the decrease in pH and to accelerate organic matter degradation.

2 Materials and methods

2-1 Compost material and composting operation

Commercial rabbit food was used as a representative model of food waste so that reproducible data could be obtained. The rabbit food, sawdust, and seeding material were mixed at a ratio of 10:9:1 and 4 types of organic acids characteristically contained in food waste (acetic acid, propionic acid, butyric acid, and lactic acid) were added to create a raw compost mixture. The concentration of organic acids in the raw compost mixture was adjusted by referring to the previous study [1]. Two types of composting experiments were performed. Run A included inoculation of the compost with a yeast strain RB1, which has a high degradation activity against organic acids, and Run B was the control composting without inoculation of RB1. At the start of both experimental runs, the moisture content was adjusted to 60% by addition of distilled water. Initial temperature was at around 27°C, and after temperature reached to 60°C by self-heating due to organic matter decomposition, 60°C was maintained by the increase or decrease in air flow rate. The period of composting was set at 10 days. The concentration of CO_2 in the exhaust gas from the reactor was measured continuously, and with air flow rate at that time, the CO_2 evolution rate and the conversion of carbon corresponding to the rate of organic matter decomposition were quantified.

2-2 Physicochemical analyses

The compost samples collected at days 0, 1, 2, 3, 4, 5, 6, 7, and 10 were measured for pH, moisture content, and concentration of organic acids. The concentration of organic acids was determined using a high pressure liquid chromatography (HPLC) system equipped with a UV monitor.

2-3 Microbial analysis of compost samples

A dilution plating method was used to determine the cell density of bacteria and yeasts, including that of the RB1 strain inoculated into the raw compost material.

The microbial community in the compost samples was determined by denaturing gradient gel electrophoresis (DGGE) analysis [2]. In the DGGE analysis, bacterial 16S rRNA gene fragment was used. Characteristic bands in the DGGE gel were excised and base sequences of the DNA contained in the bands were determined.

3 Results and discussion

3-1 Time course of composting

The effect of inoculation on composting is shown in Fig. 1, which illustrates changes in temperature, pH, and conversion of carbon during the 10-day composting period. In Run A, temperature immediately increased after the start of composting and reached to 60°C at day 2. The pH also increased from the beginning, and finally leveled off at approximately pH 8.5. In contrast, temperature started to increase after the turning of day 2 and reached 60°C by day 4 in Run B, and the pH of Run B only began to rise at day 2 of composting, finally reaching a pH of 8.5 by day 8. Both temperature and pH of Run A increased faster than those of Run B, which indicated that strain RB1 effectively increased the temperature and pH in the early stages of composting. The conversion of carbon was used to better understand the amount of organic matter degraded. The conversion of carbon for Run A rose faster than that for Run B by about 2 days, but the difference in the conversion of carbon between Run A and Run B became small in the later stages, suggesting that the effect of inoculation with RB1 was more significant at the start of composting.

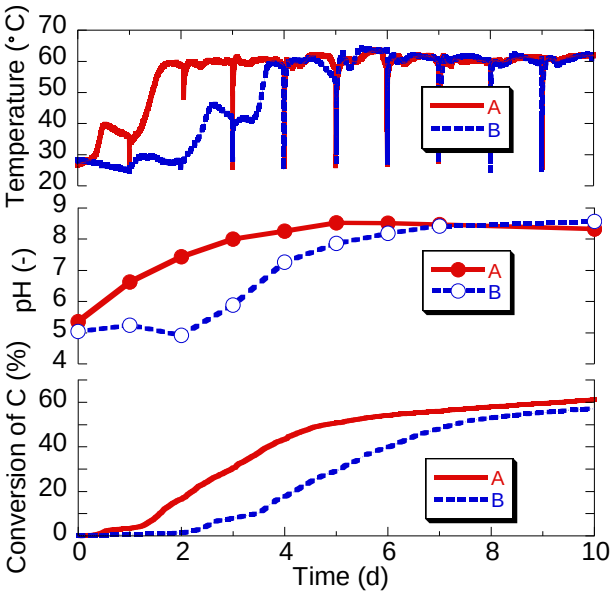

Fig. 1 The courses of temperature, pH, and conversion of carbon during composting for Run A (inoculated) and Run B (control).

Organic acids degradation during composting under both conditions is shown in Fig. 2. In Run A, acetic acid, propionic acid, and lactic acid were instantly degraded after the start of composting, though butyric acid degradation was delayed by approximately 1 day. For the control composting, acetic acid and lactic acid degradation began at day 2 after initiation of composting, whereas a decrease in propionic acid and butyric acid was observed after 3 days of composting. The reason for the delayed degradation of propionic acid may be that propionic acid is a fatty acid with an odd number of carbons, and that of butyric acid may be that butyric acid was degraded through acetic acid by β-oxidation. As mentioned above, the ease of degradation depended upon the types of organic acids; however, all acids were

completely degraded in both composting conditions by the end of the 10-day composting period. The pH increase during composting corresponded well with the observed changes in organic acids concentrations in the early phase of composting. In the middle phase of composting, the pH continued to increase even after the organic acids diminished. This was likely due to the production of alkaline substances such as NH_3 that is associated with protein degradation that occurs during composting.

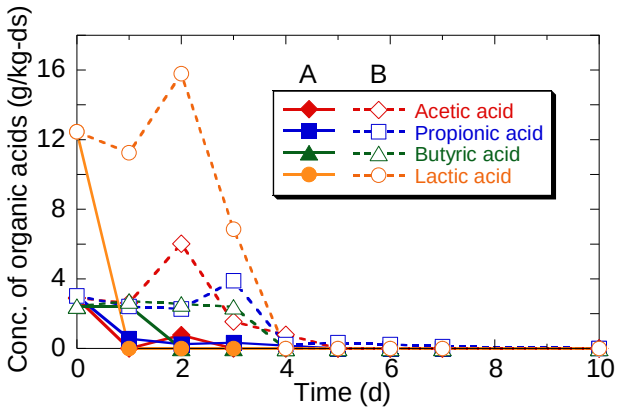

Fig. 2 The courses of concentration of organic acids during composting for Run A (inoculated) and Run B (control).

3-2 Microbial succession

The growth curves of yeast and mesophilic and thermophilic bacteria during composting for Run A and Run B are shown in Fig. 3. In Run A, the cell density of yeast, which is mainly RB1, initially proliferated rapidly and then drastically decreased to non-detectable levels by day 2 of the inoculated compost. The rapid decrease of RB1 corresponded to the increase of composting temperature, suggesting that 60 °C is too high for the RB1 strain to survive. The rapid growth of RB1 coincided closely with the decrease in organic acids; hence, this finding suggests that RB1 contributed to the degradation of the organic acids in the raw compost material.

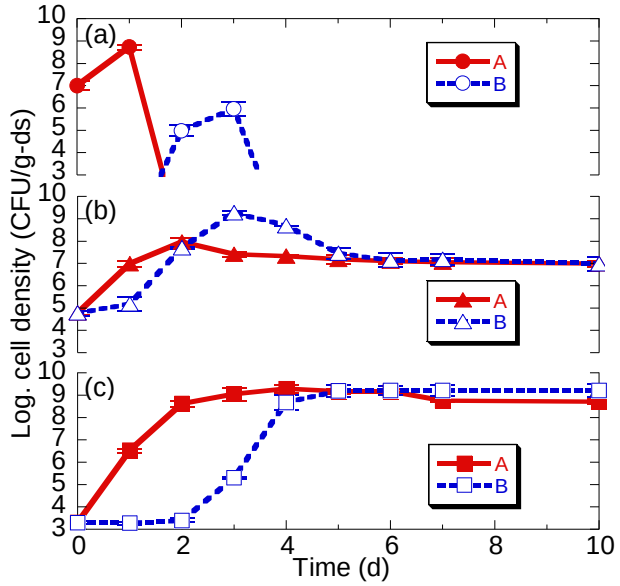

Fig. 3 The courses of cell density for yeast (a), mesophilic bacteria (b), and thermophilic bacteria (c) during composting for Run A (inoculated) and Run B (control).

Mesophilic and thermophilic bacteria proliferated faster in Run A than Run B. From these results, it is proposed that the role of RB1 in the compost was to degrade organic acids, thus adjusting the environmental conditions to promote the growth of other microorganisms that contribute to organic matter degradation.

3-3 Changes in bacterial community

The dynamic changes in a bacterial community determined by the DGGE fingerprint during composting process are shown in Fig. 4. It was observed that, except for bands 1, 2, and 3, the bands with high light intensity for both composting conditions, such as band 4, 5 (12), 6, 7, 10, and 11 (13), were similar when the temperature was increased to 60 °C. These results suggest that the microorganisms dominant during the thermophilic stages of composting with RB1 inoculation were also dominant during composting without RB1 inoculation. The RB1 inoculation may have accelerated the proliferation of those bacteria by adjusting the environmental conditions to optimize their growth.

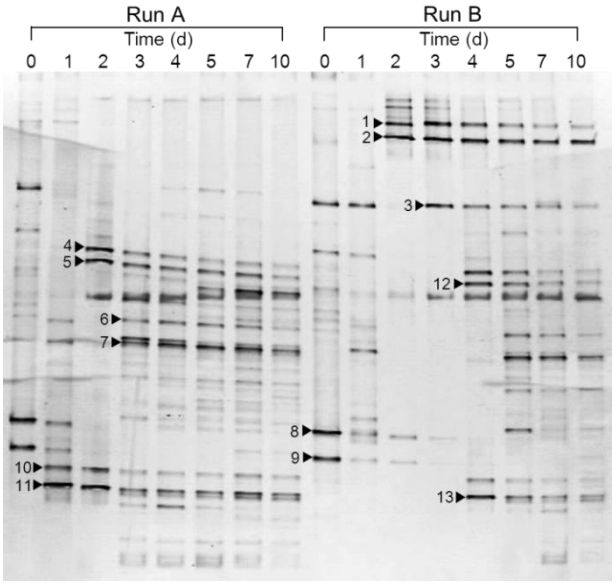

Fig. 4 PCR-DGGE fingerprint during composting for Run A (inoculated) and Run B (control).

4 Conclusions

The inoculation of yeast strain RB1 accelerated the degradation of organic acids present in the raw compost material, thus both mesophilic and thermophilic bacteria proliferated faster in the compost with RB1 inoculation than in that without inoculation. RB1 cells died with increase in temperature, and this affected the early stages of composting prior to the thermophilic stage. The RB1 strain accelerated the composting process by at least 2 days by eliminating the initial lag phase seen in the growth of other microorganisms.

References

[1] Sundberg, C., et al.: Characterisation of source -separated household waste intended for composting, Bioresour. Technol., **102**, 2859-2867, (2011)

[2] Kuok, F., et al.: Effects of turning on the microbial consortia and the in situ temperature preferences of microorganisms in a laboratory-scale swine manure composting, Bioresour. Technol., **116**, 421-427, (2012)

The effects of pretreatments for bioethanol production from bamboo

Student Number：09-22001　Name：Ryo MATSUO　Supervisor：Kiyohiko NAKASAKI

1 Introduction

Increasing world-wide concern regarding petroleum shortage and carbon dioxide emission has resulted in greater demand for alternative energy sources. As one of the promising sources of sustainable energy, bioethanol has attracted attention in recent years. Although the ethanol production from edible biomass, such as cornstarch and sugarcane, has been highly developed and is currently being employed, this technology of bio-ethanol from agricultural production does not solve the issue of food competitiveness and the development of ethanol production from inedible biomass has been required.

Because of its fast growth, bamboo is a promising biomass resource [1]. Furthermore, overgrowing of bamboo in private fields is problem in Asia, and efficient use of bamboo is necessary for its disposal as well. Therefore, the use of bamboo as the raw material of bioethanol is useful.

In this study, we investigated the effect of pretreatment on bamboo for efficient saccharification and ethanol production, and applied Electric beam (EB) and Microwave (MW) irradiations as pretreatment methods.

2 Materials and methods

2-1 Pulverization of bamboo

Moso bamboo, which is obtained in Shizuoka, Japan, was used as a raw material for ethanol production. Bamboo was pulverized into fine powder that has an approximately 50 μm of average particle size using a grinder (PA-C, Marudai Co.).

2-2 Electron beam and microwave irradiations

In order to enhance the efficiency of saccharification, bamboo powder was further treated by electron beam and microwave irradiations.

In the EB irradiation pretreatment, 50 milligrams of bamboo powder was added to 180μL of 18.6% hydrogen peroxide, and irradiated with accelerated electrons at 90 kV, 200 mA for 5 min by using an electron beam irradiator (EB-engine, Hamamatsu photonics K.K.). Irradiated sample was put in a microtube with 500 μL of ultrapure water. As the control experiment, bamboo powder added to 180μL of hydrogen peroxide was placed at room temperature for 5 min. Both the bamboo powder samples in the hydrogen peroxide with and without irradiation of the electron beam were added to 500μL of ultrapure water in the microtubes, and were stored at -30℃.

In the MW pretreatment, 1gram of bamboo powder was put into a microwave reactor with 10 mL of distilled water. The reactor was irradiated and heated using microwave (Wave magic, EYELA). The heating temperature was varied at 180, 190, and 200℃, and each temperature was maintained for 10, 20, and 30min. The concentration of 5-HMF and furfural in the supernatant of processed samples were determined using a HPLC with UV monitor.

2-3 Saccharification of pretreated bamboo powder

The enzyme used for the saccharification of bamboo powder was Meicerase (CEPB-5394, Meiji Co., Ltd.), which was derived from *Trichoderma viride*. The pretreated bamboo powder was added to 0.1M citric acid buffer solution with the pH adjusted to 5.5. The mixture was sterilized by autoclaving at 121℃ for 20min. The filter sterilized Meicelase solution was then added to the mixture, and the concentrations of bamboo and Meicelase were adjusted to 20 and 1 g/L, respectively. Saccharification was conducted at 35℃ for 96 h. The concentrations of glucose after saccharification were determined using a HPLC system equipped with RI monitor.

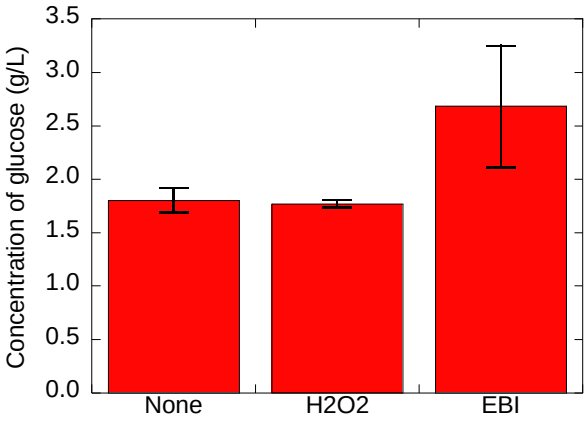

Fig. 1　The glucose concentration after the liquid-state saccharification of bamboo fine powder which are non-pretreated, hydrogen peroxide pretreated and Electron Beam Irradiation pretreated (n=3)

2-4 Simultaneous saccharification and fermentation of microwave pretreated bamboo powder

Simultaneous saccharification and fermentation (SSF) was carried out using bamboo powder pretreated by microwave at 190℃ for 30 min. In order to maintain the high activity of the yeast, culture broth containing yeast extract and polypepton was put to microwaved bamboo powder after washing with distilled water. Filter sterilized Meicelase solution and *Saccharomyces cerevisiae* precultured on YM agar plate at 30℃ for 36h, were then added to the mixture, and the concentrations of bamboo, yeast extract, Polypepton, and Meicelase were adjusted to 300, 3, 5, and 15g/L, respectively. SSF was conducted at 35℃ for 96 h, and the concentrations of glucose and ethanol were determined using the HPLC with RI monitor.

3 Results and discussion

3-1 Effects of electric beam irradiation

The concentrations of glucose after 96-h saccharification of bamboo powder with and without electron beam irradiation were compared in Fig. 1. The concentrations of glucose produced from the bamboo powder without pretreatment, hydrogen peroxide pretreated bamboo powder, and electron beam pretreated bamboo powders were 1.80, 1.77, and 2.69

g/L, respectively. The concentration of glucose produced from electron beam-pretreated bamboo powder was higher than that from both the bamboo powder without pretreatment and hydrogen peroxide-pretreated bamboo powders. The result indicates that electron beam pretreatment promotes following saccharification.

3-2 Effects of microwave

The concentrations of glucose after 96-h saccharification of bamboo powder pretreated by microwave irradiation with different conditions were compared in Fig. 2. Microwave pretreatments in all the conditions examined were effective for the enhancement of saccharification, and the concentrations of glucose were higher than that of non-treatment. Especially in the cases of 190℃30min and 200℃ 30min, the effect of the pretreatment on bamboo was high. The changes of the processing time did not result in the remarkable difference in the concentration of glucose at all the temperature conditions examined. Compared to concentrations of glucose at 190℃ and 200℃, those of 180℃ were lower by 1g/L at least. On the other hand, the concentrations of glucose at 190℃ and 200℃ did not differ significantly each other. Therefore the effect of the microwave depended on the temperature changes more than time changes, especially from 190℃.

Compared to EB irradiation, MW irradiation attained higher glucose concentration. Therefore, for the following fermentation, the bamboo pretreated by microwave at 190℃ for 30 min was chosen for ethanol production.

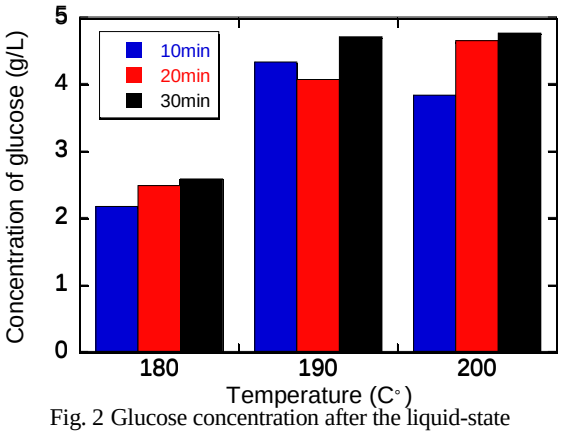

Fig. 2 Glucose concentration after the liquid-state saccharification of bamboo fine powder pretreated by microwave

3-3 The detection of Inhibitors

It was known that intense pretreatment leads to the generation of inhibitors against the growth of a microorganism such as 5-HMF and furfural which are decomposed substances of glucose and xylose. It has already been investigated that yeasts could be inhibited by 5-HMF and furfural in the previous study [2]. Therefore the concentrations of inhibitors in supernatant of bamboo sample after the irradiation by MW at 190℃ for 30min was determined. The concentration of 5-HMF and furfural were 0.65g/L and 2.16g/L. Fig. 3 shows the concentration of glucose after saccharification of bamboo fine powder which is pretreated by microwave at 190℃ for 30 min and the proportion of glucose which comes from liquid or solid were calculated. The concentration of glucose originated from liquid is low, so it was considered that high ethanol production could be still obtained without glucose produced from liquid fraction.

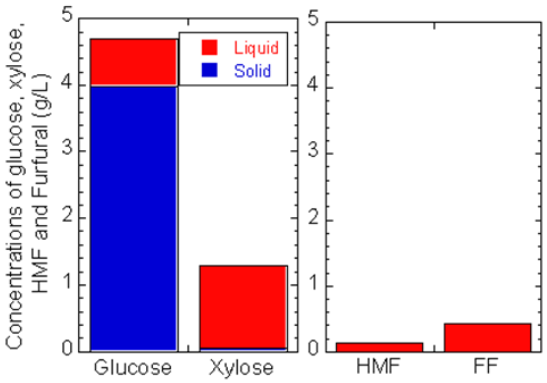

Fig. 3 The glucose, xylose, 5-HMF and furfural concentrations after the saccharification of bamboo fine powder pretreated by microwave at 190℃ for 30 min.

3-4 SSF of pretreated bamboo fine powder

The courses of concentrations of glucose, xylose and Ethanol during SSF of microwave pretreated bamboo fine powder at 190℃ for 30min. Although small amount of glucose remained after 96h, the ethanol concentration was 24.8 g/L. the application of SSF was effective for producing high concentration of ethanol.

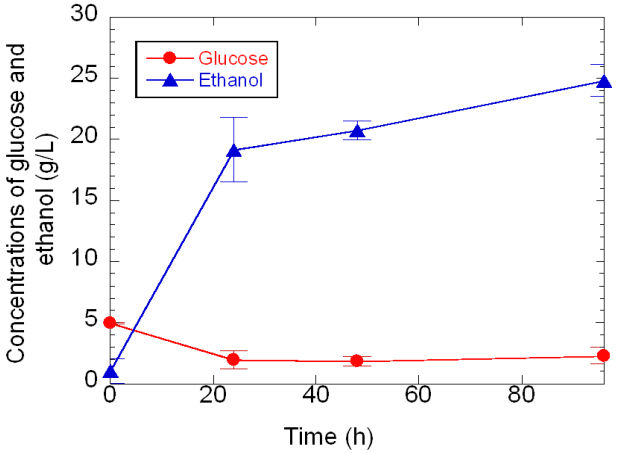

Fig. 4 Courses of concentrations of glucose and Ethanol during Simultaneous Saccharification and Fermentation (SSF) of microwave pretreated bamboo fine powder (n=3)

4. Conclusion

In this study, high concentration, 24.8g/L, of bioethanol was produced by using SSF of bamboo fine powder which is pretreated by microwave at 190℃30 min.

References

[1] Scurlock, J. M. O., D. C. Dayton, and B. Hames. "Bamboo: an overlooked biomass resource?." *Biomass and bioenergy* 19.4 (2000): 229-244.

[2] Lee, Hawon, et al. "Tolerance of Saccharomyces cerevisiae K35 to lignocellulose-derived inhibitory compounds." *Biotechnology and Bioprocess Engineering* 16.4 (2011): 755-760.

Application of Fe or Al as External Electrode in Electrodeposition Method for Reinforced Concrete

Student number: 09-19909 Name: Yuji HIRAI Supervisor: Nobuaki OTSUKI

1. Introduction

Nowadays the deterioration of RC structures is widely reported. So it is necessary to maintain or manage these structures to use for long time. Repair of cracks is important from the view point of durability of RC structures. For that purpose electrodeposition method is one of the most effective repair methods. By this method the filling of cracks and reforming of concrete surface with electrodeposition product of chemical compounds can be achieved.

Electrochemical Repair method such as electrodeposition method has high effective features that overcome disadvantages of conventional repair methods, such as injection, surface sealing and local repair method.

On the other hand, high construction cost is a big issue of electro chemical repair methods. About half of the cost is for Ti mesh which is used as external electrode. Therefore, in this study, in order to solve this problem, the application of Fe or Al as electrode is investigated; since Fe and Al are more economic (about 1/10 times) than Ti mesh and easy to construct.

Based on these backgrounds, the objective of this study is set as follows: usage of Fe or Al electrode for electrodeposition method. Furthermore, to achieve this objective, these 3 subjects are investigated as follows.

(1) Deposition situation based on surface covering rate, and deposition depth.

(2) Resistivity against Cl^- penetration based on NaCl water immersion test.

(3) Resistivity against cracking based on bending test.

2. Experimental Procedure

2.1 Specimen

Mortar specimens (40×40×160mm) were casted with ordinary portland cement; w/c is 0.5 and s/c=2.5. Steel rebar was embedded with 15mm mortar cover. Crack of 0.4±0.1mm wide was induced in specimen along the rebar.

2.2 Electrodeposition Method

Electrodeposition method was performed on these mortar specimens for 14days with a 2.0A/m^2. The device consisted of external electrode (anode), external solution, rebar in mortar specimen (cathode) and DC power supply, as shown in **Fig 1.** Electrodeposition conditions are shown in **Table 1.**

3. Results and discussion

3.1 Deposition state

3.1.1 Deposition state on mortar surface and inside the crack

Deposition state on mortar surface based on surface covering rate, and inside the crack based on deposition depth were investigated respectively.

The results of surface covering rate and deposition depth are shown in **Fig. 2** and **Fig. 3.**

From these results, electrodeposition method using Fe or Al electrode showed almost same or higher repairing effect to induce deposition products than conventional method using Ti mesh. Especially when Fe or Al electrode is used with Mg-ace solution the method showed highest performance about deposition state

3.1.2 Chemical analysis (X-RD) electrodeposits property

Chemical compound deposited on surface of specimen was removed and analyzed by X-RD. From the result, it is estimated that when deposition compound consists of $Mg(OH)_2$ and $MgAl(OH)_{14!}xH_2O$ it shows high performance about deposition situation.

3.1.3 Elution situations of Fe or Al electrode during 14 days charging

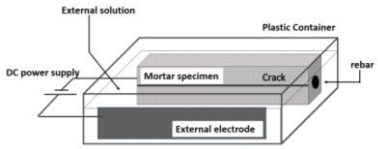

Fig 1.Device

Table 1. Electrodeposition Condition

naming	Fe 1.	Fe 2.	Fe 3.	Al 1.	Al 2.	Al 3.	***Ti
electrode	Fe	Fe	Fe	Al	Al	Al	Ti
solution	*M	**MA	W	M	MA	W	M

*M: Mg Acetate [$Mg(CH_3COO)_2$ [0.1mol/L]]
*MA: Mg Acetate + Aluminum compound
[$Mg(CH_3COO)_2$ [mol/L]+Al2(OH)5Cl・nH2O [0.1mol/L]]
***Conventional Condition

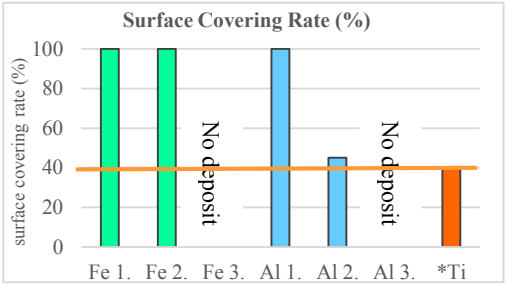

Fig 2. Surface Covering Rate

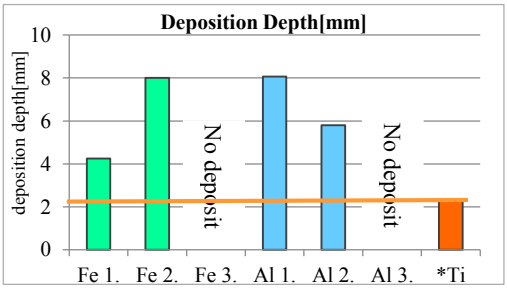

Fig 3. Deposition Depth

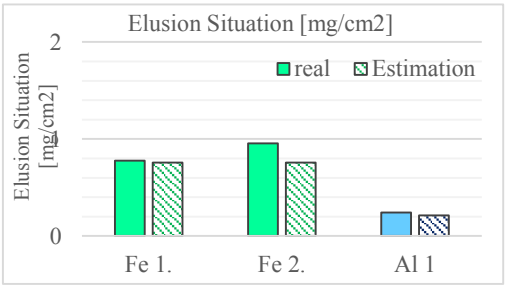

Fig. 5 Cl- penetration depth [Inside Crack]

To evaluate the elution situation, elution amount was investigated and compared to estimation which was calculated from integrated current.

The results are shown in **Fig 4.** From the result it can be said that the amount flown out was significantly small that these electrodes have enough durability during 14 days charging. And these amount can be estimated by calculation.

3.2 Resistivity against Cl^- penetration

To evaluate resistivity against Cl^- penetration of mortar specimen repaired with electrodeposition method using Fe or Al electrode, NaCl immersion test was conducted. After charging for 14days, specimens were immersed into 10% NaCl water for 7 days, then Cl^- penetration depth and amount of Cl^- ion around rebar were investigated.

(1) Cl^- penetration depth

Cl^- penetration depth was evaluated by silver nitrate spray test. When Cl^- exists, silver nitrate changes to silver chloride, then surface color becomes white. The length from surface to boundary line of the change of color is defined as Cl^- penetration depth.

The results are shown in **Fig 5.** From the result, it is clarified that electrodeposition method using Fe electrode with Mg-ace + aluminum compound solution or Al electrode Mg-ace solution have high repair effect to improve resistivity against Cl^- penetration.

(2) Amount of Cl^- ion around rebar

The results are shown in **Fig 6.** From the result, it is clarified that electrodeposition using Fe electrode with Mg-ace solution have higher performance to improve protection from corrosion. Mg-ace+ aluminum compound solution or Al electrode

3.3 Resistivity against cracking

Resistivity against cracking of mortar specimen repaired with electrodeposition method using Fe or Al electrode was evaluated based on bending test.

The results are shown in **Fig 7.** From the result it is confirmed that electrodeposition method using Fe or Al electrode can improve resistivity against cracking at same level as those without crack.

4. Comprehensive evaluation

Table 2. shows comprehensive evaluation of Fe or Al electrode for electrodeposition method. Al electrode combined with Mg-ace solution showed higher performance than other conditions; even compared with conventional condition using Ti mesh.

5. Conclusion

Fe and Al have enough performance as electrode of electrodeposition method. From experimental results, using Fe or Al electrode have higher repairing effect than conventional using Ti mesh, such as deposition situation, resistivity against Cl^- penetration and resistivity against cracking.

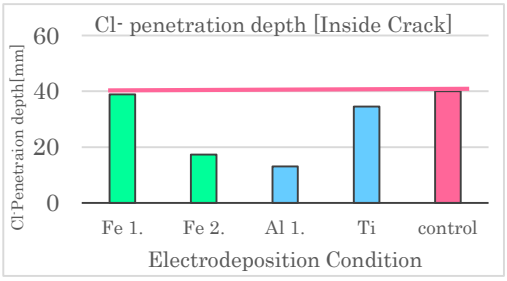

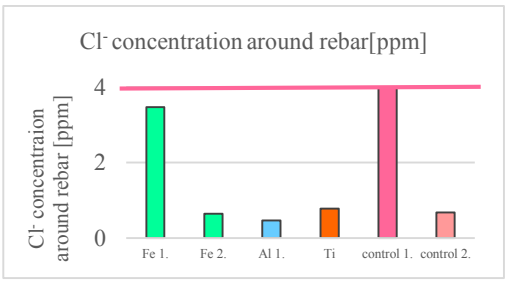

Fig 6. Cl^- concentration around rebar

*control 1: no repaired specimen with crack

**control 2: no repaired specimen without crack

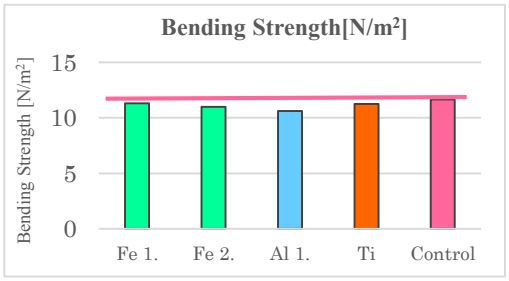

Fig 7. Bending strength

Table 2. Comprehensive evaluation

Elect -rode	Solution	Surface covering	Crack closure	Chemical compound	Against Cl^- attack	Against cracking
Fe	M	◎	○	$Fe_6(OH)_{12}$ -(CO_3) $Mg(OH)_2$	○	○
Fe	MA	◎	◎	$MgAl(OH)_{14}$ -xH_2O $Fe_6(OH)_{12}$ -(CO_3) $Mg(OH)_2$	○	○
Fe	W	×	×	-	×	null
Al	M	◎	◎	$MgAl(OH)_{14}$ -xH_2O $Mg(OH)_2$	◎	○
Al	MA	○	○	$MgAl(OH)_{14}$ -xH_2O $Mg(OH)_2$	○	null
Al	W	×	×	-	×	null
Ti	M	-	-	$Mg(OH)_2$	-	-

Compare to Ti mesh

◎means improved ○means same ×means change for the worth

The interannual variation of the sea breeze arrival time at Tokyo and Kumagaya in summer

ID: 09B18360 Name: Yuta Nejime Supervisor: Prof. Kanda

1. Introduction

The impact of urbanization to sea breeze behavior has been one of the hot research topics[1] because of its mitigation effect of urban heat island. Both simulations[2] and data analyses[3] have suggested the sea breeze delay by urbanization. However, less known is the effect of both urbanization and global warming on sea breeze behavior. One of the reasons for the scarcity is difficulty in investigating the sea breeze behavior in old days due to the lacking of data.

This research focused on the change in sea breeze behaviors between 1960s and 2000s using routine observation records of Japan meteorological agency. Through the analysis, the effect of urbanization and synoptic climate change on sea breeze behavior was separately discussed.

2. Methodology

Analysis days were selected from the following criteria: (1) no rainfall, (2) more than 7h sunshine and (3) wind direction southeast to south-southwest during mean maximum wind velocity. Analysis periods were July to September between 1965 and 1969 for old data and between 2010 and 2012, for the current situation, respectively.

Sea breeze arrival time was estimated by specific humidity, wind direction, wind velocity and temperature following the method by Gamo[4]. The old data was available only in autographic recording and thus all the data was digitalized before the analysis.

Multiple linear regression analysis for the sea breeze arrival time at Otemachi and Kumagaya were conducted in order to separate the urban impact and synoptic climate change to the sea breeze behavior.

The multiple regression was derived from the following climate condition as explanatory variables: sunrise time(T_r), synoptic pressure gradient (U: positive in Southeast, V: positive in Southwest), daily temperature difference (ΔT), daily amount of global solar radiation (Q) and rainfall amount on the previous day (R). Here time difference between sunrise time and sea breeze arrival time was set as explained variable.

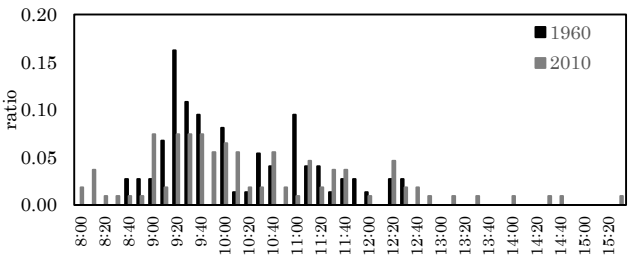

Fig. 1 The ratio of distribution of sea breeze arrival time at Otemachi

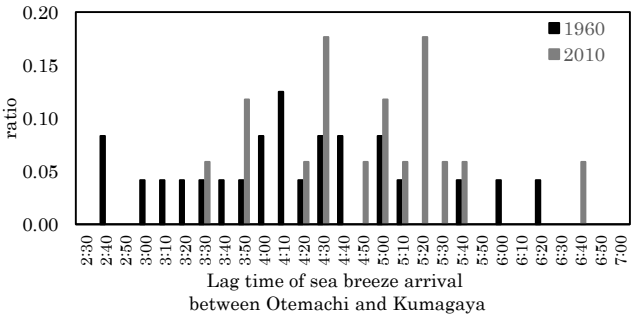

Fig. 2 Frequency distribution of the sea breeze arrival time from Otemachi to Kumagaya

Since we selected climate condition as the explanatory variables, the derived multiple regressions expected to reflect the surface condition; remember sea breeze was affected by both climate and surface conditions. The difference of the derived equations from 1960s and 2010s data could explain the difference in surface conditions between two periods.

3. Result

3.1 Sea breeze arrival time

The number of the analysis days were 108 in 2010s and 76 in 1960s at Otemachi, and 17 in 2010s and 24 in 1960s at Kumagaya.

Fig.1 is the histogram of sea breeze arrival time at Otemachi. The sea breeze arrival time in 1960s seems to be earlier than that in 2010s. Average time of sea breeze arrival was 10:23 in 2010s and 10:10 in 1960s, respectively.

Fig.2 shows that the lag time of sea breeze arrival from Otemachi through Kumagaya. The required time in 2010s was later than those in

1960s; the average time was 4:52 in 2010s and 4:15 in 1960s, respectively, suggesting difficulty of sea breeze penetration by urbanization.

3.2 Effect of urbanization and synoptic climate change on sea breeze behavior

Multiple regression in 1960s and in 2010s were derived as follows:

$$T_p = T_r + 0.168 + 19.0 * U + 21.5 * V + 8.9 * 10^{-3} * \Delta T + (-4.6 * 10^{-4}) * Q + (-4.1 * 10^{-4}) * R \quad \text{(Eq.1)}$$

$$T_p = T_r + 0.117 + 279.7 * U + 313.3 * V + 1.99 * 10^{-2} * \Delta T + 8.5 * 10^{-4} * Q + 5.9 * 10^{-4} * R \quad \text{(Eq.2)}$$

Substituting 2010s input data to the above equations gives the insight of the difference of surface conditions between two periods. Fig.3 shows the sea breeze arrival time estimated in the 2010s equation (Eq.2) tended to be late than those in 1960s, possibly reflecting the difference of the drag effects by urban obstacles like buildings. Substitution of 1960s data to the equations also showed the similar result (not shown).

Meanwhile, substituting data in 1960s and 2010s to the 2010s equation (Eq.2) could give the effects of change in synoptic climate. Fig.4 shows the estimated sea breeze arrival time in 2010s was earlier than those in 1960s. One of the considerable reasons could be the large temperature difference between land and sea surface brought by global warming. Due to the big thermal inertia in sea, the change in sea surface temperature by the global warming could be smaller than in land. Using Eq.1 also shows a same trend (not shown).

The significance of the above results was confirmed by F-test and T-test.

4. Conclusion

The delay of sea breeze arrival time by urbanization was found from long term observation analysis and multiple regression analysis. This tendency was also supported by simulations. Climate condition are also important role to generate the sea breeze, and they advance the sea breeze arrival time in 2010s.

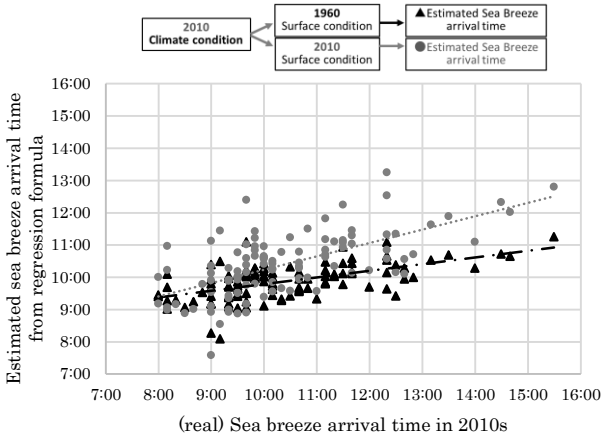

Fig. 3 Estimated sea breeze arrival time from observed data in 2010s
(Reflected the surface condition)

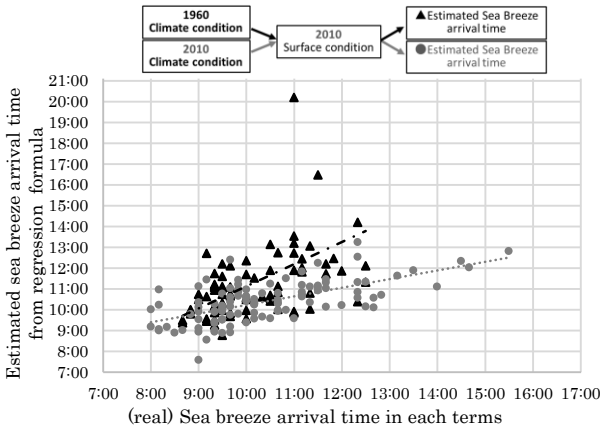

Fig. 4 Estimated sea breeze arrival time from each regression formula
(Reflected the climate condition)

Reference

1)Yamamoto, H., Mikami, T., Takahashi, H.: Influence of Sea Breeze on the Daytime Urban Heat Island in Summer in the Tokyo Metropolitan Area, Journal of Geography, Vol.120, p.325-340, 2011

2)Kusaka, H., Kimura, F., Hirakuchi, H., Mizutori, M.,: The effects of land-use alteration on the sea breeze and daytime heat island in the Tokyo Metropolitan area, Jornal of the Meteorological Society of Japan, Vol.78, No.4, p.405-420, 2000

3)Yoshikado, H. and Kondo.: Inland penetration of the sea breeze over the suburban area of Tokyo, Boundary-Layer Meteorology, Vol.48, p389-407, 1989

4)蒲生　稔:海風前線位置を読み取る方法の比較, 公害, Vol.26, p.31-39

熱画像風速測定法 TIV による塵旋風の二次元空間速度分布解析

学籍番号：10B15311　氏名：張　逸群　指導教官：神田　学，稲垣 厚至

1　はじめに

TIV（Thermal Image Velocimetry）はサーモカメラで撮影された熱画像動画を画像解析にかけることで、物体表面近傍の 2 次元風速分布を測定する手法である。本研究は TIV を塵旋風の観測に応用するものである。人工芝の張られた屋外運動場での屋外大気観測を実施し、これにより観測された塵旋風の（１）流れ場の可視化及び、（２）定量的な解析を行うことを目的とする。

2　塵旋風（Dust devil）

塵旋風とは地表面付近で発達する半径 10-100m 程度の鉛直渦のことであり、渦により地表面の塵が巻き上げられることで可視化されたものを指す。これまでの屋外観測により、静穏な晴天日に発生しやすいことが知られている。これまでに超音波風速計やドップラーライダーを用いた観測が実施されているが、前者は定点の時系列情報しか得られず、後者は空間分布構造を観測することができるものの、1 次元の視線方向風速成分のみ得られるため、詳細な 2 次元風速の空間分布構造を観測した例はこれまでにない。これに対して本研究で用いる TIV では、2 次元風速の水平分布を計測できる点において新たな知見が得られることが期待される。

3　測定手法

TIV とは PIV (Particle Image Velocimetry)でと同様のアルゴリズム用い、粒子画像の代わりにサーモカメラで捉える物体表面温度分布を時系列的に追跡することで、熱分布構造の移流速度分布を求め、そこから地表面近傍の 2 次元風速分布を推定する手法である。表面温度の移流速度と風速の関係については、超音波風速計を用いて熱画像と同時刻の風速を測り、そこで得られる風速と TIV で求められる移流速度を比較する。これまでの観測から、両社は概ね線形関係[1]にあることが分かっており、本研究でもそのような関係を用いた。

ところで、観測される地表面温度画像には地表面の不均一性などに起因した模様が含まれている。その影響を避けるため、ハイパスフィルターを利用してそれらの模様を除去する。

4　観測概要

2013 年 2 月 20 日東京工業大学大岡山キャンパスにある人工芝で覆われたスポーツグランド

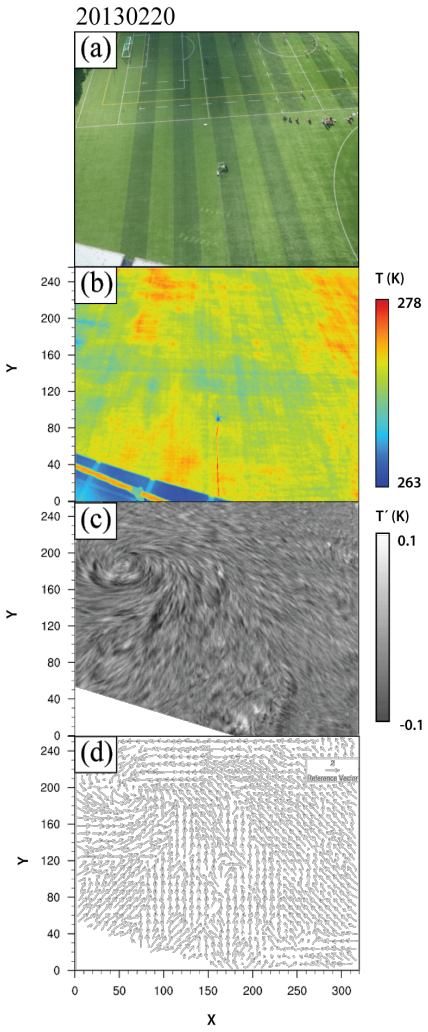

図 1　(a) 観測領域 (人工芝グランド)，(b) 輝度温度，(c)温度変動，(d)移流速度ベクトル

にて観測を行った。地上 47 m の建物の屋上でサーモカメラ（FlIR, SC5200）を設置し、ピクセル数は 256×320 pixels で、フレームレートは 100 Hz で観測した。またグランドでは 5 台の超音波風速計を鉛直方向に並べて設置し、TIV の精度検証に使用した。

観測は 11 時 20 分から 12 時 50 分までの約 1 時間半行った。ここでは塵旋風の見られた、12 時 05 分から 12 時 10 分のデータの解析結果を紹介する。

5　結果

5.1.　TIV による塵旋風流れの可視化

サーモカメラによる観測結果を**図 1** に示す。**図 1a**、**b**、**c**、**d** はそれぞれ可視画像、輝度温度の生画像、ハイパスフィルターをかけた輝度温度、TIV から算出された移流速度ベクトル分布を表す。

図 1b を**図 1c** と比べると、**図 1b** ではグランドの模様が明瞭に映り、流れ場の様子はほとんど確認できない。一方、フィルターをかけた**図 1c** では模様の影響が解消され、半径約 30 m の大きな渦構造が可視化された。

5.2.　移流速度と風速の比較

図 2 は TIV により算出された移流速度と超音波風速計で測定した高度 1.5 m での風速を時間解像度 0.1sec で比較したものであり、両者よく一致していることが確認できる。

5.3.　塵旋風の定量的解析

TIVで得られた計算された2次元風速分布を用いて、塵旋風の定量的な解析を行った。**図3**は TIV、数値解析 (LES, S. Raasch and T. Franke, 2011)，及びランキン渦のモデルより得られた視線方向に対する接線方向速度（**図3a**）、視線方向速度（**図3b**）、渦度（**図3c**）の分布を示す。

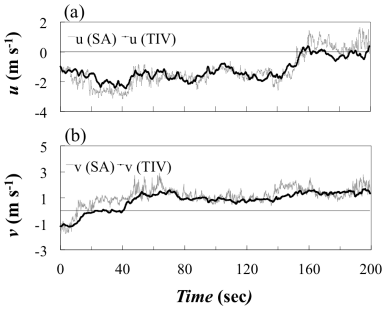

図 2 TIV と超音波風速計で計算された風速の時間変化
SA: 超音波風速計，TIV: 熱画像風速測定法

TIV及び数値解析の結果はアンサンブル平均した結果となっている。これらの図より、渦度の分布が本観測結果および数値解析の結果が一致していることが確認された。一方で、渦心から離れた個所では接線方向速度が大きく、視線方向速度はゼロに近づく傾向が得られた。これは周囲の流れ場及び地表面摩擦の影響と考えられる。本手法で得られる速度分布は地表面近傍の値であることから、より摩擦の影響が色濃く表れたものと考えられ、測定高度の高い数値解析の結果（高度1 m）ではよりランキン渦のモデルに近い値が得られたものと考えられる。

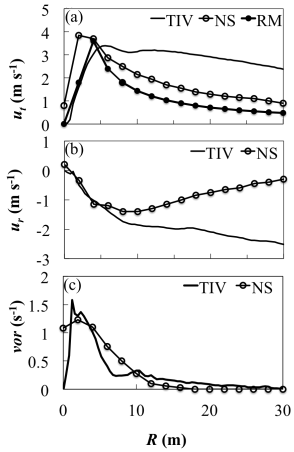

図 3 TIV, 数値解析及びランキン渦モデルでで算出された(a) 接線方向速度，(b) 視線方向速度，(c) 渦度
NS: 数値解析（Raasch and Franke, 2011）
RM: Rankine's combined vortex model

6　まとめ

サーモカメラおよび超音波風速計を用いた観測を実施し、TIVを適用することで塵旋風の２次元速度場分布を観測した。塵旋風周りの風速分布について、渦心を中心としたアンサンブル平均を行い、定量的な解析を行った。その結果、数値解析とランキン渦のモデルに一致していることが確認できた。

参考文献

[1] 神田学，稲垣厚史，久米村秀明:“サーモカメラを用いた壁面近傍風速の計測手法開発”, ながれ,Vol.31, pp.491-493, 2012
[2] 稲垣厚至，神田学：熱画像風速測定法TIVによる地表面近傍の大気乱流観測，ながれ，32，307-312，2013.
[3] Adrian RJ (1991) Particle-imaging techniques for experimental fluid mechanics. Annu Rev Fluid Mech 23: 261-304
[4] (9) Raasch, S. and T. Franke, 2011: Structure and formation of dust devil-like vortices in the atmospheric boundary layer: A high-resolution numerical study. J. Geophys. Res., 116, D16120, DOI: 10.1029/2011JD016010, Supplementary animation: 10.5446/9352

Simulation of Sea Breeze penetration in Kanto region by using WRF-CHEM

ID: 10B22713　Name: Tomoaki Mitsui　Supervisor: Prof. Kanda

1. Introduction

One of the hot issues in urban meteorology has been the impact of urbanization to sea breeze behavior as well as mitigation effect of sea breeze on urban heat island. For example, Varquez et al[1)] pointed out that urbanization disturbs sea breeze penetration to inland in their simulations. However, in the previous studies sea breeze front was estimated by change of temperature, humidity, and wind velocity at some specific surface observation points, and thus it is difficult to analyze 3-dimentional features including strong vertical mixing in the front.

For better understanding of sea breeze behavior and its impact to urban climate, WRF-CHEM (Weather Research and Forecasting model – Chemistry) was used. WRF-CHEM is one of WRF packages, which support passive scalar transport option. Sea breeze can be identified by tracing passive scalars. To see the urban effects on sea breeze, two simulations were done: one considered realistic urban features (SDLC): the other revised all urban grids to the grassland category (VEGE). SDLC was carried out with highly sophisticated urban modeling.

2. Simulation settings

September 14th 2011 was selected as analysis day. The domain setting is shown in Fig 1. Three different passive scalars were released from the Tokyo bay, Sagami Bay and the free atmosphere just before the onset of sea breeze.

3. Result and Consideration

In Figure 2, time evolution of sea breeze front was shown as well as the distribution of the scalar at 13:00; line in Figure 2 represents the front at 13:00, 14:00, 15:00, 16:00, and 17:00 from the bottom to top. Sea breeze front was identified, based on the spatial gradient of the scalar.

Sea breeze front was delayed in SDLC as clearly confirmed by sea breeze front at 17:00. The difference in sea breeze front between SDLC and VEGE shows urban effect, i.e.. thermal effect associated with urban warming and the drag effect by urban geometry.

Scalar concentrations near surface both from the Tokyo bay and free atmosphere at 13:30 in SDLC are shown in Figure 3. The scalar fell down from the free atmosphere in advance of the sea breeze front.

The free atmosphere is known for its dry and high potential temperature, thus this subsidence flow can contribute to the warming up of Saitama area. The subsidence flow seems to be related with strong updraft and vertical mixing in front of sea breeze; these eroded the free

atmosphere. Figure 4 shows SDLC brought more scalar from the free atmosphere than VEGE did reflecting aforementioned thermal and dynamical effects by urbanization.

4. Conclusion

Sea breeze behavior was simulated in SDLC and VEGE tracing passive scalar advection. The following results were obtained.

(1) The comparison of SDLC case and VEGE case showed sea breeze advanced more in VEGE case than in SDLC case, possibly reflecting urban effect.

(2) Subsidence flow in front of sea breeze occurred. The scalar transportation from the free atmosphere was larger in SDLC than that in VEGE, due to the difference of intensity of the vertical mixing between them.

References

1) Varquez, A.C.G., Nakayoshi M, Kanda M, : The Effects of the Distribution of Highly Detailed Urban Surface Parameters on a Sea Breeze Simulation in Kanto, 2011 (submitted)

2) 蒲生稔、海風前線位置を読み取る方法の比較、公害、vol. 26、p31-39、1991

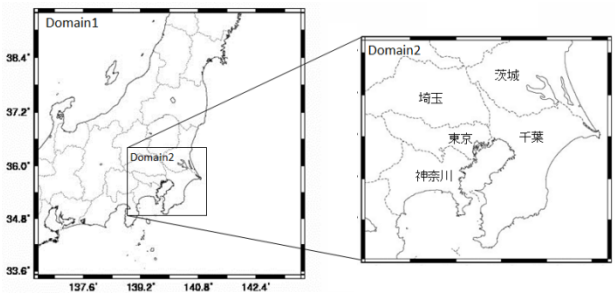

Figure 1. Domain settings

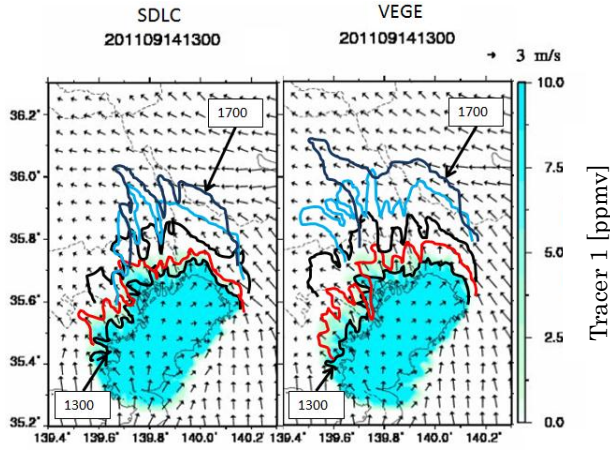

Figure 2. Time evolution of Sea Breeze Front

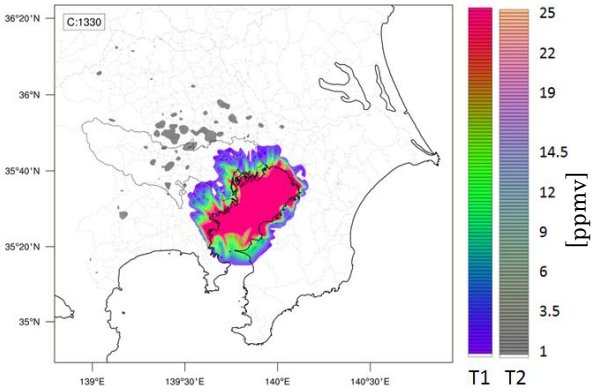

Figure 3. Scalar concentration near surface both from the Tokyo bay and free atmosphere at 13:30 in SDLC (T1: Tracer 1 is from the Tokyo bay, T2: Tracer 2 is from free atmosphere).

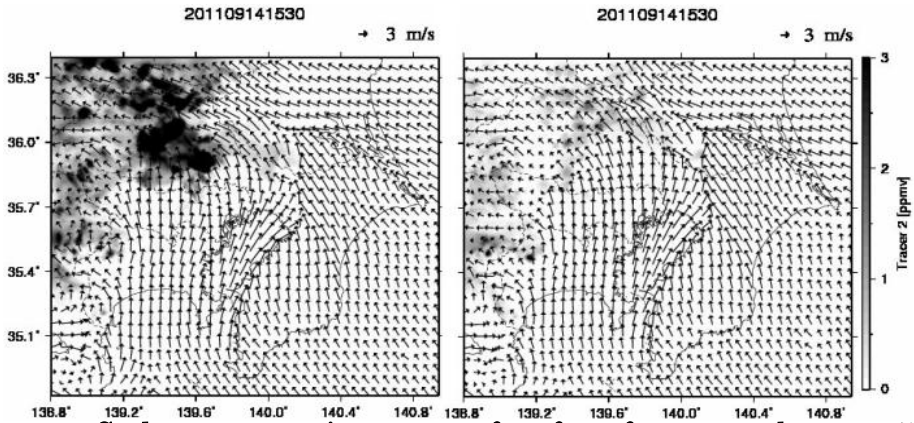

Figure 4. Scalar concentration near surface from free atmosphere at 15:30 (left figure shows SDLC, right figure shows VEGE).

Large-Eddy Simulation of Coupling Real Urban Geometry Field and 3D Radiative Process

Student ID : 10_25829 Name : Yuma YOSHIDA Supervisor : Manabu KANDA, Atsushi INAGAKI

1. Introduction

Atmospheric boundary layer (ABL) is driven by mechanical and buoyancy effects created at the ground surface. In urban areas, the surface geometry has a three-dimensional complexity due to the building array, and causes complex aerodynamic and thermal effects on the flow field within the ABL. To examine their effects, especially focusing on the effect of heat, urban air flow is simulated using large-eddy simulation (LES) with input of three-dimensional sensible heat flux database calculated in an urban heat balance model.

In a field of meteorology, LES is used to simulate an air flow within and above the urban canopy. However, most of the cases are carried out under neutral stratification, and not many studies consider the effect of heat. On the other hand, mainly in the architectural field, realistic three-dimensional energy balance solved to simulate a detail thermal environment in cities, in which sensible heat flux from the each building facets could be obtained.

Based on the two research directionalities above, urban air flow is simulated using LES with implementing a realistic thermal input from building facets and the ground represented by a 3D energy balance model.

2. Methodology

2.1 Basic equation of LES

In this study, Parallelized Large-Eddy Simulation (PALM) was used. Basic equation of this model is Navier-Stokes equation, the continuity equation, and first principle of thermodynamics.

$$\frac{\partial u_i}{\partial t} = -\frac{\partial}{\partial x_k}\overline{u_k}\,\overline{u_i} - \left(\varepsilon_{ijk} f_j \overline{u_k} + \varepsilon_{i3k} f_3 u_{gk}\right) - \frac{\overline{\theta^*}}{\theta} g\delta_{i3} - \frac{1}{\rho_0}\frac{\partial \overline{p^*}}{\partial x_i} + \frac{\partial}{\partial x_k}\tau_{ki} \quad (1)$$

$$\frac{\partial \overline{u_i}}{\partial x_i} = 0 \quad (2)$$

$$\frac{\partial \overline{\theta}}{\partial t} = -\frac{\partial}{\partial x_k}\overline{u_k}\,\overline{\theta} + \frac{\partial}{\partial x_k}\overline{u_k'\theta'} \quad (3)$$

Then, u_i is x_i direction velocity, p is pressure, ρ_0 is density (1.0 constant in this model), θ is potential temperature. Upper bars represents spatial filtered value. In this study, coriolis force is neglected.

2.2 3D radiative process

In this study, LOCALS-UCSS developed by Yasunobu Ashie of NILIM is used to reproduce thermal boundary condition on the building and ground facets. This model is considering the multi refraction process of radiation. The resulted sensible heat flux distribution from the each surface facets are input as the thermal boundary condition of LES model.

2.3 Ray-Tracing method

Two kinds of radiation models are used to reproduce realistic thermal boundary conditions in cities. 3D-Rad considers multi refraction of long and short wave radiations, which has large calculation load. Ray-Tracing method just considers the shade and sunlit area on building facets, and assigns a constant sensible heat flux. Fig.1 shows vertically integrated sensible heat flux.

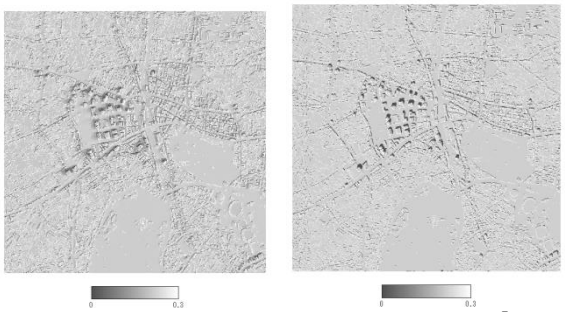

Fig1: Vertical integrated sensible heat flux[Kms^{-1}]
Right:3D-Rad, Left:Ray-Tracing

3. Numerical Setting

3.1 Calculation conditions

Numerical settings in LES are shown in Table 1. Grid size in z is stretched with the factor of 1.08 above z=1750m.

Table1: Calculation Conditions

Domain size	4000m×4000m×4619m
Grid size	5m×5m×5m(z<1750m) Note: z>1750 z-direction grid size is stretched
Initial wind velocity	3.0 m s^{-1}, 10.0m s^{-1}
Sensible heat flux input	0.186 Km s^{-1}
Date of calculation	4th June 2013 12pm
Boundary condition	Cyclic (x, y) Slip (top) Non-Slip (Bottom)
Calculation time	10800 sec (v3) 7200 sec (v10)

3.2 Simulation site

Shinjuku is chosen as calculation site. Fig.2 shows building height distribution. This area includes high-rise skyscraper area in the center, and park in the south and east regions.

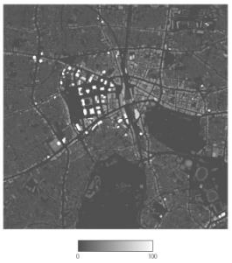

Fig2: Building height of calculation site

3.3 Simulation cases

8 cases of simulation were conducted. 3D-Rad, Ray-Tra, Floor Heat, are different method to give the heat distribution. No heat is neutral calculation used as a reference.

Table2 shows the simulation case.

Case	Initial velocity	Heating method
3D-Rad_v3	3.0 m/s	LOCALS-UCSS
Ray-Tra_v3		Ray-Tracing method
Flour Heat_v3		Floor and Roof only
No heat_v3		Neutral
3D-Rad_v10	10.0 m/s	LOCALS-UCSS
Ray-Tra_v10		Ray-Tracing
Flour Heat_v10		Floor and Roof only
No heat_v10		Neutral

4. Result

4.1 Thermal effects on Surface layer

Fig.3 is vertical profiles of turbulent intensity normalized by friction velocity.

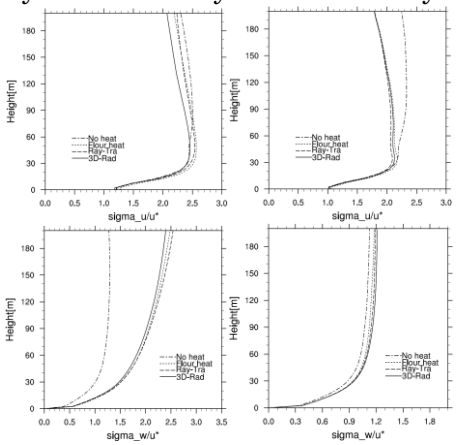

Fig3: Normalized turbulent intensity σ_u, σ_w
Upper: σ_u , Lower: σ_w
Left: _v3 case, Right: _v10 case

As a result, wall heating weaken σ_u but, strengthen σ_w . Especially σ_w of v3 case is stronger than neutral case.

4.2 Thermal effects on convective layer

Fig.4 compares σ_w normalized by convective scale velocity w_* with function of convective layer model. z_i is ABL height. Simulation results entirely follow the model values except lower part of v10 case in which the turbulent intensity becomes larger than the model value. This is considered to be a wake turbulence from the buildings because this model is developed based on an experiment in a flat field without large obstacles.

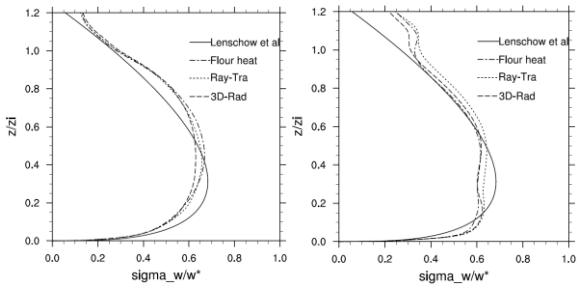

Fig4: Normalized σ_w profile
Left: _v3, Right: _v10

Fig5 is 30 min averaged w at xy and xz cross sections for V3 cases. 3D-Rad has thermal roll but the other cases have no rolls. This implies that the difference in the pattern of surface heating could invoke a large structure above.

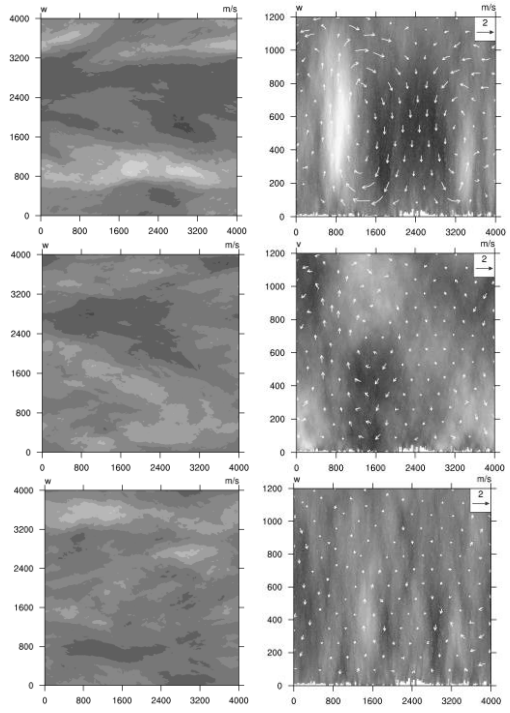

Fig5: Left: z=397.5m cross w contour
Right: x=3200m cross w contour
From upper, 3D-Rad,Ray-Tra,Floor Heat

Reference

[1] Ashie, Y., Kono, T., (2011) : Urban-scale CFD analysis in support of a climate -sensitive design for the Tokyo Bay area, International Journal of Climatology, Vol.31, pp 174-188

衛星画像を用いたチャオプラヤ川中流域における大規模浸水現象の定量化と要因考察

学籍番号：07_23649　氏名：逸見聡　　指導教官：木内豪

第一章　序論

2011 年、タイのチャオプラヤ川流域において夏から秋にかけて大規模な洪水が発生した。特に下流域に位置するアユタヤやバンコクなどのエリアでは市街地への浸水など目に見える被害が大きく、タイ国のみならず周辺国の経済活動へも大打撃を与える結果となった。

そこで本研究では、ENVISAT 衛星画像と HJ-1A 衛星画像を利用して氾濫域の推定を行い、その結果をもとに今回の浸水現象の時系列推移を水文、気象条件などのデータと比較し、要因分析を行う。2011 年の洪水のみならず、近年タイにおいては洪水の規模・頻度ともに増加傾向にある。その要因は地球温暖化による年降水量の変動幅増大、をはじめとして様々指摘されており、実に複合的である。様々なデータとの比較により浸水要因を洗い出してゆくことで、今後起こりうる洪水の対策及び被害軽減に少しでも役に立つことが期待できる。

また、本研究の対象エリアはチャオプラヤ川の中流域である。以下の図 1 に示す。

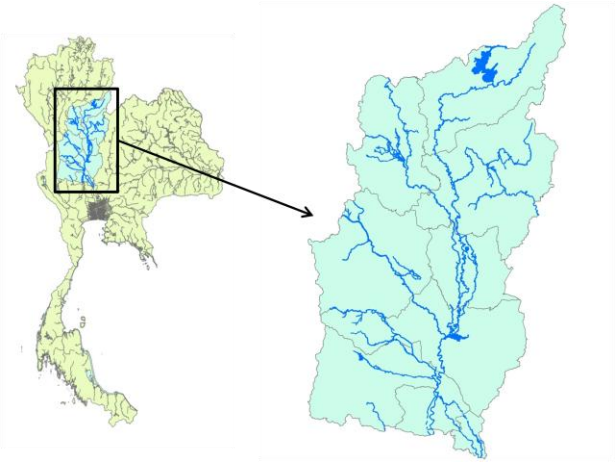

図 1　対象エリア（左図はタイ全土）

第二章　既往の研究

本研究のような人工衛星による氾濫域の推定が行われた事例を二つ紹介する。

一つは、UNOSAT により公表されている浸水マップである。その解析エリアは流域全体を網羅しているが、解析に用いられた衛星 MODIS の解像度は 250m と粗く、その頻度も約一カ月に一度程度と氾濫域推移の把握には十分ではない。

もう一つが、GISTDA と JAXA の共同により行われた解析である。これには航空機搭載多周波・多偏波合成開口レーダである Pi-SAR-L が用いられ、JAXA は 2011 年 11 月 5 日から 12 月 27 日まで観測を行った。この衛星の解像度は 3.0m と大変優れているが、解析期間が限定的であり、観測エリアは主要な都市部のみである。

第三章　衛星画像解析による浸水域の推定

氾濫域抽出のため、本研究では HJ-1A、ENVISAT の 2 種類の衛星データを利用した。ENVISAT のデータは解像度こそ 150m と粗いが、雲の影響を受けないため広域での氾濫解析に適している。一方の HJ-1A 画像は、雲の影響を受けてしまうため広域での浸水域抽出には適さないが解像度が 30m と高い。この長所をもつ HJ-1A 画像と ENVISAT 画像の比較を局所的に行うことで精度を高め、最終的に ENVISAT 画像で全体の解析を行う。解析フローの概要を図 2 に示す。

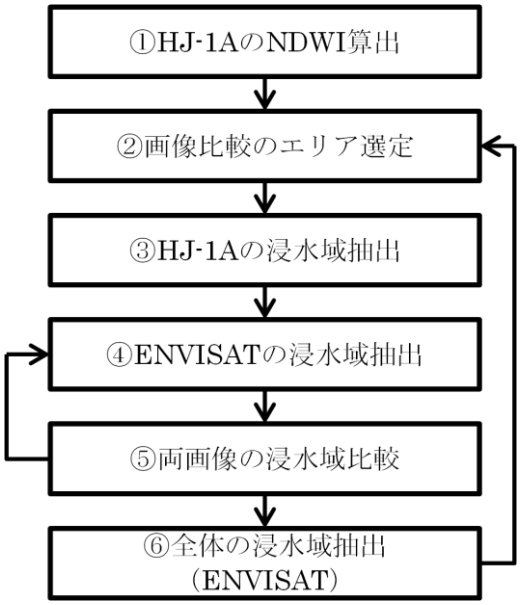

図 2　浸水域推定のフロー

手順①における NDWI（Normalized Difference Water Index：正規化水指標）は、HJ-1A の可視光（バンド 3）と近赤外光（バンド 4）それぞれの反射率の値から、GREEN にバンド 3、NIR にバンド 4 を当てはめ、次の計算式により求められる。

$$NDWI = \frac{GREEN - NIR}{GREEN + NIR} \quad (-1 \leqq \mathrm{NDWI} \leqq 1)$$

手順⑤の両画像の浸水域比較では、以下の条件を設定して適合率を求め、その値が最大となるような後方散乱強度を ENVISAT の閾値とし、全体の浸水域抽出を行った。

表 1　浸水域適合評価の指標

		HJ-1A	
		浸水域	非浸水域
ENVISAT	浸水域	a	b
	非浸水域	c	d

$$適合率 = \frac{a+d}{a+b+c+d} \times 100(\%)$$

第四章　浸水域推移からみる洪水特性の考察

浸水現象の考察にあたり、降雨量、水位、流量などの水文・気象条件、その他標高、土地利用などの様々なデータを用いた。第三章のフローにより求められた解析結果と考察内容を一部抜粋して紹介する。

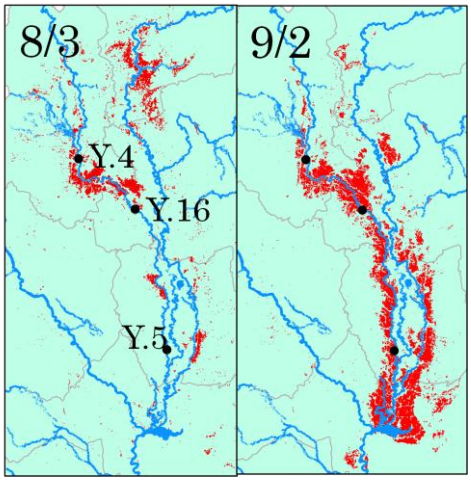

図 3　解析結果の比較

図 3 に 8 月 3 日、9 月 2 日の解析結果の比較を示す。黒点は、Yom 川における観測点の位置である。比較すると上流からの氾濫が進んでいることが分かるが、この要因は、河川の急激な水位上昇に起因する越流発生によるものと考えられる。図 4 は観測点 Y.16 における河川の水位変動（黒色）と左岸と右岸の標高（それぞれ緑色、青色）および一日ごとの降雨量（赤色）を示したグラフである。8 月から 9 月にかけての水位上昇と氾濫拡大の水位が比例しており、また左岸側の標高が低くこれが Yom 川流域全体で左岸側の氾濫がより大きく広がっている事にも関連していると推測できる。

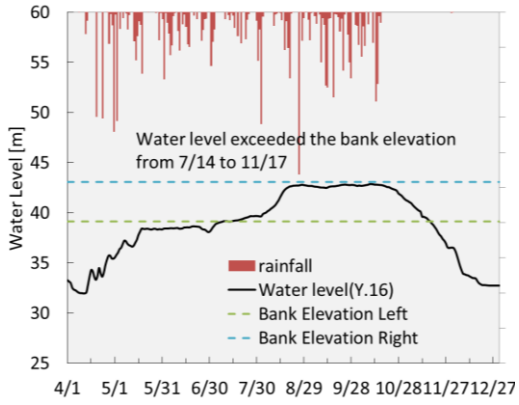

図 4　観測点 Y.16 における流下能力と流量関係

第五章　結論と今後の課題

本研究では、ENVISAT と HJ-1A という二種類の衛星データを用いて時系列の浸水域情報を作成した。本研究の画像処理により得られた情報は、上記の通り様々な情報と比較した非常に事細かな分析が可能であり、今後様々な氾濫解析の検証に用いるためのデータとして大いに役立つことが期待できる。

浸水現象の推移においては、河川の流下能力に大きく依存することが推測できる。流下能力の小さいエリアでは氾濫が広がりやすいが、それが下流への氾濫拡大を遅らせる効果も発揮していたと考えられる。浸水域の時系列変化の考察にあたっては気象条件、土地利用など様々なデータとの比較を行ってきたが、標高などの微地形による特徴まで考慮したものではなかった。これらの本研究において不足していた要素も考慮することが出来れば、より精度の高い要因考察が可能となり今後の災害対策にも更に役立つことだろう。

参考文献

[1] 佐山敬洋、建部祐哉、藤岡奨、牛山朋来、萬矢敦啓、田中茂信：2011 年タイ洪水を対象にした緊急対応の降雨流出氾濫予測、土木学会論文集

[2] UNOSAT,Maps,Thailand,
URL: http://www.unitar.org/unosat/maps/tha

[3] 一般財団法人リモート・センシング技術センター：Pi-SAR によるタイ洪水解析
URL:https://www.restec.or.jp/wp-content/uploads/2012/10/b8854c0d9d9d875d819065fa1bd1f5fa.pdf

[4] 大吉慶、河野宜幸、島田政信、祖父江真一：航空機搭載 バンド合成開口レーダ（Pi-SAR-L）によるタイ王国の洪水災害観測

[4] 小森大輔：2011 年タイ国チャオプラヤ大洪水はなぜ起こったか、盤谷日本人商工会議所所報

[5] 東京大学生産技術研究所沖研究室：2011 年タイ国水害調査結果（第 4 報）

[6] 近藤純正：蒸発散量と降水量の気候学的関係―研究の指針―、日本気象学会、1998

Visualization of Direct and Indirect CO_2 Emission of each Municipality in Japan

Student Number: 09-04026 Name: Xuyang WANG Supervisor: Shinya HANAOKA

1 Introduction

The IPCC concluded in the 5th assessment report that the rapid rise of CO_2 concentration is the result of human activities. Considering the IPCC's simulation results of climate change, The Japanese government set the new target of 3.8 percent CO_2 reduction by 2020 from the 2005 level while struggling to formulate a new energy policy assuming that all Japanese nuclear reactors were idled. To achieve the target, Japanese government needs to urgently plan domestic policies and legislation for reduction measures.

However, local municipalities are not moving ahead with a plan to reduce global warming (except large local municipality). One of the important reasons is that, up to now, the CO_2 emissions were mainly estimated as an average of the whole Japan. There is not enough data of CO_2 emissions in each municipality for local governments to plan their own policies about global warming. Therefore, it is necessary to estimate the CO_2 emissions in each municipality.

CO_2 emissions fall into 2 types, direct emissions and indirect emissions. In this study, direct emissions mean the emissions from different CO_2 emitting regions which are derived from industry sector, transportation sector, commercial sector, and residential sector. And indirect emissions mean the emissions from the regions where the commodities are consumed according to expenditure of money on the items for daily household life. Consideration of the indirect CO_2 emission is important because about 47% of CO_2 emissions are caused by the private consumption expenditure [3] and it is necessary to change viewpoint of responsibilities of the energy consumer. But there is no complete data of indirect CO_2 emissions in each municipality of Japan.

The objective of this study is 1) to unify direct CO_2 emissions in each sector of Japan by using GIS, 2) to estimate the indirect CO_2 emissions from a data set of emission intensity from Embodied Energy and Emission Intensity Data for Japan Using Input-Output Tables (3EID) and Household Expenditure Survey (HES) and 3) to visualize these results. For the lack of region data, this study estimate direct/indirect CO_2 emissions in each municipality. In order to make people understand the characteristics of statistical data intuitively without special knowledge, the results of direct/indirect emissions are visualized by area cartogram. It can be used as a material when planning domestic policies and legislation for CO_2 reduction measures.

2 Methodology

2.1 Direct CO_2 Emission

Direct emissions were unified from the previous studies in each sector.

1) Residential sector

First, we multiply the data of a) total area of floor space (detached houses; collective houses), b) energy consumption of each energy source and each energy use and c) heat value basis. Then we allocate the figures calculated for each prefecture [2] to each municipality depending on the rate of household of each housing type (detached houses; collective houses).

2) Commercial sector

First, we multiply the data of a) total area of floor space of each building use and b) energy consumption and the rate of each energy source and energy use of each building type. Then we allocate the figures calculated for each prefecture [3] to each municipality depending on the rate of persons engaged in each business category.

3) Industry sector

A counter-measures evaluation model (G-BEAMS [4]) is used to estimate CO_2 emission. NOx emission data is allocated to each mesh depending on the rate of population, production value, etc. Then CO_2 emission of industry sector in Japan is allocated to each mesh depending on the spatial distribution of NOx emission because the CO_2 emission is proportional to NOx emission in Japan.

4) Transportation sector

We multiply the data for roads of each municipality and for each vehicle type of a) mileage travelled (km/year) and b) CO_2 emission factor (g-CO_2/km). Then take into consideration the increase in the amount of the emission during start and stop of automobiles in addition to the amount of the running emission.

2.2 Indirect CO_2 Emission

In this study, indirect CO_2 emission was calculated by using the data below. All the data is for the year of 2005.

a) HES

The survey shows monthly income and expenditure of households in prefectural capitals. In this study, the date of annual household's expenditures which were classified by 981 items in each prefectural capital was used. It was set as E.

b) 3EID

This data shows the environmental load due to the production activities which are equivalent to money amount. There are 2 kind of 3EID, one is setting the emission intensity of import products as same as domestic goods. We call it domestic emission intensity. The other one have considered the supply chain of import products. We call it global emission intensity. We used the 2 kinds of 3EID in this study but only show the result of global in the article abstract. It was set as *ic*.

c) Population Census

In this study, numbers of households in each municipality were used from the data. It was set as *H*.

The indirect CO_2 emission was calculated by

$$CE_i = \sum_j H_{ij} \left[\sum_k E_{ijk} \left(ic_{ik} + dc_{ik} \right) \right] \quad (1)$$

CE_i: Annual CO_2 emission in each zone i (kg-CO_2/year)

j: the type of household which is divided into two-or-more-person households and one-person household.

H_{ij}: The number of type j households in zone i

E_{ijk}: Annual expenditure to the item k by type j household type in zone i (yen/household/year)

ic_{ik}: Emission intensity of indirect CO_2 for the item k in zone i (t-CO_2/million yen)

dc_{ik}^{*}: Emission intensity of CO_2 by direct combustion for the item k in zone i (town gas, LPG, kerosene and gasoline) (t-CO_2/million yen)

*About dc_{ik}: This is the CO_2 emissions intensity of town gas, LPG, kerosene and gasoline by direct combustion when these kinds of energy source are being used. The values of dc_{ik} are calculated as the following (t/ million yen). The ethanol blended fuel is treating as the same kind of gasoline.

dc_i (Kerosene) = 27.71; dc_i (Gasoline) = 14.64;
dc_i (LPG) = 23.56; dc_i (Town Gas) = 17.87 (2)

The Figure 1 shows the estimation process of annual indirect CO_2 emissions in each municipality.

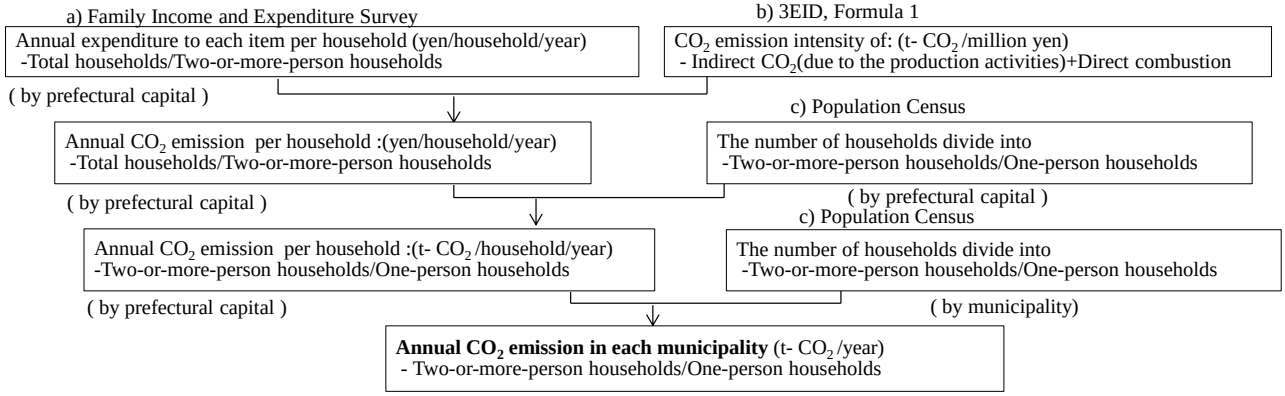

Figure 1 Estimation process of indirect CO_2 emission

2.3 Data Visualization

The statistical data was often expressed by Choropleth Map. But in this study, when the range of CO_2 emissions is large between regions, you have to divide the legend with more kinds of colors. This makes it difficult to match the legend. Therefore, so we used Area Cartogram, a map in which some thematic mapping variable is substituted for land area. The space of the map is distorted by the information of statistical data so that people can understand the characteristics intuitively. In this study, the methodology of area cartogram was quoted by the study of Inoue[8].

3 Results

The visualization results of direct/indirect CO_2 emissions were shown as the Figure 2 and 3. The area on the map shows the total CO_2 emission and and the color shows the per-person CO_2 emissions.

For the direct emissions, the total CO_2 emissions of some areas are significantly larger than others. This is because the thermal power stations which were giving a significant impact on the environment. The data is for 2005, so the influence of thermal power plants is great even before the Tohoku Earthquake. So when all Japanese nuclear reactors were idled, the reduction of CO_2 emissions would be stringent. The metropolises, industrial complex also have a large emission because of the productive activity. The commercial and business districts also have large emissions because which is derived from the transportation sector and commercial sector.

For the indirect emissions, the area of thermal power stations and the industrial complex regions became normal. The total indirect emissions are mostly from metropolises, prefectures. This shows the CO_2 emission from energy conversion has been allocated to final consumers. When the density of household is large, the indirect emission would be large. And when there is an active consummation, the per-person emissions would also be large.

As the overall trend, the total amounts of direct emissions are larger than the indirect ones. This shows the most CO_2 emission is from the productive activity, but that is for the final consumers.

4 Conclusion

This study estimated indirect CO_2 emission in each municipality unit which had not been estimated in the previous studies. And the results of direct/indirect emissions were visualized by area cartogram for offering for people can understand without special knowledge. The data was easily compared to each other and the differences of each municipality and spatial distribution CO_2 emission was expressed strongly. It can be used to analyze the characteristics of CO_2 emissions' distribution and attribution in the future. Both of the methodology and the results of this study can be a

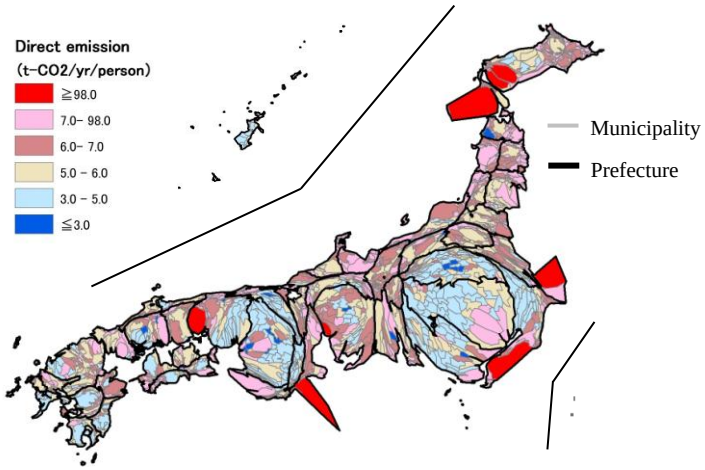

Figure 2 Direct CO_2 Emissions

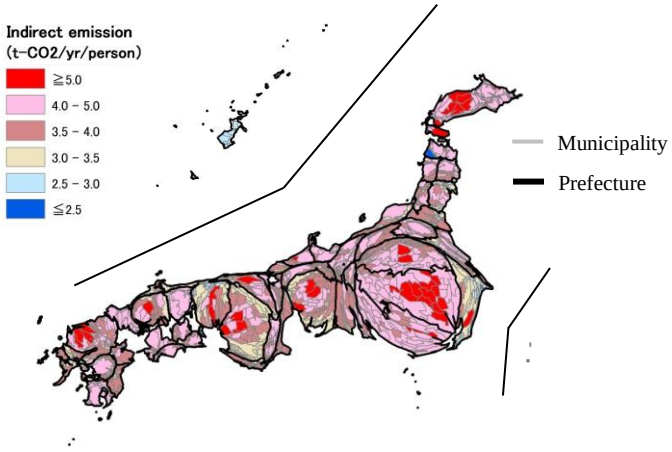

Figure 3 Indirect CO_2 Emissions (global emission intensity)

useful material for the local governments to plan their own policies and legislation for CO_2 reduction measures. The control of CO_2 emissions in Japan can be facilitated.

References

[1] Sawako Shigeto., et al.: An easily traceable scenario for 80% CO_2 emission reduction in Japan through the final consumption-based CO_2 emission approach: A case study of Kyoto-city, Applied Energy 90, pp.201-205, 2012.

[2]Tonooka, Y., et al.: A detailed energy demand estimation and CO_2 emission inventory of residential house by prefecture and housing type in Japan, J. Environ. Eng., AIJ, 592, pp.89-96, 2006. (in Japanese)

[3]Tonooka, Y., et al.: CO_2 emission reduction scenario in building sector in Japan, CGER report I079-2008, pp.91-133, National Indtitute for Environmental Studies, 2008. (in Japanese)

[4]Nansai, K., Suzuki, et al.: Design of Georeference-Based Emission Activity Modeling System (G-BEAMS) for Japanese emission inventory management, Online proceeding of 13th International Emission Inventory Conference, pp.1-11, June, Florida, USA, 2004.

[5] Ryo Inoue,: Studies on cartogram construction algorithms for better visualization of statistical data on GIS, Papers of Research Meeting on Civil Engineering Planning, 2005. (in Japanese)

塩害及び中性化におけるフライアッシュを用いた海水練り鉄筋コンクリートの寿命予測

学籍番号: 10-00976　名前: 易　成　指導教員: 大即　信明

1 背景

世界的な水不足が懸念されている中，コンクリート分野において海水を有効利用することが日本コンクリート工学会などで検討されている．小原の研究[1]によると，普通ポルトランドセメント(以下 OPC)に高炉スラグ微粉末を混和することで海水練りコンクリートの長寿命化の可能性が示された．しかし，水不足が特に懸念される発展途上国においては高炉スラグを生成する製鉄所は広く分布していない．

発展途上国での海水練りコンクリートの使用を考える際，石炭火力発電所の産業副産物であるフライアッシュ(以下 FA)の利用が有効と考えられる．しかし，海水練りコンクリートへの FA の適用可能性の検討およびその効果に関する詳細な知見は数少ない．

以上を踏まえ，本研究では目的を(1) FA を用いた海水練り鉄筋コンクリートの物性と腐食挙動の把握，(2) 塩害及び中性化における FA を用いた海水練り鉄筋コンクリートの定量的な寿命予測を，Cl^- 拡散係数，腐食発生限界 Cl^- 量，中性化速度係数，酸素透過量から評価した．

2 実験概要

2.1 使用材料

本研究では，練混ぜ水に水と ASTMD1141-98(2003) に準じた人工海水(Cl^- 濃度 2%)を使用した．細骨材に陸砂，粗骨材に陸砂利を使用した．供試体に設置する棒材に φ13mm×10cm の普通鉄筋(SR235)を使用した．セメントに OPC と JIS で規定された FA Ⅱ種を 2 種類（能代 FA，勿来 FA）と JIS 規格外の FA（相馬 FA）の計 3 種類を使用した．

2.2 供試体

本研究では，φ100×20cm の無筋の円柱コンクリート供試体と鉄筋をかぶり 10mm の位置に設置した 40×40×160mm^3 の角柱モルタル供試体を使用した．表 1 に記した配合はコンクリートとモルタル両方の供試体を作製し，表 2 に記した配合はコンクリート供試体のみ作製した．コンクリート供試体は OPC を使用した場合打設後 5 日間，FA を混和した場合 7 日間湿空養生を行った．モルタル供試体は練混ぜ水と同じ種類の水を用いて 7 日間水中養生を行った．なお，海水練りによって初期に混入する Cl^- 量は約 3.0kg/m^3 であった．

表1. コンクリート及びモルタル供試体

水セメント比(単位水量)	セメント種,(FA置換率 ,%)	練り混ぜ水	呼び記号
0.5(171kg/m³)	OPC, (0)	水	0.5OPC-W
		海水	0.5OPC-S
	JIS規格Ⅱ種FA, (10)	水	0.5能代(Ⅱ)FA10-W
		海水	0.5能代(Ⅱ)FA10-S
	JIS規格Ⅱ種FA, (30)	水	0.5能代(Ⅱ)FA30-W
		海水	0.5能代(Ⅱ)FA30-S
	JIS規格Ⅱ種FA, (30)	水	0.5勿来(Ⅱ)FA30-W
		海水	0.5勿来(Ⅱ)FA30-S
	JIS規格外, (30)	水	0.5相馬(×)FA30-W
		海水	0.5相馬(×)FA30-S
0.7(174kg/m³)	OPC, (0)	水	0.7OPC-W
		海水	0.7OPC-S
	JIS規格Ⅱ種FA, (30)	水	0.7能代(Ⅱ)FA30-W
		海水	0.7能代(Ⅱ)FA30-S

表2. コンクリート供試体

水セメント比(単位水量)	セメント種，FA置換率,%	練り混ぜ水	呼び記号
0.5(171kg/m³)	JIS規格Ⅱ種FA, (10)	水	0.5勿来(Ⅱ)FA10-W
		海水	0.5勿来(Ⅱ)FA10-S
	JIS規格外FA, (10)	水	0.5相馬(×)FA10-W
		海水	0.5相馬(×)FA10-S
0.7(174kg/m³)	JIS規格Ⅱ種FA, (10)	水	0.7能代(Ⅱ)FA10-W
		海水	0.7能代(Ⅱ)FA10-S

2.3 測定項目及び測定方法

(1)　Cl^- 拡散係数

(JSCE)-G 572-2010 に従い，曝露面とした打設下面以外をエポキシ樹脂でシールしたコンクリート供試体を人工海水中に 4 ヶ月または 12 ヶ月浸漬後，スライス法によって分析した結果をフィックの拡散方程式を用いて Cl^- 拡散係数を算出した．

(2)　中性化速度係数

JIS A 1153 に従い，曝露面とした打設上面と下面以外をアルミテープでシールしたコンクリート供試体を CO_2 5%(一部 10%)の中性化促進環境下で，曝露 4, 12, 16 週後，フェノールフタレイン法を用いて中性化深さの測定を行い，√t 則から中性化速度係数を算出した．算出した中性化速度係数は魚本式[2]を用いて大気中濃度 0.035%における中性化速度係数に変換した．

(3)　酸素透過量

50℃, NaCl 3%の塩害促進環境で曝露面とした打設下面以外をエポキシ樹脂でシールした曝露 20 週後のモルタル供試体のカソード分極曲線から得られた限界電流密度[3]を用いて算出した．

(4)　腐食電流密度

(3)と同じ条件で曝露したモルタル供試体の腐食電流密度を AC インピーダンス法によって経時的に測定した．なお，FIB の腐食判定基準 (0.2 μA/cm^2)から供試体中鉄筋の腐食を判定した．

(5)　腐食発生限界 Cl^- 量

腐食電流密度から腐食したとみなされたモルタル供試体の鉄筋近傍のモルタル中の Cl^- 量を JCI-SC45 に従って分析し，コンクリート中の Cl^- 量に変換して算出した結果を腐食発生限界 Cl^- 量とした．

2.4 寿命予測方法

本研究における寿命の定義を図1に示す．塩害と中性化における潜伏期を算出する為に Cl^- 拡散係数，中性化速度係数，酸素透過量を把握した．なお，塩害環境の進展期の算出を行う為に，腐食速度と酸素透過量の関係式[4]及び鳥取式[5]を用いた．

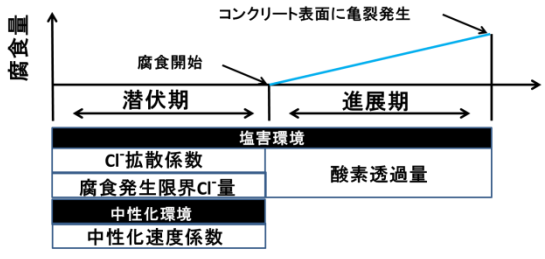

図1. コンクリートの寿命

3 実験結果

表3. 各配合の物性値の実験結果

呼び記号	Cl^- 拡散係数, (cm^2/year)	中性化速度係数, (mm/√週)	酸素透過量, (nmol・cm^2/sec)	腐食発生限界Cl^-量, (kg/m^3)
0.5OPC-W	3.6	0.08	0.039	5.5
0.5OPC-S	2.2	0.14	0.035	
0.5能代(Ⅱ)FA10-W	1.9	0.23	0.012	4.9
0.5能代(Ⅱ)FA10-S	1.2	0.23	0.012	
0.5能代(Ⅱ)FA30-W	1.0	0.45	0.005	5.2
0.5能代(Ⅱ)FA30-S	0.6	0.38	0.006	
0.5勿来(Ⅱ)FA30-W	1.1	0.53	0.012	5.3
0.5勿来(Ⅱ)FA30-S	0.8	0.47	0.009	
0.5相馬(×)FA30-W	1.8	0.51	0.018	3.9
0.5相馬(×)FA30-S	0.8	0.23	0.013	
0.7OPC-W	3.6	0.45	0.034	4.3
0.7OPC-S	2.9	0.55	0.038	
0.7能代(Ⅱ)FA30-W	2.4	1.10	0.012	3.7
0.7能代(Ⅱ)FA30-S	1.8	0.80	0.006	

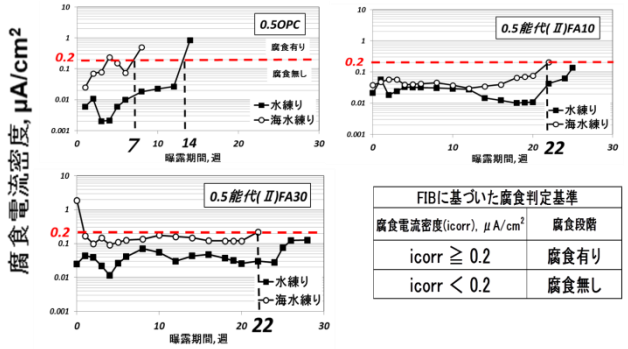

図2. モルタル中の鉄筋の腐食挙動

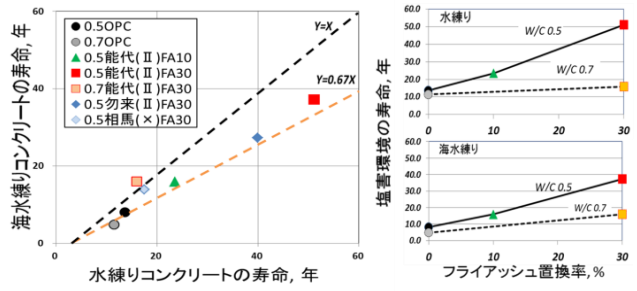

図3. 塩害環境の寿命 (潜伏期と進展期の和), 鉄筋かぶり70mm

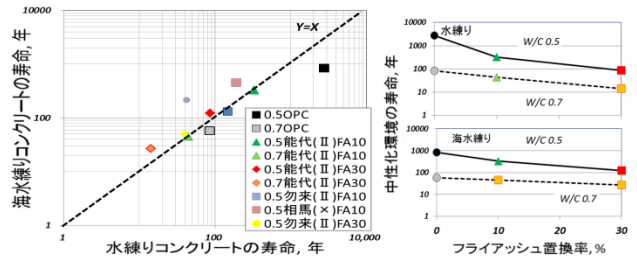

図4. 中性化環境の寿命 (潜伏期), 鉄筋かぶり30mm

3.1 物性値

表3は各配合の物性値の実験結果である.

(1) Cl^-拡散係数

海水練りした場合の Cl^- 拡散係数は水練りした場合よりも小さくなることが確認された. これは海水練りの初期混入 Cl^- が濃度勾配を緩やかにしたためと考えられる. また, FA を混和した場合の Cl^- 拡散係数は OPC と比べ小さくなることが確認され, FA のポゾラン反応による緻密化の可能性が示唆された.

(2) 中性化速度係数

海水練りした場合の中性化速度係数は水練りした場合と概ね同じになることが確認された. また, FA を混和した場合の中性化速度係数は OPC よりも大きくなる. これは, FA を混和した場合 pH は OPC よりも低くなるためだと考えられる.

(3) 酸素透過量

海水練りの酸素透過量は水練りと概ね同じであり, FA の酸素透過量は OPC に比べ小さくなることが確認され, FA のポゾラン反応による緻密化の可能性が示唆された.

(4) 腐食発生限界 Cl^- 量

FA を混和した場合の腐食発生限界 Cl^- は OPC と比べ小さくなった. これは, FA を混和した場合の pH は OPC よりも低くなるためだと考えられる.

3.2 腐食挙動

図2は塩害におけるモルタル中の鉄筋の腐食挙動である.

海水練りした場合の腐食発生は水練りより早い. 一方, FA を混和した場合の腐食発生は練混ぜ水によらず水練りした OPC より遅いことが確認された. これは FA を混和した場合の Cl^- 拡散係数が OPC の3分の1以下であるためと考えられる.

3.3 寿命予測

図3は塩害における, 図4は中性化における寿命予測である.

(1) 塩害における寿命予測

図3の結果から, 練混ぜ水に海水を使用すると水練りした同配合に比べて塩害における寿命は短くなる. これは初期混入塩分が存在するためであると考えられる. 一方, 海水練りした, FA を混和した海水練り鉄筋コンクリートの寿命は FA 置換率の増加に伴い水練りした OPC よりも長くなることが確認された. これは, Cl^- 拡散係数と酸素透過量が FA 置換率の増加に伴い小さくなることで潜伏期と進展期が伸びたためと考えられる. 特に水セメント比0.5の場合, FAⅡ種を30%置換した海水練りの配合は長い寿命を示し, 約30年であった. (能代と勿来の平均値)

(2) 中性化における寿命予測

図4の結果から, 練混ぜ水に海水を使用すると水練りした場合の寿命と概ね同じとなる. FA を混和した海水練り鉄筋コンクリートの寿命は FA 置換率の増加に伴い水練りした OPC よりも短くなることが確認された. FA を混和した配合の中性化速度係数は同配合の OPC と比べて大きくなったためと考えられる.

4 結論

本研究から以下の結論が得られた.

(1) FA を使用することにより, 塩害における海水練り鉄筋コンクリートの寿命(ひび割れ発生まで)を, OPC を用いた水練りコンクリートよりも長期化する可能性が示唆された. 特に水セメント比0.5の場合, JIS 規定の FAⅡ種を30%置換した海水練りの配合は最も長い寿命を示し, その値は約30年となった.

(2) 中性化における寿命(潜伏期)での海水練りと水練りの差は小さかった. しかし, FA を使用することで中性化速度が早くなるため, 鉄筋かぶりを大きくするなどの対策が必要である.

参考文献

1) 小原弘毅, 塩害および中性化における海水練りコンクリートの寿命予測, 東京工業大学大学院修士論文, 2013
2) 魚本健人・高田良章, コンクリートの中性化速度に及ぼす炭酸ガス濃度の影響, 生産研究, 43巻6号, pp. 35-pp. 38, 1991. 6
3) 堺 孝司, 開発土木研究所月報, No. 457, pp. 39-41, 1991. 6
4) 鳥取誠一, 鉄筋腐食に関する暴露試験等に基づいたコンクリート構造物の劣化予測, 京都大学学位論文, 2002
5) 丸山真一, 中性化によるコンクリート中鉄筋の腐食に及ぼすセメントおよび温度の影響, 東京工業大学学位論文 2002

Feasibility Study of FOSS GIS:
A case of World Heritage Site in Luang Prabang, LaoP.D.R

Student number: 10_06016 Name: Ryusuke Katagiri
Supervisor: Yume Yamaguchi, Junichi Takada

1 Introduction

Town of Luang Prabang was inscribed as World Heritage thanks to its unique townscape. However, UNESCO monitoring report indicates that the rapid development is gradually changing the townscape. Therefore, the town may be at the risk of being enlisted as heritage in danger in the near future. (Kami.2010) Tech team has been collaborating with the local government of Luang Prabang, The world heritage site of Lao PDR, by introducing applicable information and communication technology to assist sustainable development of the town.

To assist in finding possible solution to tackle this problem, usage of GIS (Geographic Information System) was identified as a potential means with the aim to visualize and analyze the changes in the townscape after World Heritage inscription. The project team used ArcGIS, commercial software, for development of GIS prototype in the past, however, annual license fee has become burden for the local institution. If Lao PDR decides to join WTO, along with its advantages such as loosen custom, no quantity limitation for items, it would also influence on stricter regulation on pirated software. Due to high cost for commercial software the usage of illegal software is common issue in developing countries. Thus, the need of FOSS (free and open source software) GIS is expected to be further highlighted with particular attention on cost and legality. Kami (2010) who was project team member conducted the feasibility study of FOSS GIS, but almost all the software packages are renewed and there are new software packages born. In this context, this study aims to investigate feasibility of FOSS GIS use in Luang Prabang.

2 Objectives of this research

The objectives of this research are: 1) to select an appropriate FOSS GIS to be used to manage the core preservation areas of Luang Prabang; 2) to conduct testing the use of selected FOSS GIS using the training manual; and 3) to evaluate the test result and to suggest the improvement.

3 Over view of GIS

Geographic Information System (GIS) integrates hardware, software, and data for capturing, managing analysis, and displaying all forms of geographically referenced information (Mattay et al., 2006).

3.1 ArcGIS

ArcGIS is the most popular GIS software in the world. Its share is about 36 percent in GIS software in 2008 and it is larger than any other software. It has easy user interface, rich function in editing maps and geo analysis, good user support. In addition to that, it becomes easy to share data with other department that use ArcGIS due to its biggest share in market.

3.2 QGIS

QGIS is FOSS (Free and Open Source Software) GIS. The strongest advantage of QGIS is its user interface. QGIS has user-friendly interface that is similar to ArcGIS, therefore users who have ever used ArcGIS before can easily use QGIS as well. The second advantage is GRASS plugin modules. By using the GRASS plugins, QGIS is able to operate many analyses function of GRASS. Other than GRASS tool kit, QGIS has many plugins.

4 Study framework

The study investigated the feasibility of FOSS GIS to be used in Luang Prabang using the following steps: 1) identifying important FOSS GIS functions and features; 2) specifying suitable FOSS GIS through comparison among different software packages 3 times; 3) comparing QGIS with ArcGIS and clarifying QGIS advantage and disadvantages in the project; 4) identifying the appropriate task for testing; 5) creating manual to manage a specific function on QGIS; 6) conduct testing on QGIS; and 7) to evaluate the use of QGIS and improve manual. At last, revised manual was sent to local staff members for their feedback.

5 Results

5.1 Needs for screening

First, this study identified important functions and features requested for FOSS GIS to the project. Thus, the important functions were identified with the local team members, including; 1) Editor, 2) Attribute calculation, 3) Symbol, 4) GEO analysis, 5) Geo referencing, 6) GPS. And important features were also identified with priorities, including; 1) Programming language, 2) Level of complexity, 3) Maturity, 4) Compatible user interface with ArcGIS, 5) Abundant functions, 6) Support of various data format, and 7) Easy installation and test running. In these features, they put high priority on 2) Level of complexity, 3) maturity, 5) abundant functions and 7) easy installation and test running.

5.2 Results of screening

Then first FOSS GIS selection was done. 21 software packages were selected from over 100 software packages by considering 3 conditions;(a) General purpose of Desktop GIS applications, (b) currently active or not and (c) Operating system is Windows.

In the second FOSS GIS selection, 8 software packages are selected from 21 packages by considering 2 conditions; (a) Sufficient functionalities as a desktop GIS system (b) Popularity of the software. 8 software packages are GRASS, gvSIG, ILWIS, MapWindow GIS, OpenJUMP, QGIS, SAGA GIS, and uDig.

In the third FOSS GIS selection, QGIS was selected as most potential software package by considering these conditions; (a) Check required

functions by creating comparison table, (b) Simple test running and (c) Refer other comparison tables.

5.3 Comparison between ArcGIS and QGIS

To investigate feasibility of QGIS, its advantages and disadvantages against ArcGIS are discussed by revising some useful sites. As advantages of QGIS, license fee, legality issue and user support were identified. As disadvantages of QGIS, lack of calculation function in attribute table, fewer map adjustment and edit functions and fewer geo analysis functions were discussed.

5.4 Testing with appropriate task using QGIS

Before the testing of QGIS, local staff members identified two important and useful functions: 1) distance calculation function; and 2) function of creating contour. First, distance calculation function as employed using ArcGIS and QGIS in the map given by local staffs. But there are almost no difference regarding its function. And second, Function of creating contour is especially needed, mainly because of 2 reasons; 1) Local staffs can't use this function on ArcGIS due to license problem. 2) There are few training sources of QGIS, because it is not commercial software. Thus, the task using QGIS was decided on "creating contour line on QGIS".

5.5 Results of testing

As a next step, training manual for creating contour lines on QGIS was created. Further, nine questions to evaluate and improve this manual were asked. As a sample DEM file, a file "Laos_dtm" was used to create contour lines. The author let 10 examinees to create contour lines by referring manual and recorded their background, time to finish manual and frequency of question.

The results are showed in the table below.

Participant	Age	Major in university	GIS Experience	Time(minutes)	frequency of question
E1	20s	IDE	None	15	0
E2	40s	The faculty of literature	None	16	2
E3	20s	Electronics	None	15	1
E4	20s	Information engineering	None	11	0
E5	20s	IDE	None	20	4
E6	20s	Library information	3 months	15	0
E7	20s	IDE	None	18	2
E8	20s	IDE	None	13	0
E9	20s	Mechanical Engineering	1 month	10	0
E10	20s	IDE	None	15	2

Table 1 Summary of test result
(source: compiled by the author, February, 2014)

Based on the data collected, the analysis was conducted using the following three points: 1) possibility of using QGIS; 2) usability of QGIS; and 3) improvement of this manual. The test result may be interpreted that DPL staff members with less experience of using GIS are able to create contour lines easily. Because, including examinees without experience of GIS, six out of 10 examinees finished all the procedure without any questions during the testing.

With the testing, some useful suggestions were identified to make this manual more comprehensive. The following points were incorporatead for revised manual: 1) to arrange procedures and pictures alternately; 2) to indicate time to load something or finish each procedure; and 3) to explain each operations meaning simply by using glossary. On the basis of these suggestions, revised training manual was created and send to local staff members.

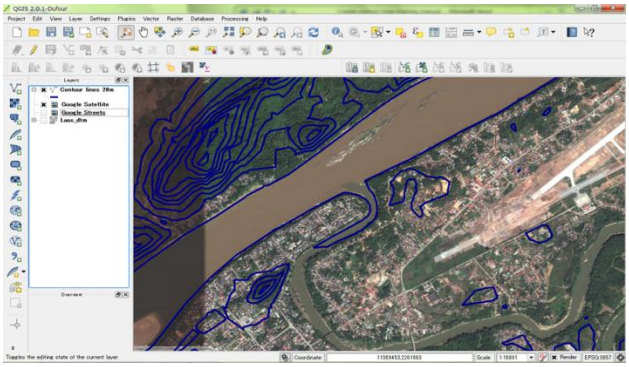

Figure 1 Creating contour lines using QGIS
(Source: Created by author, February, 2014)

6 Conclusions

In summary, this study investigated the feasibility of FOSS GIS to be used in Luang Prabang.
QGIS performed well under the existing condition and its functions are adequate for local needs. By the test running, function of creating contour lines is confirmed to work on QGIS and the manual to create contour lines was evaluated to be useful.
It is believed that QGIS might be effective and useful tool for the project in Luang Prabang. It is hoped that this study can support usage of FOSS GIS in the other project by selecting the most feasible FOSS GIS to cope with problems in implementing and sustainable usage.

References

[1] Yoshitaka Kami "Feasibility Study of Open Source GIS Application for World Heritage Management in Luang Prabang, Lao PDR", 2010
[2] Neftali Sillero, Pedro Tarroso," Free GIS for herpetologists: free data sources on Internet and comparison analysis of proprietary and free/open source software", 2009
[3] Stud.techn. Atle Frenvik Sveen, "Use of Free and Open Source GIS in Commercial Firms", 2008
[4] Stefan Steiniger , Geoffrey J. Hay, "Free and open source geographic information tools for landscape ecology",2009
[5] Geoffrey Anderson, Cloudshadow Consulting, Inc, Boulder, Colorado "Building Web-Based Spatial Information Solutions around Open Specifications and Open Source Software"2003

Study on charging method for enhancing
charge-discharge efficiency of Ni-MH battery

Student Number: 10-08593 Name: Kenta Koh Supervisor: Kunio Takahashi

1 Introduction

Energy harvesting is a technique for gathering tiny energy from environments such as light, vibration, heat, and electromagnetic waves. It is used for small devices such as wireless network sensor. Energy obtained from energy harvesting is unstable so that we cannot use this energy directly. So we have to store those energy before use. In our lab, we used capacitors as storage devices because of their advantage of charge discharge efficiency. But capacitors have disadvantages compared to rechargeable battery from the point of leak current, discharge characteristic and so on. So the possible of using battery has to be discussed.

In the past, the effect of pulse charging on inner pressure and cycling characteristics of Ni-MH batteries is studied by Jixiao Zhang et al [1]. But charging efficiency has not been discussed.

The purpose of this study is to clarify the effect of pulse charging on charge-discharge efficiency and study charging method. To attain this purpose, the following procedures are taken.

1) Measuring voltage and current for both constant current and pulse charging.
2) Referring to the measurement result for constant charging current, charge-discharge efficiency for pulse charging in analyzed to investigate the effect of duty ratio and magnitude of pulse charging current on charge-discharge efficiency.
3) Studying charging method considering control loss.

2 Experiment condition

2.1 Battery condition

I use a Ni-MH battery which has been used less than 50 cycles. Its storage is 1900mAh.

2.2 charging condition

Battery is charged 160% of capacity and discharge 100% of capacity in case of full charging [3].

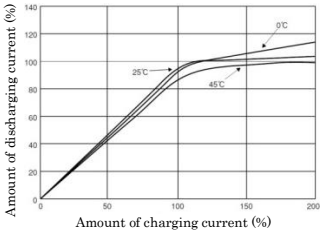

Fig1 Efficiency of amount of current

But looking at Fig1, battery cannot be charged when the amount of charging current is over 100% of storage. So I charge battery up to 53% of storage i.e.1Ah in all experiments.

2.3 Discharging condition

The battery is discharged at the current of 160mA until its voltage decreases to 1V. After discharging, battery's voltage is recovered gradually. So I start all charging experiment when battery's voltage is recovered up to 1.2V.

3 Constant current charging experiment

3.1Experiment parameter

In this experiment, charging current is constant. Fig2 shows charge-discharge circuit. I set I_1,I_2,t_1,t_2 and measure V_1, V_2.

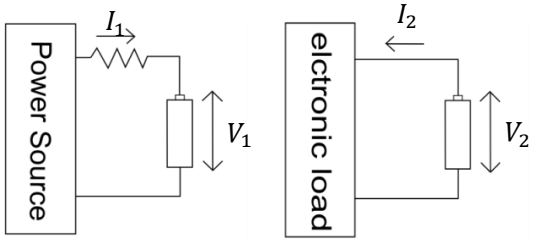

Fig2 Charge-discharge circuit

t_1: charging time t_2: discharging time

E_1: charging energy ($=\int_0^{t_1} I_1 V_1 dt$)

E_2: discharging energy ($=\int_0^{t_2} I_2 V_2 dt$)

η_1: charge-discharge efficiency ($=\frac{E_2}{E_1}$)

3.2 Result

Fig3 shows relation of current and charge-discharge efficiency.

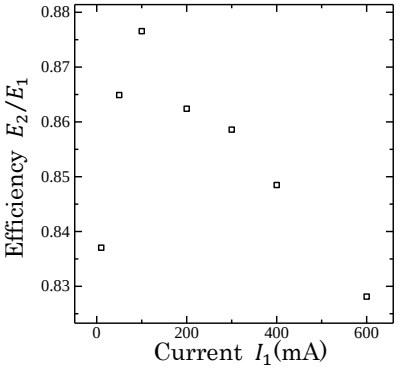

Fig3 Charge-discharge efficiency

Next, doing pulse charging experiment, I set current and duty ratio based on this result

4 Pulse charging experiment

4.1 Experiment parameter

In this experiment, the charging current is pulse. Fig4 shows definition of duty ratio.

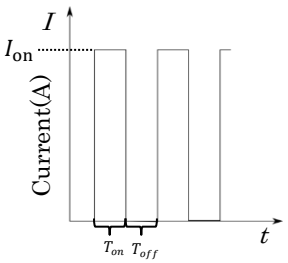

Fig4 example of pulse charging

d: duty ratio ($=\frac{T_{on}}{T_{on}+T_{off}}$)

η_2: efficiency ($=\frac{E_2}{E_1}$)

I decide I_{on} so that it becomes the average of amount of current is equal as shown equation.

$\frac{1}{T_{on}+T_{off}}\int_0^{T_{on}+T_{off}} I_3\,dt = 100(\mathrm{C})$

So I set current and duty ratio as Table1 and measure efficiency shown.

Table1 Measurement plan

I_{on}	T_{on}	T_{off}	d
200mA	1sec	1sec	1/2
300mA	1sec	2sec	1/3
400mA	1sec	3sec	1/4
500mA	1sec	4sec	1/5
600mA	1sec	5sec	1/6

4.2 Result

Fig5 shows charge-discharge efficiency.

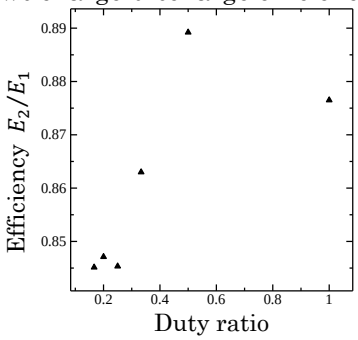

Fig5 Charge-discharge efficiency

There is a duty ratio which optimizes charge-discharge efficiency. In next discussion, I use this data in the next discussion.

5 Discussions

I propose pulse charging circuit with FET like Fig6. I set duty ratio with controlling frequency of FET switching. Energy losses by using FET are heat which is generated in resistor between drain and source R_{DS}, gate drive loss, switching loss.

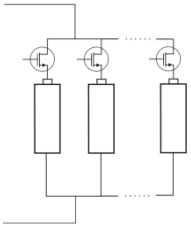
Fig6 pulse charging circuit with FET.

To compare charging method, I set charging circuit like Fig7.

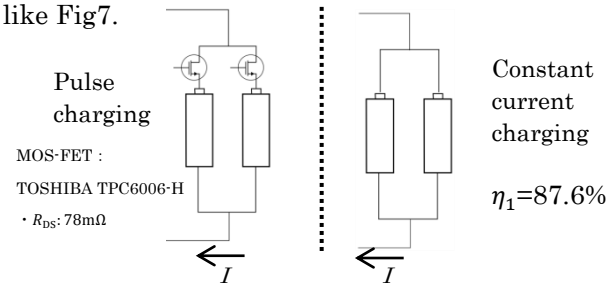

Fig7 Comparing two charging method

The current I is 200mA and duty ratio is 1/2 to reproduce pulse charging experiment.

The charge-discharge efficiency considering energy loss is 87.9%. Energy loss is decided by R_{DS} if FET's switching frequency is less than 1kHz.

So, if we choose FET whose R_{DS} is small and charge battery with optimum duty ratio, there is some possibility using pulse charging to enhance charge-discharge efficiency.

7 Conclusions

Measurement result shows that we should choose battery's capacity appropriately.

There is a duty ratio which optimizes charge-discharge efficiency.

There is some possibility using pulse charging to enhance charge-discharge efficiency.

8 References

[1]Jixiao Zhang, Jingxian Yu," The effects of pulse charging on inner pressure and cycling characteristics of sealed Ni/MH batteries", Journal of Power Sources,Volume 136, Issue 1, 10 September 2004, Pages 180–185

[2]AIS-Panasonic, Pages for juridical person, Information of Ni-MH, 第 1 章"ニッケル水素電池の 5 大特性"

[3]AIS-Panasonic, Pages for juridical person, Information of Ni-MH, 第 3 章"充電方法について"

中国における高速鉄道と航空の旅客特性と機関選択

学籍番号：10_08601　　氏名：康　書陽　　指導教官：花岡　伸也

1　はじめに

中国では 2003 年に初めて旅客専用線の高速鉄道（時速は 200km/h 以上）が開通後、2011 年以降に北京・上海間（1,318km）や北京・広州間（2,298km）など次々に新しい高速鉄道（時速は 300km/h 以上）が開通し、2013 年 9 月時点で約 10,500km が運用されている。2008 年に修正された中長期鉄道網計画によると、四縦四横の旅客専用線、都市間鉄道、高速化された在来線、西部開発のための新線、海峡西岸線の 5 種類の高速列車に対応した鉄道があり、2015 年まで約 18,000km が計画されている。

高速鉄道の開通後、競合する航空路線の運休や減便が生じている。例えば、大手航空会社の鄭州・西安間（505km）の航空路線は、2010 年に高速鉄道（時速は 300km/h 以上）の開通後に、2 社運休となった。石家庄・太原間などの 300-700km 区間も航空路線の減便が起きている。今後国内航空路線の需要の一部は高速鉄道に代わっていくものと考えられる。

高速鉄道と航空の旅客特性及び機関選択モデルの推定事例は今までいくつかあるものの、中国を対象とした事例は少ない。そこで、本研究では複数の高速鉄道路線があり、競合する航空路線の多い北京をケーススタディとして、行動調査（RP 調査）と選好調査（SP 調査）を用いて高速鉄道と航空の旅客特性の分析及び機関選択モデルを推定とする。

2　現地調査

本研究では、北京で 2013 年 12 月に現地調査を行った。北京を起終点とする高速鉄道は、北京駅から発車する北京－瀋陽－哈爾浜を結ぶ内陸北向きの京哈線、北京西駅から発車する北京－鄭州－武漢を結ぶ内陸西向きの京広線、さらに北京南駅から発車する北京－南京－上海を結ぶ内陸南向きの京滬線があり、いずれも四縦四横の一つである。これらの路線の高速鉄道の停車駅があり、かつ北京の首都空港から航空路線のある都市として、上海、杭州、南京、西安、武漢、鄭州、済南、太原、瀋陽、長春、青島、合肥の 12 都市を選んだ。

RP 調査は北京駅、北京西駅、北京南駅の駅構内の待合室、北京首都空港のチェックインカウンター付近で行った。SP 調査は北京地元の住民を対象に、企業、大学及びインターネットで調査を行った。各調査地点のサンプル数が均一になるように収集し（目標値 RP600、SP200）、合計 840 サンプルを集めた。その後、機関選択モデルに利用可能なサンプルを精査し、有効サンプル数は 744 となった。

調査票の言語は中国語で、調査項目は、モデル変数に反映することを想定し、次の項目を質問した。RP 調査の場合は社会属性（性別、年齢、職業、家族月収）、目的地、旅行目的、ラインホール運賃、出発地住所、アクセス手段、アクセス時間、アクセス費用、日帰りかどうか、高速鉄道・航空の選択理由、全部で 14 問である。SP 調査の場合は社会属性（性別、年齢、職業、家族月収）、三段階の距離別における交通機関に対する選択傾向、全部で 7 問である。

3　旅客特性分析

RP 調査のアンケート回答者の中で、高速鉄道を利用するのは 267 人で、航空を利用するのは 265 人である。回答者の多数は企業の従業員、学生、個人経営者である。高速鉄道を利用する 35 歳以上の人の割合は 48%の一方、航空の場合は 22%しかない。家族月収は 4 段階の選択式で回答を得て（1 元＝約 17 円）、高速鉄道の 37%が 0~5000 元、32%が 5000~10000 元、31%が 10000 元以上である。一方、航空の 28%が 0~5000 元、45%が 5000~10000 元、27%が 10000 元以上である。これより、高速鉄道と航空の主要旅客の所得階層があまり異なっていないことがわかる。

片道運賃を旅行目的別、方面別で分析した。高速鉄道の運賃は原則的に営業距離に比例し、割引制度もないが、一等車と二等車に分けられる。一部の旅客は相対的に高い運賃の一等車を利用しているが、それでも航空運賃の 2 分の 1 以下である。一方、航空運賃の分散は大きく、営業距離にも比例しない。特に、北京と最も近い目的地、済南までの航空運賃は最も高い。

旅行目的は高速鉄道と航空で顕著な違いはなかった。出張、旅行、帰省のシェアが高かった。業務目的は`高速鉄道と航空のいずれも約 40%を占めた。

アクセス手段については、業務旅客のほうがそれ以外の目的の旅客よりもタクシーを利用する人が多い。空港までの交通手段の選択は、業務旅行の 55%と非業務旅行の 30%の人が自動車かタクシーを利用したことがわかる。

次に、業務旅行と非業務旅行に分けて、高速鉄道利用者に高速鉄道を利用する理由と航空を利用しない理由、航空利用者に航空を利用する理由と高速鉄道を利用しない理由を分析した。高速鉄道利用者では、短いアクセス時間と適切な出発時間を選択条件とした結果が最も多かった。一方、航空利用者は短いラインホール時間を選択している回答が最も多かった。さらに、業務旅行では、職場決定と高

い定時運行率を決定要素として選択する人が多く、非業務旅行では、低運賃を重視している人が多いことがわかる。

SP 調査では一人の回答者から中距離（400~700 km）、中長距離（700~1000 km）、長距離（1000~1300 km）におけるサンプル 3 つが得られる。回答者は全部 212 人で、公務員、事業者、企業の従業員の割合が最も高い。16~35 歳の回答者は 60%以上を占める。35 歳以上の航空を利用したい人は高速鉄道を利用したい人より少ないが、その差は RP データより小さい。家族月収については、高速鉄道と航空を利用したい人の各レベルの数はあまり差がなく、0~10000 元レベルが 80%を占める。

高速鉄道や航空に対する選択傾向は業務や非業務目的に分けられる。いずれにおいても、距離が長いほど、航空を選ぶ人の割合が高くなる。業務旅行において航空を利用したい人は非業務旅行の約 2 倍で、非業務旅行の高速鉄道を利用したい人は業務旅行の約 1.5 倍である。

次に、選択傾向に対する理由を分析した。業務旅行の場合、約 50%の人はラインホール時間、約 25%の人は快適性を重視して航空を選んだ。その一方、約 30%の人はラインホール時間、約 20%の人は安全性と定時運行率を重視し、高速鉄道を選択した。非業務旅行では、約 35%の人はラインホール時間と快適性を重視し、航空を選んだ。約 35%の人は運賃、約 15%の人はラインホール時間、安全性と快適性を重視して、高速鉄道を選択した。

4 機関選択モデル推定

本研究では、RP データから、高速鉄道、航空の 2 選択肢による非集計選択モデルの二項ロジットモデル（BL）を用いて機関選択モデルを推定する。さらにアクセス方法を車・タクシーと公共交通機関に分けて、多項ロジットモデル（MNL）を用いて推定する。推定結果を表 1 と表 2 に示す。

表 1　業務旅行機関選択モデル推定結果

	BL		MNL	
説明変数	推定値	t 値	推定値	t 値
アクセス運賃	0.0872	3.21	0.0724	5.07
アクセス時間	-0.130	-3.43	-0.232	-17.6
便数	0.016	2.06	0.014	1.85
ラインホール運賃	0.0001	0.14	0.0001	0.03
ラインホール時間	0.0002	0.05	0.0001	0.01
固有定数（空港）	2.75	2.58	-	-
固有定数（空港・車）	-	-	4.66	11.33
固有定数（空港・公共）	-	-	10.0	0.00
固有定数（駅・公共）	-	-	2.84	0.244
修正 ρ^2	0.312		0.299	
サンプル数	277			

表 2　非業務旅行機関選択モデル推定結果

	BL		MNL	
説明変数	推定値	t 値	推定値	t 値
アクセス運賃	0.0642	4.23	0.0973	6.68
アクセス時間	-0.05	-1.97	-0.03	-0.71
便数	0.024	2.85	0.023	2.81
ラインホール運賃	0.0003	0.62	0.0004	0.73
ラインホール時間	0.0004	0.12	0.0002	0.05
固有定数（空港）	0.553	0.65	-	-
固有定数（空港・車）	-	-	0.0364	0.03
固有定数（空港・公共）	-	-	-0.095	-0.04
固有定数（駅・公共）	-	-	1.08	1.95
修正 ρ^2	0.246		0.312	
サンプル数	305			

アクセス時間と便数は説明変数として統計的に有意な結果を得て、高速鉄道選択理由と一致している。アクセス運賃の t 値が大きいものの、符号条件が合わない。そのほかに、ラインホール時間、ラインホール運賃、月収、駅・空港での待ち時間などを説明変数として検討したものの、どれも t 値が小さく、符号条件が合わないケースもあり、統計的に有意な結果とならなかった。

5 結論

本研究では、北京で現地調査を行い、集めた RP と SP のデータを用いて高速鉄道と航空の旅客特性を分析し、RP データのみで機関選択モデルの推定を行った。修正 ρ^2 の値が十分高いことから、モデルの説明力があるとわかった。モデルは実情をある程度反映しているものの、サンプル比率が実態と一致しているかどうか不明なことから、ラインホール運賃とラインホール時間などの説明変数に影響している。サンプリングを注目し、モデル改善の余地がある。

参考文献

[1] Zheng Zhao, “The Analysis about the Impact of the High-speed Railway Operation on Civil Aviation” (2009)

[2] Yi Liu, “The Impact of High-speed Railway on Civil Aviation Transportation Industry” (2013)

[3] “Year Book of China Transportation & Communications” (2013)

[4] Japan Society of Traffic Engineers “Disaggregate Travel Demand Analysis” (2013)

Transport Infrastructure and the Location of Industrial Estates: Thailand experience

Student Number: 10-09842 Name: Wataru Saito Supervisor: Shinya Hanaoka

1 Introduction

The number of industrial estates in Thailand has been increasing as industrial structure transferred from primary to secondary in 1980's. Foreign Direct Investment (FDI) to Thailand's manufacturing industry has been increasing as well, and most of foreign firms have moved into industrial estate to get some profits by agglomeration effect. It can clearly be seen that transport infrastructure is one important factor when firms decide their location.

There are more industrial estates in Thailand than neighboring countries, but labor costs in Thailand has been increasing so we can predict some firms will move their location to Laos, Cambodia or Myanmar. Moreover, many official agencies has invested in Greater Mekong Subregion (GMS) so it is useful to research about relationship between industrial location and transport infrastructure in Thailand at the first setout for forecasting logistics of GMS.

This research attempts to identify the impact of transport infrastructure factors on location of industrial estates in Thailand.

2 Industrial Estates in Thailand

This section explains the chronological transition of industrial estates' location in Thailand to understand what kind of transport infrastructure is important. The official website of "The Board of Investment in Thailand (BOI)" shows 60 industrial estates. It is assumed that these 60 ones reflect the tendency of whole industrial estates' location in Thailand. Figure 1 and Table 1 show chronological transition of Thailand industrial estates. Asian Highway are shown by bold line on Figure 1.The numbers on Figure 1 correspond to Table 1.

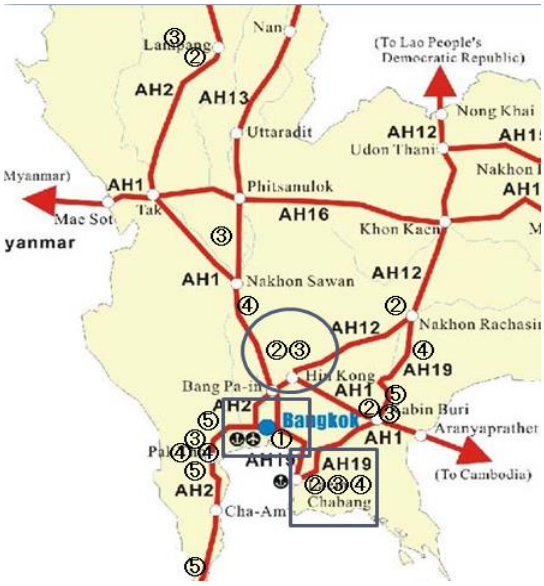

Figure 1: Map of location transition

Table 1: Location transition: number and area

	Completion age	Num of IE	located area
①	1970s	5	Bangkok
②	1980s	12	East area(Near to Leam Chabang port)
③	1990s	23	
④	2000s	13	Regional city(far from Bangkok)
⑤	2010s	7	West area, not central area

Due to promotion act in investing in regional area of Thailand since 1987, some industrial estates decided to locate farer from Bangkok in order to obtain the benefits of tax reduction.

In addition, because of 'Thailand Floods 2011' and recent democratization in Myanmar, several industrial estates locate rather in west area than in central area. Furthermore, as shown in Figure 1, many of them are located along the main road or near to the port. We can assume that road and port are one of important factors.

3 Methodology and Results

3.1 Model and data

To identify the impact on the location from transport infrastructure, this research applies multiple regression analysis. Linear regression model and variables are proposed as following:

Table 2: Independent variables: Definition, mean, standard deviation and expected effect

	Variable	Definition(unit)[data year]	mean	standard deviation	expected effect
transport	DisBangkok	Distance(km) to Bangkok which is the main market	248	306	−
	Dis Port	Distance(km) to the nearest main port	197	171	−
	Lane	Road length(km) which has only 2 lanes to go to Bangkok and Port[2008]	32	48	−
	Surface	Road length(km) which is in bad surface condition to go to Bangkok and Port[2008]	5	13	−
non-transport	BOI	Dummy variable with value 1 if the province lies in BOI zone 3,value 0 for others	0.39	0.49	+
	EMP	Number of employees who is working on secondary industry in the province[2008]	101,416	162,053	+
	Wages	Minimum wages(baht/day)[2008]	169	17	−
	Fee(IE)	Average Maintainance fee of General Industrial Zone(baht/area/month)[2010]	762	150	−

$$\text{Sum Size(IE)}_p = \beta_1 \text{DisBangkok}_p + \beta_2 \text{DisPort}_p + \beta_3 \text{Lane}_p + \beta_4 \text{Surface}_p + \beta_5 \text{BOI}_p + \beta_6 \text{EMP}_p + \beta_7 \text{Wages}_p + \beta_8 \text{Fee(IE)}_p + C \quad (1)$$

where Sum Size(IE)_p is the total industrial area (km^2) of industrial estates located in each province (p).This refers to the number of firms located in industrial estates indirectly. Samples are 18 provinces after 55 industrial estates (by 2010 before 'Thailand Floods 2011') are synthesized. $\beta_{(1-8)}$ are parameters to be estimated and C is a constant. From previous studies and section 2, this research set independent variables which are explained in Table 2. Independent variables divided into transport and non-transport variable. 'Lane' and 'Surface' are referred to UNESCAP Asian Highway Database. As for 'BOI', Thailand divides the country into 3 zones by different level of investment incentive. 'Fee(IE)' is representing the land price indirectly.

3.2 Results

Correlation coefficients among independent variable are less than 0.8 except 'Dis Port' and 'Surface'. Coefficient of 'Surface' has less effect (−) than 'Dis Port' when they are included so 'Surface' is omitted. Coefficient of 'EMP'(+) is the smallest and less than 0.1 so it is omitted as well. The result of the regression model is shown in Table 3.

From this result, we can say that all of the signs (+ or −) are corresponding to our expectation. 3 transport infrastructure variables except 'Surface' have significance. In contrast, 'BOI' is the only variable which has significance among non-transport. This explains that Thailand's investment promotion act has an influence on the location of industrial estates. When omitting one of 3 transport variables, adjusted R square decreases dramatically from 0.36 to less than 0.2, so those transport infrastructure variables are definitely important.

Table 3: Result of the regression analysis

	Variable	standardized regression coefficient	t-Value significant level *10% **5%
transport	Dis Bangkok	-0.820	-2.740**
	Dis Port	-0.746	-2.628**
	Lane	-0.817	-2.057*
non-transport	BOI	0.918	2.671**
	Wages	-0.397	-1.340
	Fee(IE)	-0.256	-0.691
	R square	0.59	
	Adjusted R square	0.36	
	Num of observation	18	

4 Conclusions

This research analyzes the impact on industrial estates' location in Thailand from transport infrastructure. The result states that 'distance to market', 'distance to the main port' and 'the number of road lanes' are the key transport infrastructure factors for location of industrial estates. Further research is required by two aspects: 1) Improve the variables and make a model including time-series information 2) Estimate the future situation of industrial location in GMS by using the model.

References

[1]Adeheid Holl: Transport Infrastructure,agglomeration aconomies, and firm birth: empitical evidence from Portucal,regional science,Vol.44,pp693-712,2004.

[2]JBIC: Investment to Thailand, JBIC report,2012

Effect of geometry of the multi-beam structure on gripping stress

Student Number:10B11431 Name:Shin Shimahara Supervisor:Kunio Takahashi

1 Introduction

Geckos use adhesion to move quickly on a wall and a ceiling. The hairs which geckos have on their toes deform to adhere to a surface and it enable geckos to get enough force to grip on a wall and a ceiling [1]. In order to apply this mechamism to develop a device such as the gecko-inspired tape [2], analysis of adhesion between a micro-nano-hair structure and a rough surface is needed. The effect of an elastic beam on adhesion was investigated in the preceding studies[3] [4], but the effect of geometry (mounting angle and interval between the beams) of a multi-beam structure which consists of a substrate and beams which are fixed on the substrate on adhesion is not investigated. In order to design a device which has the mulit-beam structure, it is needed to analyze the effect of geometry of the multi-beam structure on adhesion.

The objective of this study is the evaluation of the effect of geometry of the multi-beam structure on the maximum gripping stress.

2 Model of the system

Figure.1 shows the model of the multi-beam structure and the rigid body which has rough surface. The elastic beams are fixed on the rigid substrate with the same interval δ and angle θ. $\theta \ll 1$[rad] is assumed. The surface roughness is the triangle wave. Its amplitude is A, the angle of inclination is φ. $2\lambda \gg L$ and $\varphi \ll 1$[rad] is assumed.

Figure.2 shows geometry of the elastic beam. Its length is L, thickness is H, width is W, Young's modulus is E, and moment of inertia of the cross section is I. $H \ll L$ and $W \ll L$ are assumed. H is negligibly thin.

Figure.3 shows the contact process between the multi-beam structure and the rigid body. The multi-beam structure begins to be loaded from $D = \infty$. Loading stops at $D = 0$. Then, the muli-beam structure is unloaded until it detachs perfectly from the rigid body. As $H \ll L$, $W \ll L$, $\theta \ll 1$[rad] and $\varphi \ll 1$[rad] are assumed, the deformation of the beams obeys linear beam theory. As $2\lambda \gg L$ is assumed, the number of the beams which are across inflection point of surface roughness is much smaller than the number of the beam which are not across inflection point of surface roughness. Therefore, the effect of the beams which are across inflection point of surface roughness on adhesion is ignored.

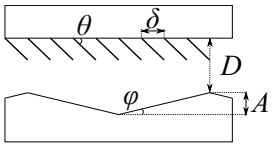

Fig. 1: Multi-beam structure and rigid body

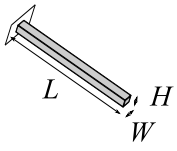

Fig. 2: Elastic beam

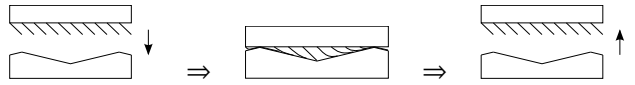

Fig. 3: Contact process

3 Adhesion between the multi-beam structure and the rigid body

The gripping stress σ is obtained as follow.

$$\tilde{\sigma} = \frac{\tilde{F}_{\mathrm{ave}}}{\tilde{\delta}\tilde{W}} \tag{1}$$

F_{ave} is the average gripping force. The gripping stress, the average gripping force, the interval, and the width of the beam are normalized as $\tilde{\sigma} = \frac{\sigma}{12EI/L^4}$, $\tilde{F}_{\mathrm{ave}} = \frac{F_{\mathrm{ave}}}{12EI/L^2}$, $\tilde{\delta} = \frac{\delta}{L}$ and $\tilde{W} = \frac{W}{L}$. δ must be the minimum interval which the beams do not interfere each other to calculate the maximum σ. From Fig.4, δ is obtained as follow.

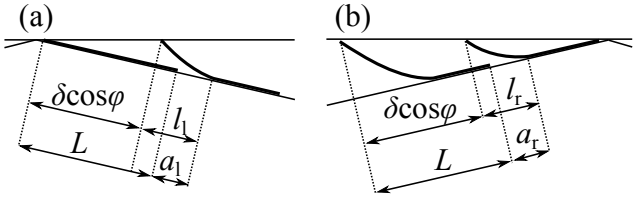

Fig. 4: Geometrical relation at $D = 0$ (a):The contact angle is $\theta - \varphi$ (b):The contact angle is $\theta + \varphi$

$$\delta \cos\varphi = L - l_{\mathrm{l}} + a_{\mathrm{l}} = L - l_{\mathrm{r}} + a_{\mathrm{r}} \tag{2}$$

l_{l} and l_{r} are the length of non-adhesion area. a_l and a_r are the gap between the beams. As δ is the minimum interval which the beams do not interfere each other and H is negligibly thin, a_l or a_r must be 0. At $\theta \le \varphi$, $l_l = l_r = L$ and it results in $\delta = 0$. At $\theta > \varphi$, δ is obtained as follow.

$$\tilde{\delta} = \begin{cases} \left(1 - \dfrac{\sqrt{\left(1+\frac{3\tan\varphi}{\tan(\theta-\varphi)}\right)^2 + 12\frac{\tan\varphi}{\tan(\theta-\varphi)}\frac{\Gamma}{\tan(\theta-\varphi)}} - \left(1+\frac{3\tan\varphi}{\tan(\theta-\varphi)}\right)}{2\frac{\Gamma}{\tan(\theta-\varphi)}}\right)/\cos\varphi & (L - l_{\mathrm{l}} \ge L - l_{\mathrm{r}}) \\ \left(1 - \dfrac{\sqrt{1 + 12\frac{\tan\varphi}{\tan(\theta+\varphi)}\frac{\Gamma}{\tan(\theta+\varphi)}} - 1}{2\frac{\Gamma}{\tan(\theta+\varphi)}}\right)/\cos\varphi & (L - l_{\mathrm{r}} > L - l_{\mathrm{l}}) \end{cases} \tag{3}$$

Γ is the parameter which includes the work of adhesion.

$\tilde{F}_{\mathrm{ave}}$ is obtained by convoluting the force curve of a single beam with the height distribution function of the surface roughness [5].

The maximum gripping stress $\sigma_{\max}$ is the strongest gripping stress at a certain θ.

Relation between the maximum gripping stress $\sigma_{\max}$ and the angle θ is shown in Fig.5, Fig.6 and Fig.7. The amplitude is normalized as $\tilde{A} = \frac{A}{L}$.

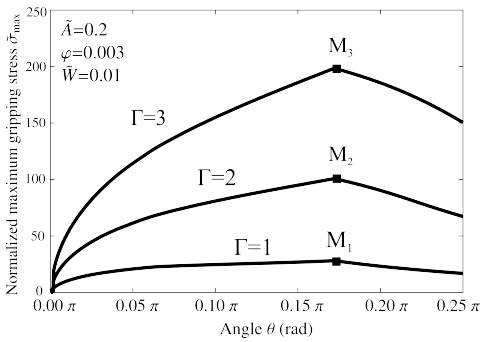

Fig. 5: Relation between the maximum gripping force $\sigma_{\max}$ and the angle θ at different Γ

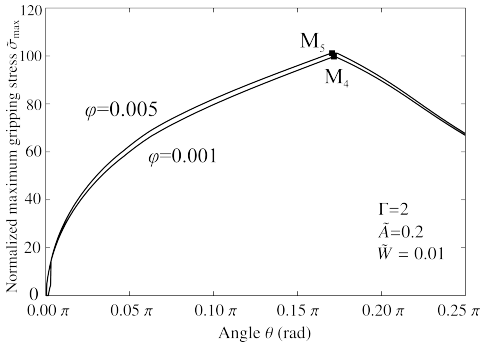

Fig. 6: Relation between the maximum gripping force $\sigma_{\max}$ and the angle θ at different φ

4 Discussion

$M_1 \sim M_8$ in Fig.5$\sim$Fig.7 are the points where the maximum gripping stress is maximal. θ at M_3 and M_6 approach to the minimum angle where all beams adhere at $D = 0$. θ at M_1, M_2, M_4, M_5, M_7 and M_8 approach to the minimum angle where all beams at $\theta - \varphi$ adhere at $D = 0$.

Figure.5$\sim$Figure.7 show that the effect of φ and Γ on the angle where the maximum gripping stress is maximal is much weaker than the effect of $\tilde{A}$.

For those reasons, the angle $\theta_{\max}$ where the maximum gripping stress is maximal is determined from $\tilde{A}$ and it is obtained as follow.

$$\theta_{\max} = \arctan\left(3\tilde{A}\right) \tag{4}$$

$\arctan(3\tilde{A})$ is the angle where all beams adhere in condition of $\varphi = 0$. Figure.8 shows comparison between theoritical $\theta_{\max}$ and equation4. Figure.8 shows that equation(4) is correct.

Furthermore, as δ is obtained by using θ, φ and Γ, the interval $\delta_{\max}$ where the maximum gripping stress is maximal is determined from $\tilde{A}$ by equation(3). Fig.9 shows relation-between $\delta_{\max}$ and $\tilde{A}$.

5 Conclusions

In this paper, adhesion between the multi-beam structure and the rigid body which has rough surface is theoritically investigated. The result shows that the angle and the interval where maximum grippinng stress is maximal are determined from the amplitude of the surface roughness when small deformation is assumed.

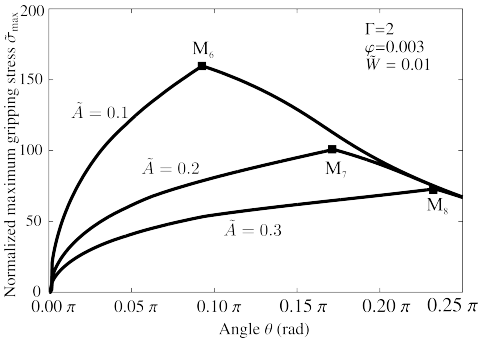

Fig. 7: Relation between the maximum gripping force $\sigma_{\max}$ and the angle θ at different $\tilde{A}$

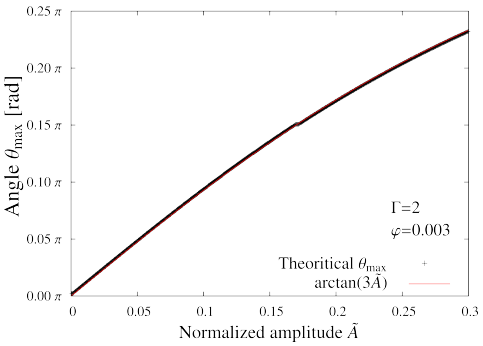

Fig. 8: comparison between theoritical $\theta_{\max}$ and $\arctan(3\tilde{A})$

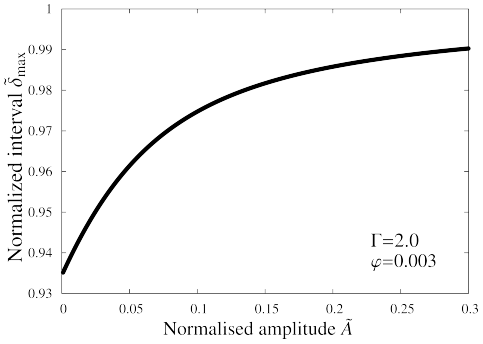

Fig. 9: Relation between $\delta_{\max}$ and $\tilde{A}$

References

[1] Kellar Autumn, Yiching A. Liang, S. Tonia Hsieh, Wolfgang Zesch, Wai Pang Chan, Thomas W. Kenny, Ronald Fearing, Robert J. Full, “ Adhesive force of a single gecko foot-hair”, Nature 405, 681-685, 2000

[2] Geim A.K., Dubonos S.V., Grigorieva I.V., Novoselov K.S., Zhukov A.A. and Shapoval S.Y., “ Microfabricated adhesive mimicking gecko foot-hair”, Nature Materials 2, 461-463, 2003

[3] Y.Sekiguchi, P.Hemthavy, S.Saito, K.Takahashi, “ Adhesion between side surface of an elastic beam and flat surface of a rigid body ”, Journal of Adhesion Science and Technology, 10 August 2012

[4] Takehiko Yazaki, Yu Sekiguchi, Pasomphone Hemthavy, Kunio Takahashi, “ Effect of Shape and Distribution of Material Properties of Beam on Adhesion with Rigid Body Surface ”, 19th Symposium on ”Microjoining and Assembly Technology in Electronics”, Mate2013 pp.297-300

[5] ヘムタビーパソムポーン, 高橋邦夫, ” 生物の把持および脱離機構の解明と可逆接合への応用”, 溶接学会誌 vol.3,no3,2009,p195-200

EXPRIMENTAL STUDY ON DETERIORATION OF PAINT-COATED STEEL WITH DIFECT APPLIED CATHODIC PROTECTION IN TIDAL ZONE

Student Number: 10-11550 Name: Kyohei Shimura Supervisor: Nobuaki Otsuki

1 Introduction

Steel is used for marine structures. However steel is easy to corrode in marine environment, therefore various protection methods are developed. Above all, paint coating and cathodic protection are common methods and often used together.

Cathodic protection can stop corrosion reaction under water zone. However, when cathodic protection is applied to paint-coated steel with defect, cathodic protection leads to degradation of paint coating around defect. Paint coating is blistered or ripped off by the generation and accumulation of hydroxide ions induced by cathodic protection.

In tidal zone, there is a period in which paint-coated steel is exposed in air. At that time cathodic protection cannot work. So paint degradation in tidal zone may lead to corrosion.

In the literature review, there are few research which focused on influential factors on deterioration of paint-coated steel with defect applied cathodic protection and deterioration of paint-coated steel with defect applied cathodic protection in tidal zone. Therefore there are few proposal of paint-condition which is suitable for paint-coated steel applied cathodic protection in tidal zone.

From the above background, the objectives of this study are as following:

(1) To clarify the influence of paint type, solution, paint thickness, current density, defect on paint degradation speed.

(2)To clarify deterioration of paint-coated steel with defect applied cathodic protection in tidal zone.

(3)To select suitable paint-conditions for paint-coated steel applied cathodic protection in tidal zone.

2 Experiment procedures

2.1 Materials

The materials used in this study were steel (SS400), two types of paint (TarEpoxy, PhthalicResin) and two types of solutions (3wt%salt water, sea water). Properties of each paint are shown in **Table.1**. TarEpoxy paint has lower oxygen permeability, higher indentation elastic modulus and stronger adhesion than PhthalicResin.

Table.1 Properties of each paint

	TarEpoxy	PhthalicResin
Oxygen permeability [mol /cm^2・sec]	1.32E-13	3.26E-13
Indentation Elastic Modulus [N/mm^2]	1574	1425
Adhesion [kgf/cm^2]	over20	14.1

2.2 Specimen

In this study, steel plates (thickness: 3.2mm, width: 125mm) are provided as shown in **Fig. 1 (a)**. Lead wire is attached on the backside of each steel plate by soldering as shown in **Fig. 1 (b)**. Steel plate was embedded in epoxy resin as shown in **Fig. 1 (c)**. After painting, φ8mm defect was added as shown in **Fig. 1 (d)**.

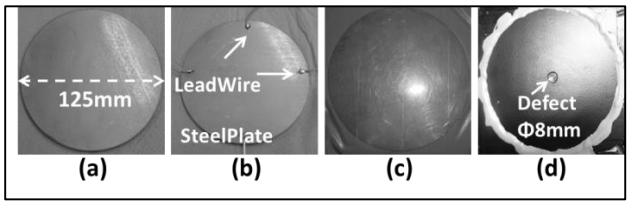

Fig. 1 Outline of specimens

2.3 Measurement items and method

In this study, appearance observation was conducted to understand duration until blistering on paint coating.

Polarization resistance was measured by alternating current impedance method. From bode plot as shown in **Fig. 2**, polarization resistance were measured.

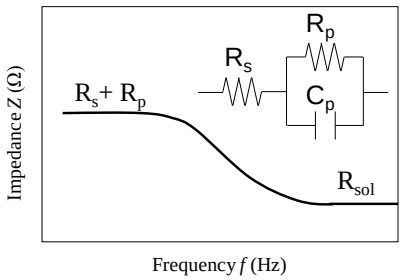

Fig. 2 Bode plot

3 Experimental results

3.1 Solution exposure test

This experiment was conducted to examine the influence of paint type, solution, paint thickness, current density and defect on paint degradation speed. Specimens are exposed in 20℃, 3wt% salt water or sea water.

The influence of paint type and solution are as shown in **Fig.3** and **Fig.4** (TE=TarEpoxy, PR= PhthalicResin/ SALT=3wt%salt water, SEA=sea water/ all specimens are with defect/ Paint thickness=300μm). From these figures, regarding paint type, TarEpoxy paint has more durability against cathodic protection. Regarding solution, polarization resistance become higher and duration until blistering become longer in seawater because of electrodeposition.

The influence of paint thickness and current density are as shown in **Fig.5** (Paint type=TarEpoxy/ all

spesimens are with defect/ Solution=3wt%salt water). From this figure, relation between paint thickness and duration until blistering is linear and difference of current density hardly influences on duration until blistering.

The influence of defect are as shown in **Fig.6** (D=with defect, ND=without defect/ Paint thickness of PR=300μm, TE=150μm/ Solution= 3wt%salt water). From this figure, defect shortens duration until blistering drastically.

3.2 Wet/dry cycle test

This experiment was conducted to examine deterioration of paint-coated steel with defect applied cathodic protection in tidal zone.

Specimens were exposed to wet/dry cycle environment which is simulating tidal zone. 1cycle consisted of 6hours 20℃ artificial sea water exposure and 6hours 20℃ air exposure.

The influence of paint type and cathodic protection on polarization resistance in tidal zone are as shown in **Fig.7** (Applied or Not Applied means whether cathodic protection is applied or not/ all specimen are with defect/ Paint thickness=150μm). From this figure, durability against cathodic protection is different in each paint type. As for TarEpoxy paint polarization resistance increases applying cathodic protection because of electrodeposition and. no paint degradation. As for PhthalicResin paint, though electrodeposition generates on steel surface, polarization resistance decreases applying cathodic protection because of severe paint degradation shown as **Fig.8**.

4 Conclusions

In tidai zone, using suitable paint, polarization resistance of paint-coated steel with defect increases applying cathodic protection because of electrodeposition and no paint degradation.

(1) TarEpoxy paint has more durability against cathodic protection than PhthalicResin paint. Regarding solution, polarization resistance becomes higher and duration until blistering becomes longer in seawater because of electrodeposition. Relation between paint thickness and duration until blistering of paint-coated steel with defect is linear. Difference of current density hardly influences on duration until blistering of paint-coated steel with defect. Defect shortens duration until blistering drastically.

(2) In tidal zone, durability against cathodic protection is different in each paint type. As for TarEpoxy paint polarization resistance increases applying cathodic protection because of electrodeposition and. no paint degradation. As for PhthalicResin paint, though electrodeposition generates on steel surface, polarization resistance decreases applying cathodic protection because of severe paint degradation.

(3) After seeing properties of each paint (**Table.1**) and the results of solution exposure test and wet/dry cycle test, suitable paint-conditions are selected as below :

・Using paint which has lower oxygen permeability, higher indentation elastic modulus and stronger adhesion.

・Increasing paint thickness as much as possible.

References

1) Masayuki Itagaki：AC impedance method principle・measurement・analysis (2008)

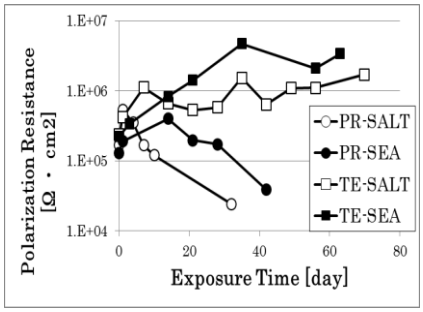

Fig.3 The influence of paint type and solution on polarization resistance

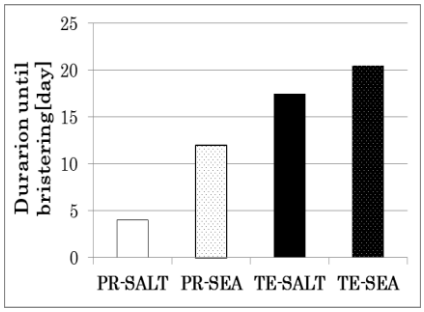

Fig.4 The influence of paint type and solution on duration until blistering

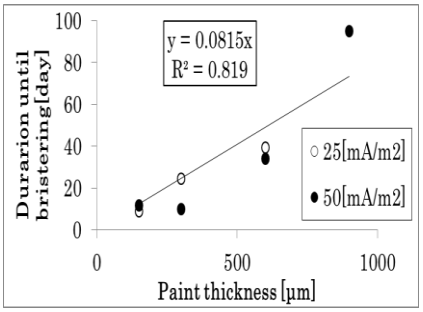

Fig.5 Relation between paint thickness and duration until blistering

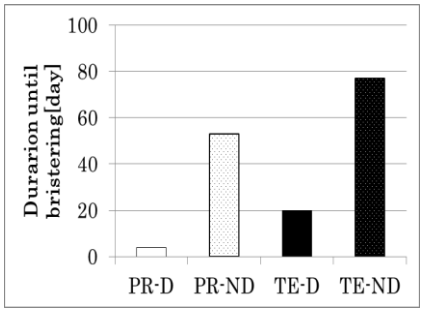

Fig.6 The influence of defect on duration until blistering

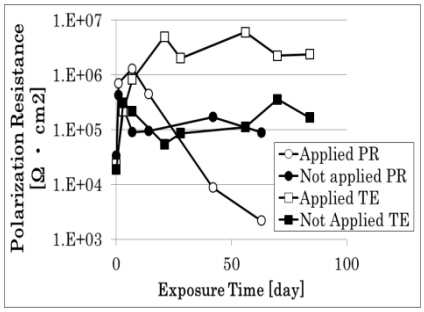

Fig.7 The influence of paint type and cathodic protection on polarization resistance in tidal zone

Fig.8 Picture of Applied PR 63rd day

Effects of free fatty acid removal on biodiesel fuel production from used frying rapeseed-soybean oil

Student Number: 10B12991 Name: Zhenqiang SHI Supervisor: Ryuichi EGASHIRA, Hiroaki HABAKI

1. Introduction

Biodiesel fuel, an alternative diesel fuel, is made from renewable biological sources such as vegetable oils and animal fats. Moreover, biodiesel fuel production itself also shows good effects in carbon neutral. Nonetheless, biodiesel fuel commercialization has not been promoted sufficiently due to its high cost of production and limitation on feed supply. The cost of feed oil frequently shares 80 % of biodiesel fuel production cost, so a reasonable feed oil and improving biodiesel fuel yield are significant to reduction in the production cost. The used frying oil has attracted many attentions due to its lower price and environmentally friend resource for biodiesel fuel production. The used frying oil occasionally contains free fatty acid by higher level, and the treatment of the used frying oil to remove free fatty acid has been studied[5-6].

This study aimed to examine the effects of deacidification methods in the feed pretreatment on the yields of treated oil and biodiesel.

2. Experimental

2.1 Feed Materials

Fresh frying oil, FFO, which was commercially available and consisted of rapeseed oil, soybean oil and a trace amount of silicone (less than 0.005wt%), and the used frying oil, UFO, derived from the above FFO were used as feed oils. Compositions of both feed oils, and some chemical properties like Acidity Value and Iodine Value were measured. Although both oils originally contained FFA, oleic acid (C18:1) and linoleic acid (C18:2) were added to the UFO to study the effect of FFA contant, $x_{FFA,0}$, in the UFO. The Wijs method was used for measuring of Iodine Value[7].

2.2 Feed Pretreatment

The experimental conditions of deacidification, DA, methods are summarized in **Table 1**. Filtration was carried out for removing the solid contents in UFO before DA. The DA and drying were conducted for the feed oils as the pretreatment before transesterification. Two types of DA methods were employed, such as esterification of FFA into FAME by methanol and sulfuric acid, EDA, and neutralization of FFA to soap by sodium hydroxide, NDA, as shown in the following reactions, respectively.

$$RCOOH + CH_3OH \rightleftharpoons RCOOCH_3 + H_2O \quad (1)$$

$$RCOOH + NaOH \rightleftharpoons RCOONa + H_2O \quad (2)$$

The reaction of EDA was carried out in a two-necked flask, which was equipped with reflux condenser, and temperature-controlled water bath. Liquids in the reactor were well mixed by a magnetic stirrer during the reactions. After EDA, sulfuric acid and methanol were removed by washing and drying. In the case of NDA, the reaction was carried out in flask with a magnetic stirrer, and the soap was removed by centrifuge. The pretreated oils were dried by heating. The procedures of DA and drying were cited from the previous works[1-4].

2.3 Transesterification

The experimental conditions in transesterification are summarized in **Table 2**. Methanol and sodium hydroxide were used as alcohol source and alkali catalyst to obtain FAME, as shown in the following equation.

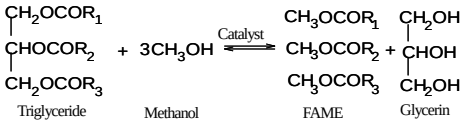

(3)

The equipment used in transesterification was the same as that used in EDA. Oil and glycerol phases were separated into each other after transesterification. Compositions of fatty acid methyl ester, FAME, in the oil phase, were determined by analysis using a gas chromatograph (GC-14B, Shimadzu CO. Ltd).

Table 1. Experimental conditions in DA

Deacidification by esterification	
MeOH/oil molar ratio [-]	7.5
H_2SO_4/oil mass ratio as catalyst [-]	0.03
Reaction temperature [K]	333
Reaction time [h]	1.5
Deacidification by neutralization	
NaOH/FFA molar ratio [-]	1.15
Reaction temperature [K]	353
Reaction time [h]	0.083

Table 2. Experimental conditions in transesterification

MeOH/oil molar ratio [-]	6
NaOH/oil mass ratio as catalyst [-]	0.01
Reaction temperature [K]	333
Reaction time [h]	1

3. Results and Discussion

3.1 Compositions of feed oils

The compositions of the feed oils are summarized in **Table 3**. The used feed oils consisted mainly of oleic acid, linoleic acid and palmitic acid. The FFO contained a trace amount of FFA, and $x_{FFA,0}$ in the original UFO was 0.017. Iodine values of FFO and UFO were 119.46 and 95.4 g/100g-oil, respectively, namely, the average number of double bonds in a molecule contained in UFO was smaller.

Table 3. Compositions of feed oils

	Mass fraction	
	FFO	**UFO**
Oleic acid (C18:1)	0.22	0.21
Linoleic acid (C18:2)	0.53	0.47
Palmitic acid (C16:0)	0.12	0.12
α- linolenic acid (C18:3)	0.077	0.066
FFA	0.00069	0.017~0.23

3.2 Effects of DA method in feed pretreatment

The effects of DA method on the mass fraction of FFA in the pretreated oil, $x_{FFA,FP}$ are shown in **Figure 1.** The $x_{FFA,FP}$ could be reduced to under 0.02 in the cases of both NDA and EDA, but $x_{FFA,FP}$ was higher in NDA than that in EDA when $x_{FFA,0}$ >0.05.

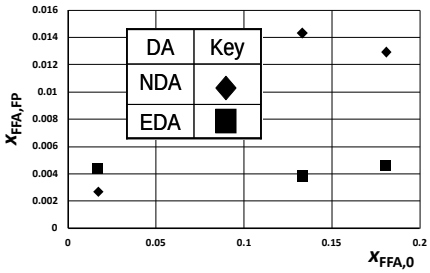

Fig.1 Effects of DA method on $x_{FFA,FP}$ in UFO

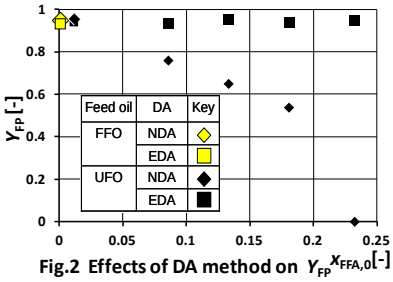

Fig.2 Effects of DA method on Y_{FP} $x_{FFA,0}$[-]

The yield in the pretreatment, Y_{FP}, was defined as following:

$$Y_{FP} = \frac{\text{Mass of pretreated oil}}{\text{Mass of feed oil}}$$

Figure 2 shows the effects of DA methods on Y_{FP}. In the case of EDA, Y_{FP} was high, more than 0.9, irrespective to $x_{FFA,0}$, because FFA could be converted to FAME and recovered in the oil phase. In the case of NDA, Y_{FP} decreased steeply with $x_{FFA,0}$ due to the removal of FFA as soap. When $x_{FFA,0}$ >0.1, the loss of feed oil was much larger than the amount of FFA in the feed oil. The neutralization of FFA should generate moisture content to enhance the saponification of the feed oil. The Y_{FP}s by NDA were the same as by EDA when $x_{FFA,0}$<0.02. In the range of $x_{FFA,0}$>0.2, the NDA treatment was impossible, because the liquid system became stable emulsion with the soap produced from the neutralization of FFA.

3.3 Effects of DA method in transesterification

The yield in transesterification, Y_{TE}, and FAME yield, Y_{OA}, are defined as followings:

$$Y_{TE} = \frac{\text{Mass of FAME}}{\text{Mass of pretreated oil}}, \quad Y_{OA} = Y_{FP} \times Y_{TE}$$

Figure 3 shows the effects of DA method on the yield of FAME at the transesterification. The operation of transesterification was impossible without DA in the range of $x_{FFA,0}$<0.1 because of emulsification of the whole liquid system. Even if $x_{FFA,0}$=0.01, the effects of saponification was serious and Y_{TE} decreased to around 0.5. With the pretreated feed oils, Y_{TE} was almost constant at around 0.94. The effects of the iodine number of the feed oil on Y_{TE} were unclear. The effects of $x_{FFA,FP}$ on Y_{TE} are shown in **Figure 4**. When the mass fraction of FFA i was more than 0.015, Y_{TE} decreased sharply from around 0.94 to 0 because the operation was impossible.

Figure 5 shows the effects of $x_{FFA,0}$ on the overall yield of FAME relative to feed oil, Y_{OA}. In the case of EDA, Y_{OA} was always more than 0.8 irrelative to $x_{FFA,0}$. In any case, Y_{OA} was the same as each other when $x_{FFA,0}$<0.02, and Y_{OA} decreased as $x_{FFA,0}$ increased in the case of NDA mainly due to the yield reduction at the DA treatment.

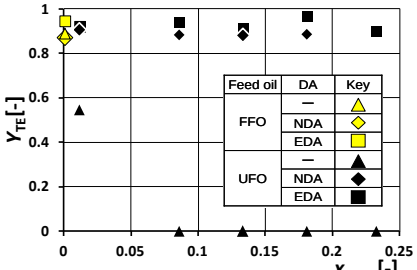

Fig.3 Effects of DA method on Y_{TE} $x_{FFA,0}$[-]

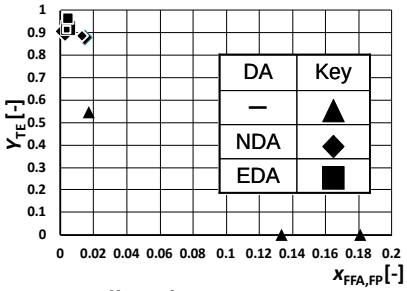

Fig.4 Effects of $x_{FFA,FP}$ on Y_{TE} in UFO

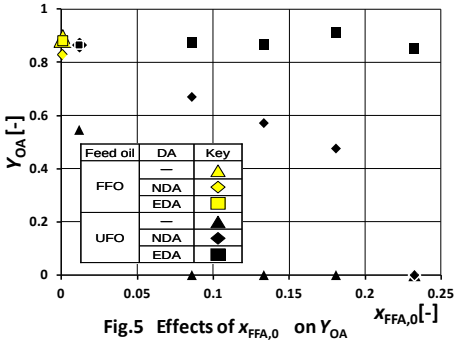

Fig.5 Effects of $x_{FFA,0}$ on Y_{OA}

4. Conclusion

Deacidification was necessary for used frying oil, and deacidification by acid catalyst attainted a higher fractional yield of oil in feed pretreatment than that by alkali, which can't be carried out when mass fraction of free fatty acid in feed oil was higher than 0.2 . Similar yield of fatty acid methyl esters were obtained in transesterification after different deacidification method.

Nomenclature

$x_{FFA,0}$: mass fraction of free fatty acid in feed oil [–]

$x_{FFA,FP}$: mass fraction of free fatty acid in pretreated oil[–]

Y_{FP} : yield in pretreatment [–]

Y_{TE} : yield in transesterification [–]

Literature Cited

[1] Hayashi Tomoki "Effects of Operating Conditions in Biodiesel Fuel Production from Low-valued Feed" Bachelor Thesis, Tokyo Tech (2008)

[2] Sinthupinyo Patima "Comparative Study of Biodiesel Production by Alkaline Transesterification from Low- valued Feed" Master Thesis, Tokyo Tech (2007)

[3] Sinthupinyo P. et al.;SCEJ Hamamatsu, R207 (2008)

[4] Sinthupinyo P. et al.; JCEJ, 43, (2), 214~223(February, 2010)

[5]Y.Wang, S.Ou, et al.; J. Mol. Catal. Chemical 252(2006)107-112

[6] Mustafa Canakci. "The potential of restaurant waste lipids as biodiesel feedstocks" Bioresource Technology, 98(2007)183-190

[7] DIN 53241-1:1995, "Determination of iodine value by methods using Wijs solution (FOREIGN STANDARD)"

International comparison on the performance of freight railway in developing countries

Student Number: 10B13246 Name: Masashi Sota Supervisor: Shinya Hanaoka

1. Introduction

It is estimated that the amount of Greenhouse Gas (GHG) emission by transportation sector in 2050 will be double of one in 2010 (DFID) and be largely occupied by road transportation. The modal shift from freight transportation by road to one by low carbon emission mode such as railway and inter-water transportation is necessary for reducing the amount of GHG emission especially in developing countries because these countries heavily depend on the road transportation. In case of transportation by railway, the amount of GHG emission per ton-km is about one tenth of the one by road transportation. In addition, in terms of cost, the railway has advantage and low cost for freight transportation enables country to flourish.

However, so far, only a few countries with large land and tremendous mining resources such as U.S.A, Russia, China have been successful with the freight transportation by railway. On the other hand, modal share of freight transportation by railway in most other countries is about 20% at most.

The objectives of this research are the following: (1) To examine the current performance and condition of freight transportation by railway in each region such as Sub-Saharan Africa, South Asia, Middle East and North Africa, Latin America and the Caribbean, East Asia and Pacific, East Europe and Central Asia (2) To identify the causes and factors which make the performance of the freight transportation by railway better or worse.

2. Methodology

The Data Envelopment Analysis (DEA) is adapted for assessment of the performance of freight transportation by railway. DEA is the method for measuring the productive efficiency of the Decision Making Units (DMU) based on the DMU with best performance. The efficiency of each DMU is the ratio of the sum of weighted outputs to the sum of weighted inputs. The value of efficiency varies from 0 to 1. If it is 1, the DMU is efficient. The efficiency of DMU_k is calculated as following equations:

$$\max \theta_k = \frac{\sum_{j=1}^{s} u_j y_{jk}}{\sum_{i=1}^{m} v_i x_{ik}} \quad (1)$$

Subject to

$$\frac{\sum_{j=1}^{s} u_j y_{jk}}{\sum_{i=1}^{m} v_i x_{ik}} < 1 \ (k = 1,2,....,n) \quad (2)$$

$$v_1, v_2, ..., v_m \geq 0 \quad (3)$$

$$u_1, u_2, ..., u_s \geq 0 \quad (4)$$

Input is referred to as u_j ($j=1,..,s$) and output is referred to v_i ($i = 1,..,m$). In this study, 3 inputs, railroad quality, network length (km), and number of rolling stocks, and one output, Freight ton-km (million), are selected. The railroad quality is cited from World Economic Forum. This value is sought by asking the executives in each country to rate infrastructure quality of railway and taking the average of these scores.

The productive efficiency of freight transportation by each country is calculated by Constant Return to Scale model (CRS) and Variable Return to Scale model (VRS) to consider the effect caused by scale. In addition, the output- oriented model is used for evaluation of CRS and VRS efficiency because the idea was to analyze the possibility of increasing the outputs while keeping the current level of the input.[1]

The results of DEA and the extent of the contribution of the mining resources to each country's economy are combined in order to identify which country has been successful in freight transportation by railway without mining resources or which country has failed in freight transportation in spite of rich resources. The Mining Contribution Index (MCI) is used for indicating the degree of effect of mining resources to economy in each country. The efficient or inefficient countries are selected and further analysis is conducted for these countries by considering the factors excluded in DEA. Through the further analysis, the research defines the reasons and factors which lead to the efficient performance or inefficient performance.

3. Results

3.1. The characteristics of each region

In Sub Saharan Africa, all countries except South Africa have low traffic. Almost all infrastructure and rolling stocks are old and non-functional. Because of insufficient fund from the government, the railway service has been privatized recently. As a result, 70% of rail networks have been fully or partially privatized. However, only a few privatizations have been successful due to the failure of demand estimation for freight transportation.

In South Asia, all railway networks are operated and owned by the government. India is the only country which has succeeded in railway transportation. There is a tendency to invest in infrastructure and focus on the market demand because of future demand for freight transportation caused by growth of economy. Compared with other nations, the ratio of the passenger volume is quite high because of low fare regulated by the government policy.

In Middle East and North Africa, there is little private participation though the governments have tried to induce private participation. The countries in this region give exclusive transportation service, only for freight or only for passenger.

In Latin America and the Caribbean, almost all countries induce the privatization positively, including some cross-border ownership. These concessions were completed by 2000. The freight transportation by railway in this region has been increased by more than 80% over the decades. However, the quality of infrastructure is relatively low compared to other regions since most networks were constructed by

suzerain about 100 years ago.

In East Asia and Pacific, the railway network is mainly operated by the government. This region has also problem in infrastructure quality. In addition, the connectivity among adjacent countries is not efficient due to political reasons. Few mining resources lead to the lack of the demand for freight transportation by railway.

In Eastern Europe and Central Asia, though the governments in this region have started to accept the private participation, only a few cases can be found. They have tried to join EU by following their regulations which force to induce vertical separation, enhancement of quality of infrastructure and improve financial condition. As a result, significant staff reduction occurred in nearly all countries.

3.2 The results of DEA

The result of DEA is described in Table1 and 2. The efficient country group is clarified into two groups based on the results of CRS model and VRS model. The countries whose efficiency is 1 only in VRS model are efficient in spite of small scale which means value of all inputs and outputs are small (Table1).

The criteria for selecting the inefficient countries is VRS<0.10 and Scale efficiency, the value of CRS/VRS, is greater than 0.80. This means that efficiency is quite low although the scale of the input of the country is large to some extent. In addition, factors causing bad performance can be identified in the calculation process of DEA (Table2). The countries selected are the following:

Table1. Efficient country

Criteria	Country
CRS=1 and VRS=1	Kazakhstan, Brazil, Colombia, India, Latvia
only VRS=1	Uganda, Albania, Jordan

Table2. Inefficient country

Factor	Country
railroad quality	Kenya, Armenia, Algeria, Bangladesh, Pakistan
network length	Nigeria, Sri Lanka
rolling stock	Moldova

The figure 1 shows the scatter plot between the efficiency which is calculated by VRS model and Mining Contribution Index.

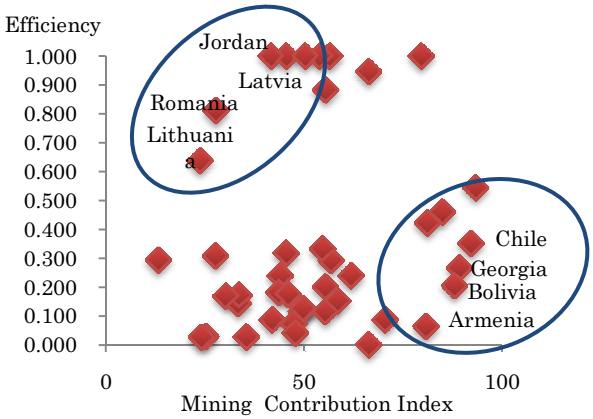

Fig.1 Scatter plot between the efficiency and MCI

Countries inside the circle in upper side have good performance in spite of low mining contribution. On the other hand, the countries in the other circle have failed in the operation of freight transportation by railway and have lost the opportunity for delivering the mining resources. These countries are also selected as candidates for case study.

3.3 Further analysis

The selection of countries for further analysis is conducted by the criteria as mentioned and reflecting the data availability for further research. From the further analysis, the following results are obtained

3.3.1 Inefficient country

There are mainly two reasons why performance of the transportation by railway is insufficient. First, lack of ability for maintenance of infrastructure is serious trigger for inefficient performance. The railway network was constructed by suzerain for delivering the mining resources to the port. However, the network is too large for them to maintain infrastructure quality without suzerain's support after independence.

The other reason is biased government policy for road transportation. The government spends more funds for road transportation and deregulates the rule related with road transportation, which leads to unfair competition environment between rail transportation and road transportation. As a result, revenue from freight transportation and fund from government decrease and this leads to the lack of finance to maintain and rehabilitate the infrastructure and induce continuous decrease of infrastructure quality.

3.3.2 Efficient country

They lost modal share of freight transportation by railway once because of emergence of road transportation. However, they have recovered it with measures such as privatization of the railway operation, tremendous investment for enhancing the quality of infrastructure and enhancement in the quality of port for inducing the export from the landlocked countries. As tendency for these countries, they have increased the transportation of container cargos by improving quality of facilities such as inland port and container terminal.

4. Conclusion

This research figures out the current condition and performance of freight transportation by railway in developing countries. This study also discloses the reasons why some countries have been successful in freight transportation by railway and others have failed in it.

Sufficient demand for transportation of bulk materials plays an important role for ensuring enough revenue to maintain the quality of infrastructure. Low developing countries need to focus on the lines with heavy freight traffic. Otherwise, they may result in ruining the whole network due to fund shortage and deficiency of ability for maintenance.

Furthermore, the policy of governments after independence from suzerain heavily affects the current performance of freight railway. This different policy leads to increase or decrease the importance of freight railway in each country.

References

[1] W.LAN, T.I LIN, Technical efficiency and service effectiveness for railways industry: DEA approaches, Journal of the Eastern Asia Society for Transportation Studies, Vol.5, pp2932-2947, 2003.

Removal of Trivalent Chromium by Artificial Zeolite from Lake Sludge

Student number: 10_13832 Name: Takahiro Takamatsu Supervisor: Hirofumi HINODE and Winarto Kurniawan

1. Introduction

Water is a necessity to human life. The water that we use are sometimes sourced from nearby lakes. However, pollutants and nutrient salts are easily accumulated in the lakes because of its nature as a closed system, and sometimes also as the receiving body of domestic wastewater.

Lake dredging is one of the most effective methods used to remove pollutants accumulated as lake sludge. However, the dredged sludge will be ultimately disposed in landfills and may give rise to soft ground. A preferable method of disposal is to utilize these dredged lake sludge for other possible applications such as water treatment.

According to previous study, lake sludge which contains silica and alumina can be used as raw material to synthesize zeolites by hydrothermal treatment [1]. Zeolites have cation exchange capacity, and adsorption capacity that can be used for removal of heavy metal ion such as chromium (III). Chromium (III) is a common waste product from tannery and several processes from the steel industry, and it causes adverse effect to the environment. In this study, zeolites were synthesized from dredged lake sludge and were evaluated for its ability to remove Cr (III) ions from model wastewater.

2. Experimental

2.1. Zeolite Synthesis

In this study, sludge from Kasumigaura lake in Ibaraki prefecture was used as raw material. The Si/Al ratio of the sludge was adjusted to desired value by addition of Na_2SiO_3 solution. For zeolite synthesis, 1.6 g of lake sludge was treated in 8 mL of alkali solution with different concentrations (1, 2, and 4 M). Afterwards, the samples were placed in the oven at 90°C, 120°C, and 150°C for hydrothermal synthesis. The prepared zeolites have final Si/Al ratios of 1.2, 1.5, 1.9, 2.5, and 3.0. The prepared catalysts were then characterized using Scanning Electron Microscopy (SEM) and X-ray Diffraction (XRD).

2.2 Measurement of Cation Exchange Capacity (CEC)

CEC of synthesized zeolites was measured by putting zeolite samples into NaOAc solution and placed in a shaker to facilitate Na^+ adsorption. After shaking, the samples were centrifuged to separate it from NaOAc solution. The samples were then put into NH_4OAc solution to exchange Na^+ ions with NH_4^+ions, followed by centrifugation to separate it from NaOAc solution. Afterwards, Na^+ ions exchanged in the separated solution was measured using Inductively-Coupled Plasma Atomic Emission Spectroscopy (ICP-AES) to determine samples' CEC.

2.3. Cr (III) Ion Removal

For Cr (III) ion removal experiment, zeolite (0.1 g) was put into chromium (III) nitrate solution (100 ppm, 50 mL) and put into the shaker for 20 h. Cr(III) concentration of the solution was determined using ICP-AES. The table below (Table 1) shows the speciation of trivalent chromate cations. The speciation depends on the solution pH, therefore pH of solution was varied in order to observe this effect on the removal performance. Because there is a possibility of precipitation when the pH of solution is over 5.0, pH of 3.0 and 4.5 were selected.

Table 1. Distribution of the chromium species as a function of solution pH.

pH	Dominant
＜4.0	Cr^{3+}
4.0 - 5.7	$Cr(OH)^{2+}$
＞5.7	$Cr(OH)_2^+$

3. Results and Discussion

3.1 XRD Analysis

From XRD analysis of the zeolites synthesized at different alkali concentrations, temperatures, and Si/Al ratios, different synthesis conditions produced different phases that are shown in Table 2. XRD results show that the samples contains various crystal phases in the zeolites such as sodium aluminum silicate hydrate, Na-P1, and analcime-C.

Table 2. CEC values of products obtained from various alkali concentrations, temperatures, and Si/Al ratios

Zeolite Preparation Conditions/Parameter		CEC value [meq / 100g]	Phase
Si / Al Ratio [mol / mol] (120°C, 2 M NaOH)	1.2	198	S, Q
	1.5	221	P, A
	1.9	264	P, A
	2.5	287	P, A
	3.0	186	P, A
Temperature (Si / Al = 2.5 2M NaOH)	90°C	269	P, Q
	120°C	287	P, A
	150°C	144	A
NaOH concentration (Si / Al = 2.5, 120°C)	1 M	195	P, A
	2 M	287	P, A
	4 M	177	P, S

S = Sodium aluminum silicate hydrate

Q = Quartz ; P = Na-P1 ; A = Analcime-C

3.2 Cation Exchange Capacity of Samples

Table 2 also shows the CEC values of prepared zeolites. The highest CEC value was 287 meq/100 g which was shown by zeolite synthesized with the condition of 2 M NaOH, 120 °C, and Si/Al=2.5.

3.3 SEM Images of Zeolite Samples

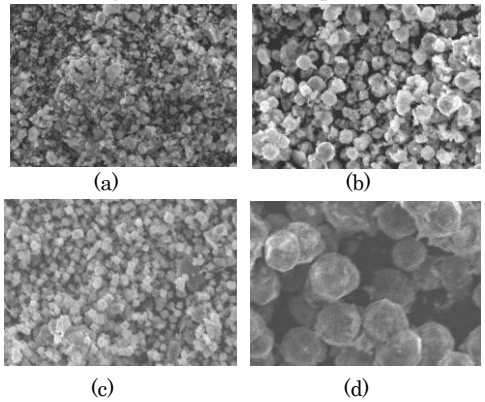

Fig. 1. SEM Images of zeolites synthesized under different conditions (a) Si/Al = 1.2, T=120°C, 2 M NaOH, (b) Si/Al = 2.5, T=120°C, 2 M NaOH, (c) T = 90°C, Si/Al = 2.5, 2 M NaOH,(d) = 150°C, Si/Al=2.5, 2 M NaOH

Some of the prepared zeolites' SEM images taken at 2000 times magnification are shown in Fig. 1. These are the samples that showed the highest CEC values, according to Table 2.

Table 3. Cr (III) ion removal by prepared zeolites

Zeolite Preparation Conditions	CEC Value [meq/ 100g]	Removal Amount [mg-Cr/g]		Phase
		pH = 4.5	pH = 3.0	
Si / Al = 1.2, 120°C, 2 M NaOH	198	26.2	7.6	S, Q
Si / Al = 2.5, 120°C, 2 M NaOH	287	9.5	10.7	P, A
T = 90°C Si / Al = 2.5 2M NaOH	269	10.2	9.9	P, A
T = 150°C Si / Al = 2.5 2M NaOH	144	6.3	5.1	A
NaOH Conc. = 4 M Si / Al = 2.5, 120°C	177	45.4	11.3	P, S

S = Sodium aluminum silicate hydrate
Q = Quartz ; P = Na-P1 ; A = Analcime-C

Table 3 shows amount of Cr(III) removal by synthesized zeolites (experiment pH = 4.5 and 3.0). The highest value was showed by zeolite synthesized with the condition of 4 M NaOH, 120°C, and Si/Al=2.5, (pH = 4.5). The second highest value was shown by zeolite synthesized with the condition of 2 M NaOH, 120°C, and Si/Al=1.2, (pH = 4.5). The removal amount of other synthesized zeolites were relatively lower.

It can be observed that both zeolites that showed high Cr (III) removal values have sodium aluminum silicate hydrate, therefore, it can be considered that sodium aluminum silicate hydrate is a good for removal of Cr(III) at pH = 4.5.

According to Table 3, zeolite synthesized with the condition of 4 M NaOH, 120°C, and Si/Al=2.5, had low CEC, however it showed higher removal value of Cr (III) than zeolite synthesized with the condition of 120°C, 2 M NaOH, and Si/Al=2.5 which had the highest CEC. Because the later zeolite which showed a low Cr (III) removal consists mainly of Na-P1 and analcime-C, this result supports the conclusion that sodium aluminum silicate hydrate was the phase that contributes to Cr (III) removal.

Langmuir adsorption isotherm for these zeolites (at pH = 4.5) is shown in Fig. 2. The maximum Cr (III) adsorption capacity of zeolite with the best removal value was 46.0 mg/g.

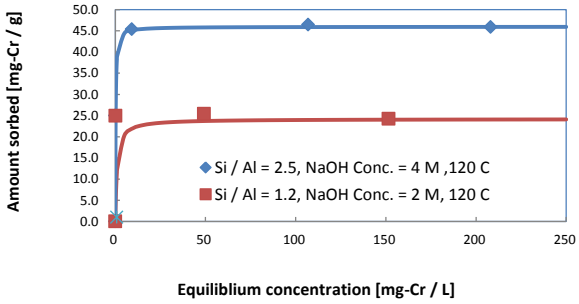

Fig. 2. Langmuir adsorption isotherm of Cr(Ⅲ) by representative zeolites at pH of 4.5 (±0.2).

4. Conclusions

The utilization of lake sludge as a raw material for zeolite synthesis was successfully done in this study. The type of zeolites that can be produced from lake sludge is dependent on alkali concentrations, temperatures, and Si/Al ratios of hydrothermal synthesis. Zeolite with a relative high Cr (III) removal was successfully synthesized from lake sludge by hydrothermal synthesis. The pH strongly influenced the Cr (III) removal by the zeolites.

Reference:

[1] Yan Shao, Synthesis of Zeolites from Lake Sludge, International Development Engineering, School of Science and Engineering, Tokyo Institute of Technology

[2] Deyi Wu , Yanming Sui , Shengbing He , Xinze Wang , Chunjie Li , Hainan Kong "Removal of trivalent chromium from aqueous solution by zeolite synthesized from coal fly ash" *Journal of Hazardous Materials*,(2008) , **155,** pp. 415 – 423

[3] Japan Association of Zeolite, Zeolite conference home page, http://www.jaz-online.org/, Retrieved in January 13, 2013

[4] Qingyu Guan, Deyi Wu, Yan Lin, Xuechu Chen, Xinze Wang, Chunjie Li, Shengbing He, Hainan Kong Application of "zeolitic material synthesized from thermally treated sediment to the removal of trivalent chromium from wastewater" *Journal of Hazardous Materials*, (2009) **155**, pp.244-249

伝搬チャネル応答とモーションの同時測定のためのモーションキャプチャソフトウェアの開発

学籍番号: 10B15417　名前: 陳　高超　指導教員: 高田　潤一・金　ミンソク

1　はじめに

無線ボディエリアネットワーク（WBAN）は人体周辺の通信ネットワークであり，医療サービスなどの分野で応用が期待されている．WBAN の要件としては，高信頼性かつ省電力のデータ通信が挙げられ，その実現に向けては伝搬路特性の評価が重要な基盤となる [1]. WBAN における伝搬路特性は，様々な要因（周囲環境，人体，動作，アンテナ）に影響され，それらの複合的な現象として観測される．そのため，実験により測定された伝搬路特性から各要因の影響を分離することが現実的にできない．一方で，シミュレーションでは，すべての要因を含めることはできないが，限られた各要因を分離して伝搬路特性を評価することができる．

そこで，伝搬路特性における各要因の依存性を体系的に解析するために，シミュレーションと伝搬測定の両方を用いる手法の開発を目指す．図 1 には本手法の全体像を示す．まず，歩行などといった特定の動作において，伝搬測定と人体動作の測定を同時に行う．伝搬測定では，送受信アンテナを人体に取り付け，Vector Network Analyzer (VNA) を用いることで送受信アンテナ間の伝搬路特性を取得する．人体動作の測定では，安価なゲーム用モーションキャプチャデバイスである Kinect を用いる．取得された人体動作データを元に，シミュレーション用の人体モデル（アバタ）を生成し，電磁界の数値計算手法を適用することで，伝搬路特性をシミュレーションする．そして，シミュレーションおよび伝搬測定で得られた伝搬路特性を比較・検討する．このような手法の実現に向けて，本研究では伝搬路特性と人体動作の同時測定システムの構築を行う．具体的には，VNA と Kinect の同期方法と Kinect から得られるデータをもとしたアバタ生成方法を検討する．

2　同期測定システム

Kinect は人体における 20ヶ所の関節の 3 次元座標を 1 秒間あたり 30 回取得できる [2]．また，関節座標データを取得すると同時に，現在時間をオペレーティングシステムに問い合わせることで，その動作フレームの時刻情報とすることができる．しかし，実際には入出力等のオーバーヘッドにより，秒間 12 回ほどしか記録できない．すなわち，サンプリング時間が一定ではない．一方，VNA のサンプリング時間は一定であるとみなせるが，VNA は測定開始時刻を記録する機能を持っていない．すなわち，時刻をもとにした同期が不可能である．そこで，本システムでは，人体動作をもとにした時刻同期を行う．人体のアンテナが取り付ける箇所を急動作させると，その箇所の人体動作データと伝搬路特性両方が急変化する．二つの急変化する時刻を合わせることで，同期を行うことができる．

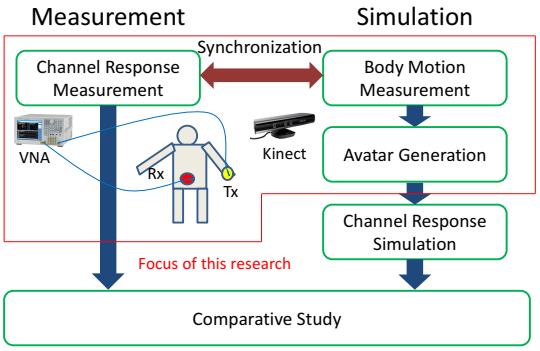

図 1: 伝搬路特性評価の概念

3　アバタ生成

Kinect から得られるデータは各関節の 3 次元座標のみであるため，そのままではシミュレーションに用いることができない．そこで，本研究では Kinect から得られた関節座標データをもとに BVH ファイル [3] を生成し，これを 3D グラフィックソフトウェアにインポートすることで，アバタを生成する．BVH ファイルは，モーションキャプチャ用のデータフォーマットで，人体のスケルトン情報とその動作情報から成る．スケルトン情報では，関節の接続構造が階層的な構造で表現されている．動作情報は関節の向きを表すオイラー角の時系列となっている．BVH ファイルの生成は，動作測定における負荷削減のため，オフラインで実行される．

4 実験

Kinect および VNA を制御するソフトウェアを C を用いて開発した [4]．Kinect の制御には Kinect for Windows SDK を利用した．また，BVH ファイルの生成を MATLAB を用いて実装した．

構築したシステムを検証するための実験を行った．送信アンテナは左手首，受信アンテナはへそに取り付けた．VNA の周波数は 445MHz, サンプリング数は 3001, サンプリングレートは 100 sample/sec とした．まず，静止状態を保ち，伝搬路特性と Kinect の安定を待った．次に手を急速に動かすことで，同期時期を作った．さらに，静止状態を保ち，伝搬路特性と Kinect の安定を待ったあと，歩行動作を開始した．

図 2 は測定した伝搬路特性と左手首の高さを，同期してプロットした結果である．0 秒は同期した時刻で，4 秒までは安定化のための静止状態，4 秒からは歩行時間である．伝搬路特性と左手首位置のトレンドが一致していること確認できる．これをより詳細に検証するために，この二つのサンプリング間隔を一致させてから，相互相関係数を計算した．図 3 に相互相関係数を示す．遅延が-0.049 秒のときに，ピーク値 0.5401 が示された．Kinect の平均的なサンプリング時間である 0.08 秒に比較すると遅延は十分に小さい．以上により，測定システムの同期性が証明された．

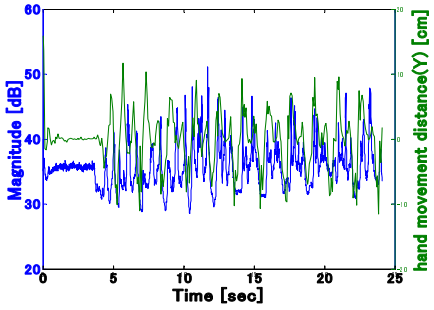

図 2: 同期測定テスト

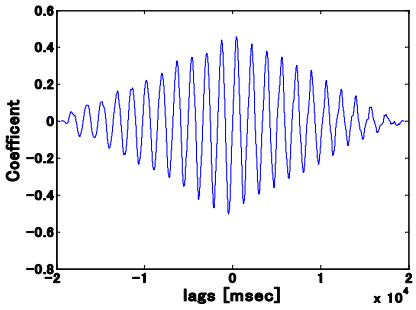

図 3: 相互相関

また，図 4 にはアバタ生成に関する結果を示す．図 4(a) は歩行動作中の 1 フレームにおいて，キャプチャ画像に関節座標データを重ねたものである．この関節座標データをもとに生成した BVH ファイルを，人体スケルトンとして表現したものを図 4(b) に示す．さらに，この BVH ファイルをもとに生成したアバタを図 4(c) に示す．図 4(a)-(c) において，人体動作がおおむね一致していることが確認できた．アニメーションでの再現も別途行い，歩行動作が再現できていることを確認した．

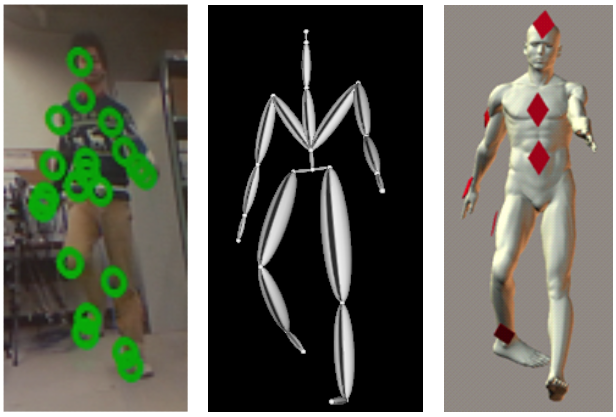

図 4: アバタの生成

5 結論

WBAN 伝搬路特性における様々な影響要因を分離して解析するために，シミュレーションと伝搬測定の両方を用いる手法の開発が必要である．これに向け，本研究では伝搬路特性と人体動作の同時測定システムを構築し，その検証を行った．具体的には，伝搬測定に用いる VNA と人体動作測定に用いる Kinect の同期方法として，人体動作を用いる手法を提案した．また，シミュレーションに用いるアバタの生成方法として，BVH ファイルの作成と 3D グラフィックソフトウェアの利用を提案した．今後の課題としては，関節座標データに含まれるノイズの除去が挙げられる．そして，様々な動作やアンテナの位置を変化させた場合の伝搬路特性を評価する予定である．

参考文献

[1] H. Cao, V. Leung, C. Chow, H. Chan, “Enabling Technologies for Wireless Body Area Networks: A Survey and Outlook,” *IEEE Commun. Mag.*, Vol. 4, pp.84-93, Dec, 2009

[2] Kinect for Windows Programming Guide page, Kinect for Windows Sensor Components and Specifications, http://msdn.microsoft.com/en-us/library/jj131033.aspx

[3] M. Meredith, S. Maddock, “Motion Capture File Formats Explained,” http://www.dcs.shef.ac.uk/intranet/research/public/resmes/CS-0111.pdf

[4] 中村 薫，斉藤 後太，宮城 英人,「KINECT for Windows SDK プログラミング C++編」，秀和システム

A STUDY ON IMAGE MATCHING USING GLOBAL PROJECTION TRANSFORMATION

Student Number:10-15446 Name:Yang Chen Supervisor:Yukihiko YAMASHITA

1 Introduction

Image matching refers to a process of matching plural images taken from the same scene with overlapping to find the correspondence between images. It is widely used in medicine, biology, information processing and other fields. It has been an indispensable technology for image recognition.

Image matching methods cover two categories:one is based on the gray, the other is feature. Normalized cross-correlation method based on the gray is commonly used for image matching. It has many good qualities, such as high accuracy, high adaptable, and strong anti-jamming. However, it has a problem that it is sensitive for the deformation of images. To this issue, the validity of a method using the Global Affine Transformation (GAT) correlation has been reported. In order to enhance the deformation resistance, I prorose extending affine transformation to projection transformation.

In this paper, I explain the process of the Global Projection Ttransformation (GPT) correlation method. I show the validity and property of the method.

2 Global Affine Transformation Correlation

2.1 Normalized Cross-Correlation

I denote the input gray-scale image as $f(\boldsymbol{x})$, and the target gray-scale image as $g(\boldsymbol{x})$. Here, I denote $\boldsymbol{K}$ and $\boldsymbol{x}$ as the domain of the image and a position vector defined in $\boldsymbol{K}$, respectively.

By using the definite canonicalization, I obtain the matching measure of normalized cross-correlation as follow:

$$C(f,g) = \int_{\boldsymbol{K}} f(\boldsymbol{x})g(\boldsymbol{x})d\boldsymbol{x}. \tag{1}$$

However, because the approach is a correlation type, it still has the problem that the correlation measure is sensitive to geometric image distortions such as an affine transformation.

2.2 Global Affine Transformation Correlation

The Global Affine Transformation (GAT) is a uniform affine transformation to an input image. Affine transformation of a point $\boldsymbol{x}$ to $\boldsymbol{x'}$ is expressed by

$$\boldsymbol{x'} = A\boldsymbol{x} + \boldsymbol{b}. \tag{2}$$

I denote the transformed image by $f'(\boldsymbol{x})$. The correlation value between the input image and the transformed image is given by

$$C(f',g) = \int_{\boldsymbol{K}} \frac{1}{|A|} f(A^{-1}(\boldsymbol{x}-\boldsymbol{b}))g(\boldsymbol{x})d\boldsymbol{x}. \tag{3}$$

Because A and $\boldsymbol{b}$ are directly in the variable of function f, it is difficult to determine A and $\boldsymbol{b}$. Therefore, I change the function to (4) by using the Gaussian window function.

$$C(f',g) = \iint_{\boldsymbol{K}} G(A\boldsymbol{x}_1 + \boldsymbol{b} - \boldsymbol{x}_2)f(\boldsymbol{x}_1)g(\boldsymbol{x}_2)d\boldsymbol{x}_1 d\boldsymbol{x}_2. \tag{4}$$

Here, A and $\boldsymbol{b}$ appear only in the Gaussian window function.

In order to achieve a higher process speed, I also introduce the edge direction function. Finally the correlation value formula is given by

$$C_{\mathrm{GAT}}(f,g) = \iint_{\boldsymbol{K}} G(A\boldsymbol{x}_1 + \boldsymbol{b} - \boldsymbol{x}_2) \\ \delta(\nabla f(\boldsymbol{x}_1), \nabla g(\boldsymbol{x}_2))f(\boldsymbol{x}_1)g(\boldsymbol{x}_2)d\boldsymbol{x}_1 d\boldsymbol{x}_2. \tag{5}$$

2.3 Linear Equations for Optimal GAT Determination

To calculate factor A and $\boldsymbol{b}$, I differentiate the objective function $C_{\mathrm{GAT}}(f,g)$ by A and $\boldsymbol{b}$. The necessary condition of maximization yields that both derivatives of $C_{\mathrm{GAT}}(f,g)$ with A and $\boldsymbol{b}$ equal to zero. Finally I get factor A and $\boldsymbol{b}$ as follows:

$$\begin{aligned} A &= (\overline{\boldsymbol{x}_2\boldsymbol{x}_1^T} - \frac{\overline{\boldsymbol{x}_2}\,\overline{\boldsymbol{x}_1}^T}{\overline{1}})(\overline{\boldsymbol{x}_1\boldsymbol{x}_1^T} - \frac{\overline{\boldsymbol{x}_1}\,\overline{\boldsymbol{x}_1}^T}{\overline{1}})^{-1}, \\ \boldsymbol{b} &= -\frac{A\overline{\boldsymbol{x}_1}}{\overline{1}} + \frac{\overline{\boldsymbol{x}_2}}{\overline{1}}. \end{aligned} \tag{6}$$

3 Global Projection Transformation Correlation

Affine transformation is a special kind of the 2D projection transformation, so I propose extending the GAT correlation method to the GPT method.

2D projection transformation is given by

$$\boldsymbol{x'} = \frac{A\boldsymbol{x} + \boldsymbol{b}}{1 + \langle \boldsymbol{c}, \boldsymbol{x} \rangle}. \tag{7}$$

Here, $\langle \boldsymbol{c}, \boldsymbol{x} \rangle$ means the inner product between $\boldsymbol{c}$ and $\boldsymbol{x}$. I divide this function into the affine transformation part and

the partial projection transformation (PPT) part as follows:

$$\boldsymbol{x'} = A\boldsymbol{x} + \boldsymbol{b} \quad (8)$$

$$\boldsymbol{x'} = \frac{\boldsymbol{x}}{1 + \langle \boldsymbol{c}, \boldsymbol{x} \rangle} \quad (\equiv P(\boldsymbol{x})) \quad (9)$$

A and $\boldsymbol{b}$ can be calculated by the method introduced in Section 2. Therefore, I just need to calculate the factor $\boldsymbol{c}$.

The function $f_p(\boldsymbol{x})$ which is transformed by the partial projection transformation is given by

$$f_p(\boldsymbol{x}) = \left|P^{-1}(\boldsymbol{x})\right| f(\frac{\boldsymbol{x}}{1 - \langle \boldsymbol{c}, \boldsymbol{x} \rangle}), \quad (10)$$

where, $\left|P^{-1}(\boldsymbol{x})\right|$ is the Jacobian of $P^{-1}(\boldsymbol{x})$.

First, I substitute $f_p(\boldsymbol{x})$ into (1). Next, I also introduce the Gaussian window function and the edge direction function to get the objective function. Finally, the objective function is given by

$$C_{\mathrm{PPT}}(f, g) = \iint_{\boldsymbol{K}} G(\frac{\boldsymbol{x}_1}{1 + \langle \boldsymbol{c}, \boldsymbol{x}_1 \rangle} - \boldsymbol{x}_2) \\ \delta(\nabla f(\boldsymbol{x}_1), \nabla g(\boldsymbol{x}_2)) f(\boldsymbol{x}_1) g(\boldsymbol{x}_2) d\boldsymbol{x}_1 d\boldsymbol{x}_2. \quad (11)$$

I set the derivation of C_{PPT} by $\boldsymbol{c}$ to zero. The factor $\boldsymbol{c}$ can be calculated as follow:

$$\boldsymbol{c} = (\overline{\langle \boldsymbol{x}_1, \boldsymbol{x}_2 \rangle \boldsymbol{x}_1 \boldsymbol{x}_1^T})^{-1} (\overline{\langle \boldsymbol{x}_1, \boldsymbol{x}_1 \rangle \boldsymbol{x}_1} - \overline{\langle \boldsymbol{x}_1, \boldsymbol{x}_2 \rangle \boldsymbol{x}_1}) \quad (12)$$

To determine the optimal GPT factors, I use the successive iteration method. As for the whole algorithm, I calculate the affine transformation part and the partial projection transformation part alternatively until the correlation becomes maximum. Then, output the maximal correlation value as the final result.

4 Experiment Result

In the experiment, I used gray-scale images. These pictures are taken by iPhone 5. I set the first shot as the original image. I obtain the target images by changing the angle of the actual shooting. First I match the target image with the original image and calculate the original correlation value between the two images. Then I adopt the GAT and GPT correlation methods to match the original and the target images. Finally I obtain the new correlation values and generate the transformed images of the target image.

Figures 1 and 2 show examples of original, target, and transformed images. Table 1 shows the values of original, GAT and GPT correlations. I measure the approximated parameter of projection transformation with a protractor. From the results, it can be seen that each correlation value using GAT and GPT was increased. Especially for the projection transformed images, the GPT correlation method is more effective than the GAT correlation method.

(a) Original (b) Target (c) GAT Trans. (d)GPT Trans.

Figure 1: Rotation Transformation

(a) Original (b) Target (c) GAT Trans. (d)GPT Trans.

Figure 2: Projection Transformation

Table 1: Correlation Values of Projection Trans.

Projection Trans.	original Cor.	GAT Cor.	GPT Cor.
c=(0,0.014)	0.858192	0.973581	0.990416
c=(0,0.026)	0.866167	0.943556	0.980527
c=(0,0.050)	0.703475	0.867848	0.919415
c=(0,0.060)	0.624939	0.818526	0.879993

5 Conclusion

In this paper, I propose to use the GPT correlation method for the gray-scale image matching. The validity of the method has been verified.

For the case of large deformation, the GPT correlation value has no significant increse. In order to achieve a more stable matching, it is necessary to improve the process. Also, for future work, the interrelationship between GAT and PPT is needed to be specified.

References

[1] T. Wakahara and Y. Yamashita, "Acceleration of GAT correlation for distortion tolerant image matching," Proceedings of the 21st International Conference on Pattern Recognition (ICPR 2012), Tsukuba, Japan, Nov.11-15, pp.746-749, (2012).

[2] M. Yasuda, K. Yamamoto, and H. Yamada, "Effect of the perturbed correlation method for optical character recognition," Pattern recognition, Vol.30, No.8, pp.1315-1320 (1997).

[3] T. Wakahara,Y. Kimura and A. Tomono, "Affine-invariant recognition of gray-scale characters using global affine transformation correlation," IEEE Trans. on, Pattern Analysis and Machine Intelligence, Vol.23, No.4, pp.384-395 (2001).

Central pressure drop underneath embankments caused by basal settlement
（基礎の沈下によって引き起こされる盛土中央の圧力減少）

Student Number: 10B17333 Name: Junichiro NAKAMURA Supervisor: Thirapong PIPATPONGSA

1 Introduction

After the Great East Japan Earthquake occurred on 11 March 2011, earthquake-induced damages of levees and reclaimed lands were largely reported. According to the investigation of the failure characteristic of levees summarized by Tohoku Regional Development Bureau of MLIT, damages caused by liquefaction of the foundation ground would involve basal settlement and saturated condition of loosening construction materials inside levees submerged under water.

This study aims to highlight that initial stress states influenced by passive arch action across a basal deflection plays a dominant role in the mechanisms of weakening resistance against liquefaction and will contribute to embankments stability evaluation against earthquakes. Arching effect influences to both initial stress states before liquefaction and failure condition of embankments with excessive basal settlements after liquefaction.

The scope of this study is restricted to static condition, not including dynamics, saturated condition and liquefaction, in order to focus on the initial stress condition due to arching after basal settlement. Therefore, 1G physical models of embankment made of dry sand with constant unit weight γ inclined at angle of repose ϕ is focused in the present study.

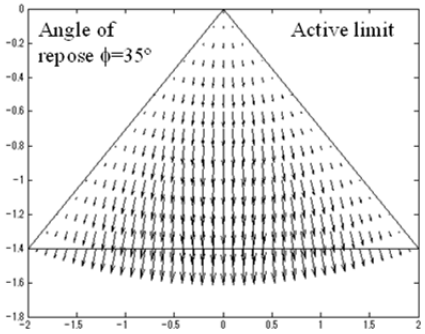

Figure 1: Trajectories of major principal stresses under active condition

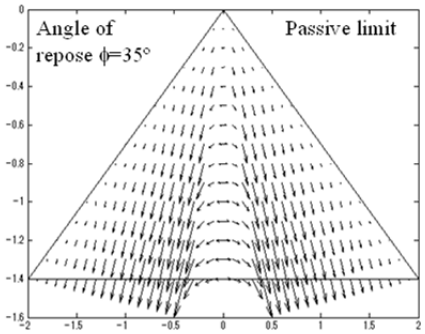

Figure 2: Trajectories of major principal stresses under passive condition

2 Literature review

States of stresses in a sand heap when a whole mass reaches the plastic state are bounded by two limits of active and passive conditions. Paths of compressive forces transferring to the base are shown in Fig.1 under an active condition and Fig.2 under a passive condition. If the vertical stress is greater than the horizontal stress along the centerline, a sand heap is in the active condition. Oppositely, if the horizontal stress is greater than the vertical stress, a sand heap is in passive condition. The previous works [1-3] have revealed that the deflection of the heap base causes the appearance of the central pressure drop. As the basal deflection is permitted to increase, the central pressure drop beneath the embankment significantly increased which was agreed well with the passive limit solution.

3 Apparatus

Dimension of in-house manufactured load frame made of aluminum channel is shown in Fig.3. Movable rack was designed to control vertical movements in up and down directions induced by actuator using screw jack with a belt linked to low-speed synchronous motor (SMK014K-A) 60 rpm (24VAC/50Hz) as shown in Fig.4. Dial gauge (DDP-50A) with a maximum range 45 mm was attached to a semi-sphere roller. Four miniature pressure gauges (P325S-02) were attached on a 10-mm-thick acrylic plate. Hinge laid along the center of acrylic plate allowed basal deflection up to 40 mm with a constant speed of 0.042 mm/minute.

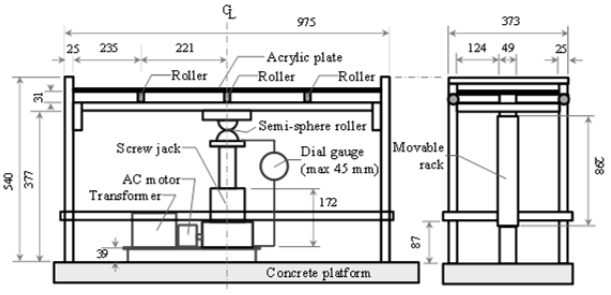

Figure 3: Plan of in-house manufactured load frame

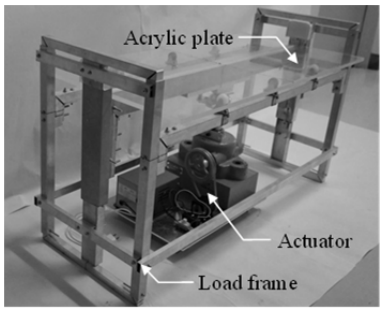

Figure 4: Photo of load frame and actuator

4 Materials and experiments

Two types of sand, silica sand no.6 and no.8, were used to build embankment. Physical properties of silica sand No.6 (D_{50}=0.316 mm) and No.8 (D_{50}=0.090 mm) are summarized in Table 1. Interface friction between silica sand no.6 and Acrylic plate is 18º and that of between silica sand no.8 and Teflon sheet (PTFE) is 24º.

Number of experiments was 15, starting from Test 1-11 using silica sand no.6 and the rest using silica sand no.8. Pressure gauges were placed on a base of acrylic plate for Test 1-4 but embedded flush to the surface of Teflon sheet for the rest. Embankment was built by pouring dry silica sand from the sieve source of sand spreader with a constant pouring height to the apex. Sand was generally deposited on the base with constant pouring height 100 mm, except Test 7 and Test 8 to check its effect at different heights. Flow rate and sweep rate of a sand spreader was controlled at 0.04-0.06 kg/s and 5.28 mm/s, respectively. Angle of repose was measured by an angle meter at sliding surfaces for every round of sand deposition. Height during construction of sand heap was measured by a laser meter. Density was measured by density pans (1.2 mm thick, 10 mm tall, 22 mm inner diameter). Changes of soil pressure were measured at a rate of 1 Hz. Yielding in embankment was produced by settlements and uplifts of the stiff base physically hinged together at the center. Three groups of experiments were considered which are Test 1-4, Test 5, 6, 9, 10 and Test 12-15, each of which was settled with different conditions of maximum settlement and hysteretic reversals as summarized in Table 2.

5 Results and conclusions

To address discussion about active and passive limits due to settlement and reversals, the passive pressure profiles after the final settlement to 10 mm when sand yielded (about 6.5% of the height of the sand heap) and the active pressure profiles after the final uplift to the level were considered. Though hysteretic reversals were applied in experiments, the relevant results in non-dimensional features were reasonably consistent with the theoretical active and passive limits based on sand heap with angle of repose 35º as shown in Figs.5-7. In general, as the basal deflection was slightly increased, the central pressure significantly decreased. Once the base was upturned, the central pressure gradually increased. Therefore, a central pressure drop caused by passive arch action could potentially reduce the resistance against liquefaction of embankments constructed on a deformable ground.

Table 1: Physical properties of silica sand No.6, No.8

Silica sand	Specific gravity	Minimum/Maximum density (kN/m^3)		Friction angle
No.6	2.643	12.17	15.26	41º
No.8	2.637	11.31	15.24	35º

Table 2: Conditions of experiments

№	Sand	Base	Pouring height	Settlements
1	Silica sand no.6	Acrylic	100 mm	45 mm
2				45 mm
3				10 mm × 3
4				2.5, 5, 10 mm
5		Teflon		40 mm
6				40 mm
7			50 mm	40 mm
8			200 mm	40 mm
9			100 mm	10 mm × 3
10				2.5, 5, 10 mm
11				2.5, 5, 5 mm
12	Silica sand no.8			40 mm
13				40 mm
14				10 mm × 3
15				2.5, 5, 10 mm

Note: Test 1&2, Test 5&6, Test 12&13 were conducted under the similar conditions to check the reproducibility of experiments. Reversal uplifts were applied to all tests back to the horizontal level at the end of each test.

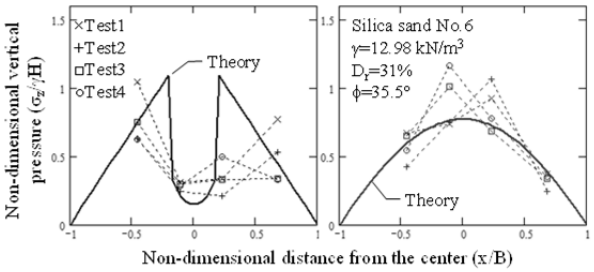

Figure 5: Passive and active pressure for Test 1-4

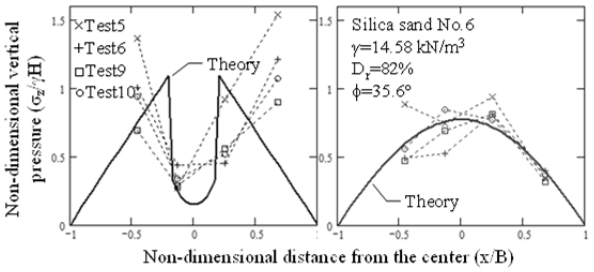

Figure 6: Passive and active pressure for Test 5,6,9,10

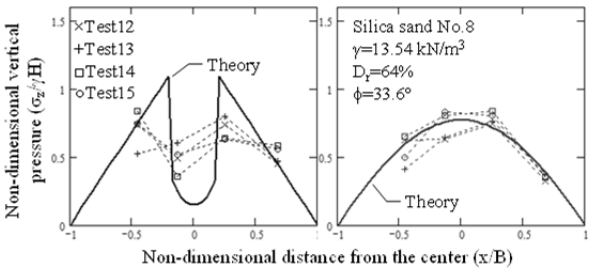

Figure 7: Passive and active pressure for Test 12-15

Reference

[1] Booker, J.R., "Applications of the theories of plasticity to cohesive frictional soils", Ph.D. Thesis, University of Sydney, 1969.

[2] Trollope, D.H., "The stability of wedges of granular materials", Ph.D. Thesis, University of Melbourne, 1956.

[3] Michalowski, R.L., Park, N., "Admissible stress fields and arching in piles of sand", Geotechnique 54 (8), 529-538, 2004.

Quantitative evaluation of the antimicrobial activity of the silver ion

Student Number: 10-19697 Name: Takuya HIBIO Supervisor: Kiyohiko NAKASAKI

1 Introduction

Silver has been known as a kind of disinfectant and is used widely in many applications such as consumer products and medical supplies. However, the quantitative evaluation of the efficiency of the antimicrobial activity of the silver ion has not been carried out extensively in contrast to other disinfectants such as chlorine, ozone, chloramine and ultraviolet. [1] Generally, to evaluate the efficiency of the disinfection, the Chick-Watson model shown below has been employed [2].

$$Ln(N/N0) = AC^{n}t \quad (1)$$

(N/N0: survival ratio, A: Chick-Watson coefficient of specific lethality, C: concentration of disinfectant (mg L^{-1}), n: coefficient of dilution, t: time (min))

In the equation (1), it is known that the value of n can be assumed to be 1 in many cases.

But, Chick-Watson has not been used in the evaluation of antimicrobial activity of the silver ion. Therefore, we tried to conduct the fitting of experimental data with this model to confirm the applicability of the model for disinfection by the silver ion. The dependency of the antimicrobial activity of the silver ion on the temperature was also evaluated using Arrhenius equation.

In addition, the resistance of the spore to the antimicrobial activity of silver ion and the relation between the disinfection efficiency and the classification of the bacteria by gram staining were evaluated in this study.

2 Materials and methods

2-1 Bacterial strains

Four bacterial strains, *Escherichia coli* K12 W3110 and *Pseudomonas aeruginosa* PAO1 as gram-negative bacteria, and *Staphylococcus gallinarum* BPT1 and *Bacillus subtilis* TB5 as gram-positive were used in this study.

2-2 Cultivation of bacteria

E. coli K12 was incubated in 5 mL of Luria-Bertani broth at 37°C for 18 hours. And the other bacterial strains were incubated in 5 mL of Trypticase-soy broth at 30°C for 18 hours. To enhance the sporulation of *B. subtilis* TB5, *B. subtilis* TB5 was incubated in 40 mL of the TS broth added with manganese sulfate at 30°C for 1 week.

2-3 Disinfection test

All bacterial strains cultivated in the medium were centrifuged at 2400 g for 5 min. Then, the supernatant was removed and the precipitated cells were resuspended in the HEPES-NaOH buffer (pH=7.0) to remove residual medium. This washing procedure was repeated 3 times. And the cell suspension was inoculated to 40 mL of HEPES-NaOH buffer. To investigate the effect of the concentration of silver, silver nitrate was added to the buffer containing *E. coli* K12cell suspension at the final concentration of 0.05, 0.08, 0.1 and 0.2 mg-Ag L^{-1}. To evaluate the effect of reaction temperature on the antimicrobial activity of the silver ion, the buffer containing *E. coli* K12cell suspension was incubated at 5, 15, 25 and 35°C. During the incubation, the 1mL of samples were withdrawn and the cell density was determined by the dilution plating method.

3 Results and discussion

3-1 Antimicrobial activity of silver ion

Generally, the disinfection activity was formulated by Eq. (2).

$$dN/dt=-kN \quad (2)$$

(N: the concentration of microorganism (CFU mL^{-1}), t: time (min), k: the inactivation rate constant (min^{-1}))

Therefore, the concentration of microorganism decreased exponentially. Fig. 1 shows the courses of the survivability of *E. coli* K12 during the incubation with different concentrations of silver ion. The inactivation rate constants corresponding to the silver ion concentrations were obtained as the slope of the approximate lines. The inactivation rate constants at the silver ion concentrations of 0.05, 0.08, 0.1 and 0.2 mg-Ag L^{-1} were 0.0033, 0.015, 0.047 and 0.092 (min^{-1}), respectively.

Fig. 2 shows the relation between the silver ion concentration and the inactivation rate constants. Then we tried fitting of this data with the Chick-Watson model. But, the result of the fitting was not satisfactory. It was considered that the threshold concentration exists in the antimicrobial activity by silver ions. Therefore, we modified the Chick-Watson model, as follows:

$$k=-A(C-C_{thr}) \quad (3)$$

(C_{thr}: the threshold concentration (mg-Ag L^{-1}))

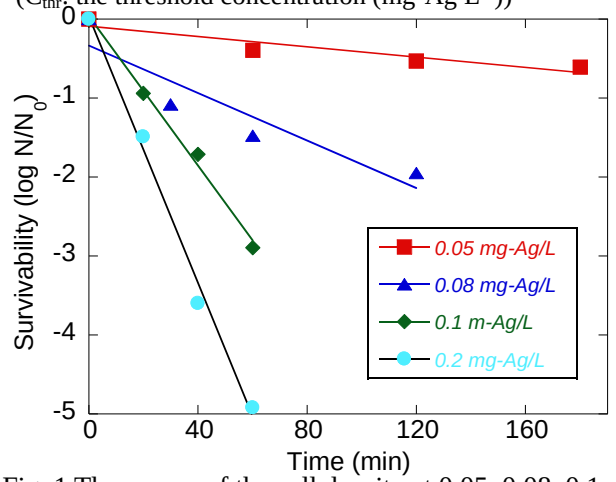

Fig. 1 The course of the cell density at 0.05, 0.08, 0.1 and 0.2 mg-Ag mL^{-1}

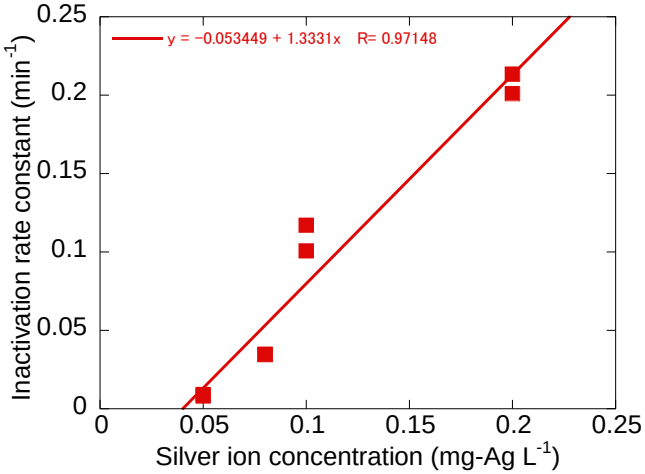

Fig. 2 The inactivation rate constants at 0.05, 0.08, 0.1 and 0.2 mg-Ag L^{-1}

3-2 Effect of the temperature on the antimicrobial activity

The inactivation rate constants at 5, 15, 25 and 35°C where the silver ion concentration was 0.1 mg-Ag L^{-1} were determined based on the change in the cell density of *E. coli* K12 during the incubation and they were 0.010, 0013, 0.047 and 0.066 (min^{-1}), respectively. Then, the activation energy of the disinfection by the silver ion was determined using Arrhenius equation as 50 kJ.

This value of activation energy is similar to that of the general chemical reaction. The activation energy for reaction of the disinfection by the sodium hypochlorite was approximately 45-80 kJ and it was revealed that the temperature dependency of the disinfection effect of silver ion was similar to that of the sodium hypochlorite.

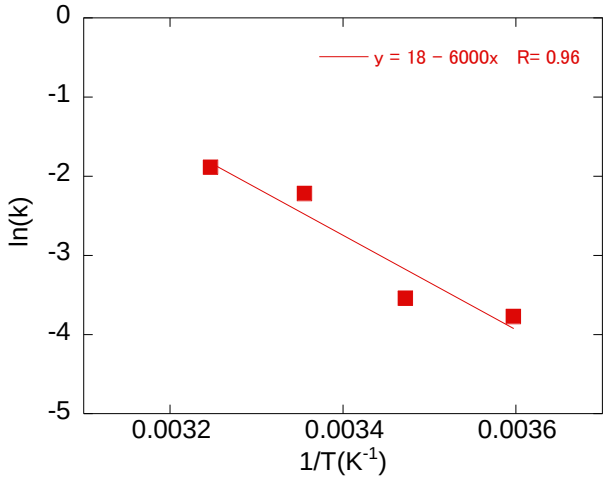

Fig. 3 The arhenius plot for the disinfection by silver ion

3-3 Comparison of the resistances to the silver ions between the spore and the vegetative cell

Generally, spores are much more resistant to the disinfectants such as chlorine compared to the vegetative cells [3]. And the resistance of the spore to the silver ion was examined in this study.

Fig. 3 shows the courses of the survivability of the spore and the vegetative cell of *B. subtilis* TB5 during the incubation with the silver ion of 0.01 mg L^{-1}. No bactericidal effect to the spore was observed in 1h incubation, while the survivability of the vegetative cells decreased after 1 h incubation. After 20 min of incubation, decrease of the survivability of the vegetative cell was not significant and it was considered that the initial culture of the vegetative cell contained small

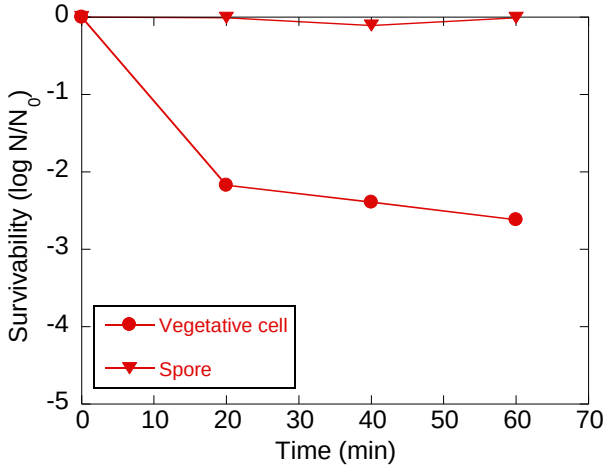

Fig. 4 The survivability of vegetative cell, spore of B. subtilis

portion of spores of which resistance to the silver ion was reflected as the little decrease of the survivability after 20 min.

3-4 Difference in the disinfection effects to the gram–positive bacteria and gram-negative bacteria

Gram-positive bacteria have only a peptidoglycan cell wall while gram-negative bacteria have both a thin peptidoglycan cell wall and an outer membrane layer. The outer membrane layer acts as an extra barrier, thereby, gram-negative bacteria show higher resistance to many disinfectants than gram-positive bacteria.

Fig. 5 compares the courses of the survivability of *E. coli* K12, *P. aeruginosa* PAO1, *S. gallinarum* BPT1 and *B. subtilis* TB5 during the incubation with the silver ion at the concentration of 0.1 mg L^{-1}. The inactivation rate for *S.gallinarum* BPT1, *B. subtilis* TB5, *E. coli* K12 and *P. aerugionsa* PAO1 were determined as 0.023, 0.11 (0-20 min), 0.047 and 0049 (min^{-1}), respectively. The results indicated that the resistance to the silver ion was independent to the classification by the gram staining.

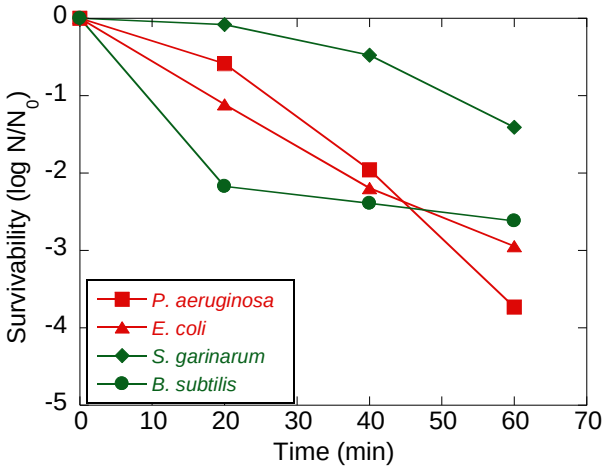

Fig. 5 The survivability of *P. aeruginosa* PAO1, *E. coli* K12, *S. gallinarum* BPT1 and *B. subtilis* TB5

4 Conclusions

It was revealed that the antimicrobial activity of the silver ion could not be expressed by Chick-Watson model and the modified model was proposed.

The activation energy for the disinfection by silver ion was determined as 50 kJ using Arrhenius equation.

The spore were high resistant to silver ions and the antimicrobial activity of the silver ion was considered not to be related with the classification of bacteria by gram staining.

References

[1] US Environmental Protection Agency, Disinfection Profiling and Benchmarking Technical Guidance Manual. Office of Water, EPA 816-R03-004, (2003)

[2] Fariba Amiri et al.: Disinfection effectiveness of organic chloramines, investigating the effect of pH, Water Research, 44, 845-853

[3] Gerald McDonnell et al.: Antiseptics and Disinfectants: Activity, Action, and Resistance, Clinical Microbiology Reviews, 43, 147-179, (1999)

汎用ソフトウェア無線機を用いた電波伝搬測定装置の開発

学生番号：10B20039　名前：ビン　テンヨウ　指導教員： 高田潤一，金 ミンソク

1　研究背景と目的

無線通信において伝搬路特性はシステム設計を行うための重要な情報である．受信信号は伝搬路を通して距離減衰されるばかりではなく，反射や回折，散乱などにより多重波の影響を受ける．これらの特性を測定するために高分解能を持つ測定装置が必要となる．現在，伝搬路測定に用いられる測定装置は高価かつ大型であり，伝搬路測定実験は非常に高い費用がかかり，利便性も低いとの問題がある [1].

そこで本研究では汎用ソフトウェア無線機（Universal Software Radio Platform) を用いて伝搬路測定装置を開発し，その妥当性に関する検証を行った．本装置は，汎用の測定装置に比べて，安価かつ小型であり，通常の専用装置に比べて，RF 周波数が選択可能であることから柔軟性が優れている．

2　汎用ソフトウェア無線機開発環境

汎用ソフトウェア無線機とは USRP(Universal Software Radio Peripheral) というハードウェア開発環境と GNU Radio というフリーソフトウェアで構成される．

2.1　ハードウェアの構造

図 1 のように，USRP はメインボードとドーターボードで構成され，PC から転送された複素ベースバンド信号は補間処理後，ディジタルアップコンバージョン (DUC:Digital-Up-converter) により中間周波数（IF) に周波数変換され，高速 D-A 変換機（分解能 16 ビット，サンプリングレート 400MS/s) により複素 IF 送信信号としてドーターボードの RF アップコンバータ回路に入力される．

一方，中間周波数における複素 IF 受信信号は，高速 A-D 変換器（分解能 16 ビット，サンプリングレート 100MS/s) によりサンプリングされ，FPGA においてデジタルダウンコンバージョン（DDC:Digital Down Conversion) により，DC 領域への周波数変換が行われ，最終的に複素ベースバンド信号に変換される [2].

2.2　汎用ソフトウェア無線機の制約

USRP と GNU Radio を用いることでソフトウェア無線機を容易に実現できるが，USRP の性能上いくつの制約が知られている．現在，RF ドーターボードは，DC から約 6GHZ までの広い周波数帯を選択できる．PC と USRP 間の最大転送レートは，ギガビットイーサネットの場合，200MByte/s である．しかし，PC と USRP は，4Byte の I/Q サンプルをやり取りするため，最大ナイキスト帯域幅は 25MHz に制限される．

USRP のメインボード上の FPGA では PC インタフェースの転送速度に応じて A-D 変換された複素 IF 信号のレート変換を行う．レート変換は 4 − stage CIC フィルタと 32 タップのハーフバンド低域フィルタにより行われるが，伝達関数のロールオフ特性によりスペクトル両端に歪みが生じる問題がある．加えて，USRP の RF ドーターボードからの最大出力電力は 20dBm で，

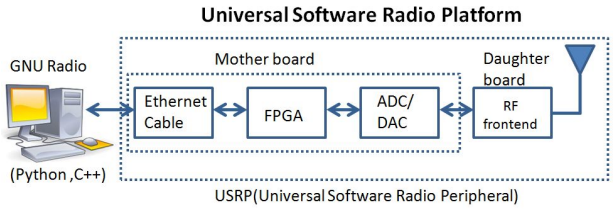

Figure 1: 汎用ソフトウェア無線機の開発環境

測定機のダイナミックレンジはこの出力電力により制限される．

3　本研究のアプローチ

3.1　送信信号

本研究の送信信号はマルチトーン信号である，マルチトーン信号は次式で表現される

$$s(t) = \frac{1}{\sqrt{N}} \sum_{k=-N/2}^{N/2} \exp(\mathrm{j}2\pi k \Delta_F t + \mathrm{j}\phi_k) \qquad (1)$$

ここで，N はサブキャリアの数，Δ_F はサブキャリアスペーシング，ϕ_k はニューマンフェースである．そして，この信号帯域内の全周波数成分が等電力を持ち，一様なスペクトラムの形をするため，伝搬測定信号に適している．

3.2　送受信プログラムの開発とシステムの構築

本研究では GNU Radio を用いて送受信を制御するプログラムを開発した．GNU Radio の最上位階層はスクリプト言語としては Python を用いる [3]．信号処理においてブロックの入出ポートを接続することにより簡単に記述できる．

送受信システムの構築として送信信号（マルチトン信号）は最初に送信 PC で作成され，送信プログラムを介して送信 USRP に送られる．そして送信 USRP から変調した RF 信号を送信する．一方，受信側では伝搬路を通って伝わってきた信号を受信 USRP で受信し，復調する．受信信号は受信 PC に送られ，ファイルとして保存される．

3.3　データ処理

保存された生データから，伝達関数とインパルス応答が計算される．受信した信号は MATLAB 上で信号処理をされる．伝搬路の伝達関数とインパルス応答を計算し，伝搬路特性を求める．信号処理の流れは次のようになる．伝搬路を通して受信された信号は次式で表現される．

$$y(t) = \int h(\tau) s(t-\tau) d\tau + w(t) \qquad (2)$$

ここで，$s(t)$ は送信信号，$h(\tau)$ はインパルス応答，$y(t)$ は受信信号，$w(t)$ は受信機の熱雑音を表す．この式を

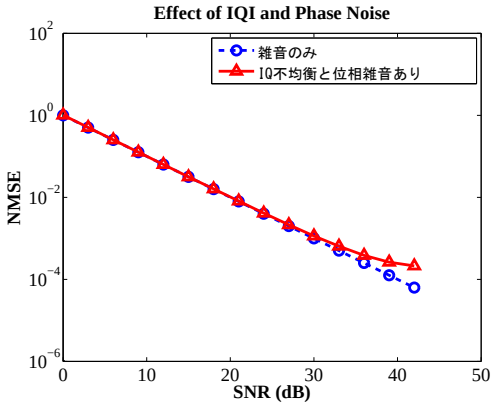

Figure 2: IQ 不均衡と位相雑音評価

フーリエ変換し，周波数領域で表現すると，次式となる．

$$Y(f) = H(f)S(f) + W(f) \tag{3}$$

上の式の両辺を $S(f)$ で除算することにより，伝達関数 $H(f)$ が求まる．さらに $H(f)$ を逆フーリエ変換をすることにより，インパルス応答 $h(\tau)$ は求められる．

3.4 同期

本章で主に同期の手法を説明する．周波数の同期は，高安定ルビジウム原子時計を基準として送信機と受信機の局部発信機を動作させることで達成し，送受信間キャリア信号の周波数オフセットを解消した．

一方，波形の送受信タイミングの同期はルビジウム原子時計の Pulse Per Second(PPS) 信号を USRP 送受信機に接続することにより実現した．PPS 信号は 1 秒周期の高精度の信号であり，送信波形が繰り返して挿入された丁度 1 秒の長さを持つパケットを送信機の PPS 信号の立ち上がりを基準として繰り返し送信し，受信機も同様に PPS 信号を基準としてデータをキャプチャーすることで，送受信間絶対同期を達成した．

3.5 校正と評価

RF 回路の不具合により I/Q 信号の不均衡と位相雑音が伝送特性を劣化させる原因として問題とされる．I/Q 信号の不均衡は補償により除去されるが、位相雑音は確率的な現象のため，なるべく高精度の局部発信機を用いる必要がある．本研究では、測定機の I/Q 不均衡を GNU radio 自動補償のプログラムで補償した．そして，補償後の I/Q 不均衡と位相雑音を測定し，NMSE(Normalized Mean Square Error) を用いてチャンネル推定性能をシミュレーションで評価した [4]．図 2 に結果を示す．I/Q 不均衡と位相雑音により NMSE が多少大きくなるが，運用範囲における影響は無視できることが確認できた．

4 検証実験

測定機の性能を確かめるため，図 3 のような T 型の試験回路を用いて検証実験を行った [5]．実験におけるパラメーター設定は表 1 に示す．この試験回路のインパルス応答を USRP サウンダとネットワークアナライザ (VNA) の両方で測定し，その結果の比較を行い、装置の性能を評価した．図 4 に T 型試験回路のインパルス応答を示す．この結果より，本装置で測定された直接波，遅延波のタイミングが VNA の結果と一致していることが確認できる．

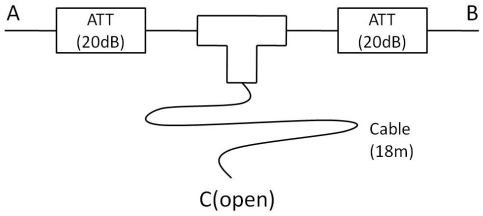

Figure 3: T 型試験回路

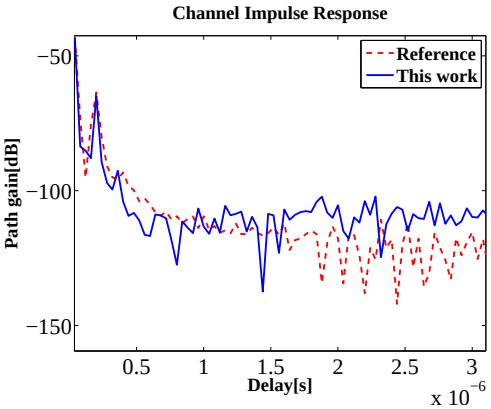

Figure 4: チャンネルインパルス応答

Table 1: パラメーターの設定

周波数	2.4GHz
帯域幅	25 MHz
サンプルレート	25MSps
遅延解像度	40ns
送信電力	20dBm

5 まとめ

本研究は汎用ソフトウェア無線機を用いて，安価で広い RF 周波数に対応する伝搬測定装置を開発した．そして，T 型の試験回路を用いて測定装置の性能を検証し，VNA と同様に伝達関数の取得が可能であることを示した．今後の研究では，様々な環境における実環境での伝搬実験を実施する予定である．

文　　献

[1] D. Mass, M. H.Firooz, J. Zhang, N. Patwari and K.Kasera, “Channel sounding for the masses: low complexity GNU 802.11b Channel Impulse Response Estimation, ” *IEEE Trans. Wireless Commun*, VOL, 11, No.1, Jan. 2012.

[2] 金　ミンソク，アズリル. ハニズ，“ オープンソースソフトウエア無線プラットホーム GNU Radio Gnu radio Open Software Defined Radio Platform ”，電気電子情報通信学誌，Vol. 96，No. 1. Jul. 2013.

[3] M. Gahadza, M. Kim, J. Takada, “Implementation of a Channel Sounder using GNU Radio Opensource SDR Platform, ” 信学技報，SR2008-94，Mar. 2009.

[4] M. Kim, J. Takada, Y. Konishi , “Novel Scalable MIMO Channel Sounding Technique and Measurement Accuracy Evaluation With Transceiver Impairments” *IEEE Trans. Instrum.Meas*, VOL, 61, No.12 , Dec. 2012.

[5] S. Kobayashi, M. Kim, J. Takada, “Development of measurement system for Body Area Network by UWB, ” Dept. of International Developemnt Engineering, Tokyo Institute of Technology, Japan, Mar. 2012.

Temperature effect on adhesion hysteresis of elastic contact between silicon rubber and glass lens

Student Number: 10_20045 Name: Guanda FU Supervisor: Kunio TAKAHASHI

1 Introduction

Adhesion of polymer is focused to develop grip-and-release devices recently[1]. Adhesion hysteresis is a phenomenon which is defined as the difference between attaching and detaching process caused by the energy lost at the interface. Understanding the mechanism of adhesion hysteresis is important to control and use adhesion.

Adhesion hysteresis is more obvious in experiments of polymer that it is first observed by Pascal Silberzan[2] using JKR model[3]. Adhesion tests of polymer have been carried out by many researchers[4, 5] and mechanism of adhesion hysteresis has been discussed using JKR theory[3] by the assumption of energy equilibrium. However, the mechanism of adhesion hysteresis has not been clarified. In our laboratory, the mechanism of adhesion hysteresis has been studied by calculating the energy dissipation[6]using JKR test with the consideration the stiffness of the measurement system[7] and make a conclusion that the energy lost at the edge of the contact area is a constant value by unit length. The problem is that the test is carried out only in one temperature and effect of temperature on adhesion hysteresis has not been studied. In the present study, a JKR test has been conducted between silicone rubber and silica glass lens in several temperatures to find the effect of temperature on adhesion hysteresis.

2 Theory

The JKR model with the considering of the stiffness of the measurement is shown in Fig.1 and we use a spring to demonstrate the stiffness of the external force measurement. Relationship between the radius of contact area a, external load F, displacement Z_t and other parameters is shown in the following expression:

$$F = \frac{2Eak}{(1-\nu^2)k + 2Ea}\left(Z_\mathrm{t} - \frac{a^2}{3R}\right) \qquad (1)$$

where E is Young's modulus of silicone rubber, R is the radius of curvature, ν is Poisson's ratio, k is the stiffness of measurement system.

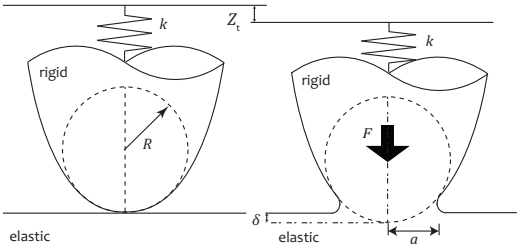

Fig. 1: JKR model with the consideration of the stiffness of the system

The external work U_external, the elastic energy from the deformation U_elastic, the interface energy $U_\mathrm{interface}$, and the lost energy $U_\mathrm{dissipation}$[6]can be expressed as Eq.(2).

$$\begin{aligned}\Delta U_\mathrm{external} &= \Delta U_\mathrm{elastic} + \Delta U_\mathrm{interface} \\ &\quad + \Delta U_\mathrm{stiffness} + \Delta U_\mathrm{dissipation} \qquad (2)\end{aligned}$$

3 Experiment

3.1 Material and devices

The schematic of experimental apparatus is shown in Fig.2. All of the devices is installed on a vibration isolation table(SIGMAKOKI). The external load F, radius of contact area a and displacement Z_t are measured simultaneously.

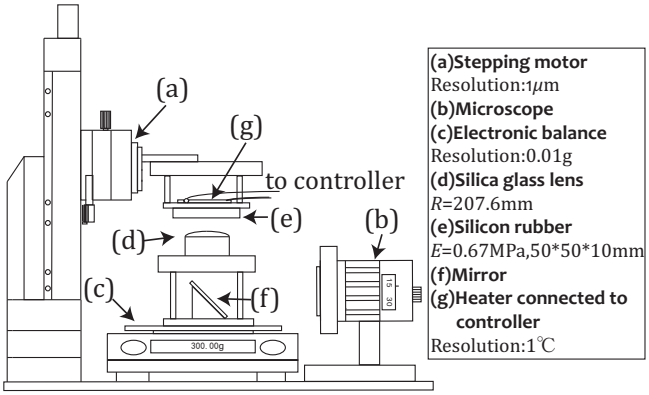

Fig. 2: Schematic illustration of the experimental apparatus

3.2 Experimental procedure

The adhesion experiments were conducted as the surface temperature of silicon rubber at 20°C, 40°C, 60°C. The surface temperature of silicone rubber is measured by a infrared thermometer. For the case of 20°C(room temperature), the experiment can be done without a heater. For the case of 40°C and 60°C, the surface temperature of silicone rubber becomes stable 30 minutes after turn on the heater. And the adhesion test is carried out after waiting for an other 30 minutes.

The stepping motor is operated to load and unload the silicon rubber with the a percision of 1μm per step. The displacement is set to zero when the silicone rubber start contacting the lens. There are 30 steps of loading process and we unload the silicon rubber until it detached from the glass lens. The duration of waiting time between each step is 60 seconds.

3.3 Results and discussion

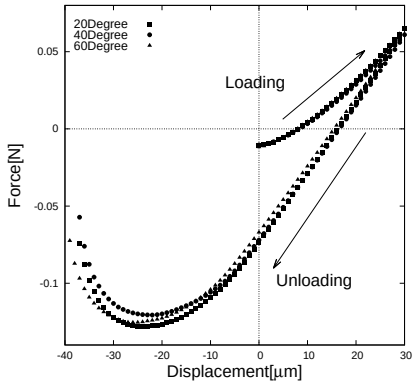

Fig. 3: Relationship between external force and displacement

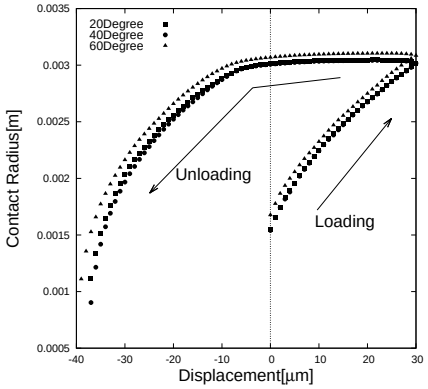

Fig. 4: Relationship between contact radius and displacement

The both loading, unloading passes have little difference between each temperature as shown in Fig.3 and Fig.4. The energy dissipation is calculated using Eq.(2). and Fig.5 shows the energy dissipation at the edge of contact area per unit length for each temperature. The energy dissipation is 0 in loading process and it is nearly a constant value in unloading process when the radius of contact area start to decrease. No differences can be seen between the three temperatures in both loading and unloading process. We can conclude that the adhesion hysteresis between silicone rubber and glass lens is independent to temperature from 20°C to 60°C.

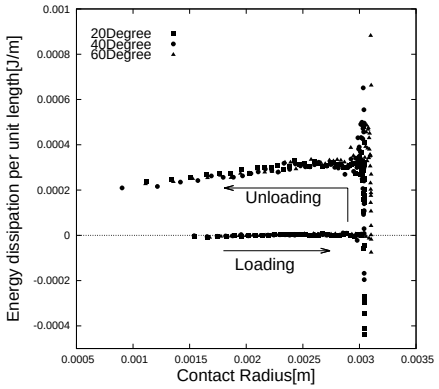

Fig. 5: Energy dissipation per unit length at each temperature

4 Conclusion

The adhesion test using JKR model with the measurement stiffness is done. The external force and contact radius is measured. The energy dissipation is calculated and it is independent to temperature from 20°C to 60°C. We can conclude that temperature from 20°C to 60°C has no effect on adhesion hysteresis between silicone rubber and glass lens.

References

[1] Y.Sekiguchi, et al., *J. Adhesion Sci. Technol.*, Vol.26, No.23, pp.2615-2626(2012)

[2] P. Silberzan, et al., *Langmuir* 10,pp.2466-2470(1994)

[3] K. L. Johnson, et al., *Proc. R. Soc. London A* 324, pp.301-313(1971)

[4] N. Amouroux, et al., *Langmuir* 19, 1396 (2003)

[5] P. R. Guduru, et al., *J.Mechanics and Physics of solid* 55,pp.473-488(2007)

[6] D. Baek, et al., "Mechanism of adhesion hysteresis in the elastic between a silicone rubber and a silica glass lens", a master thesis of Tokyo Institute of Technology(2013)

[7] K. Takahashi, et al., *J.Adhesion Sci.Technol.*, Vol.9, No.11, pp.1451-1464(1995)

Tsunami Run-up Simulations for Complex Terrain

Student Number：10_22133 Name：Koki Matsumoto Supervisor：Hiroshi Takagi

1. Introduction

By The 2011 Earthquake of the Pacific Coast of Tohoku and Tsunami that occurred on 14:46 March 11st in 2011, the number of the dead or missing casualties reached 18,524 people, and the number of the building which had been completely destroyed or partially destructed was 3,909,284 units (as of Feb 2014). According to the tidal record at Ayukawa Station [1], 8.6 m tsunami was observed and the resultant flood extended 73 km^2 in Ishinomaki City [2].

Ishinomaki was one of the most affected areas, where more than 3,000 people died. Inhabitants in Ishinomaki also experienced The Chilean Tsunami which generated 2-3 m tsunami in 1960. However, this past experience may have led to people's underestimation against the tsunami in 2011 which greatly exceeded the 1960 tsunami.

Given the complex geographical feature of Ishinomaki which encompasses both flat and hilly terrains with port, industrial area, residential area, agricultural land, canal, man-made forest belt, sea dike, natural beach, river, and many other land types, it is obvious that the inundated tsunami traveled over the land in complicated paths. In this study, a tsunami run-up analysis was performed and compared with the measured tsunami heights and inundation areas in order to assess the applicability of the model for such complex terrain.

2. Field Survey

In order to perform the numerical analysis precisely, the GSI terrain data set was used as mentioned later. Besides, the authors carried out a field survey for three days in March 2013 to measure the elevations of sea dike and river bank which generally do not appear in the terrain data of publicly available, but should have a great influence on the simulation results. A set of high-precision GPS was used to measure these elevations, and the data was finally corrected by a neighboring electronic reference point's data. It is recognized that this measurement and correction can achieve accuracy at order of several centimeters.

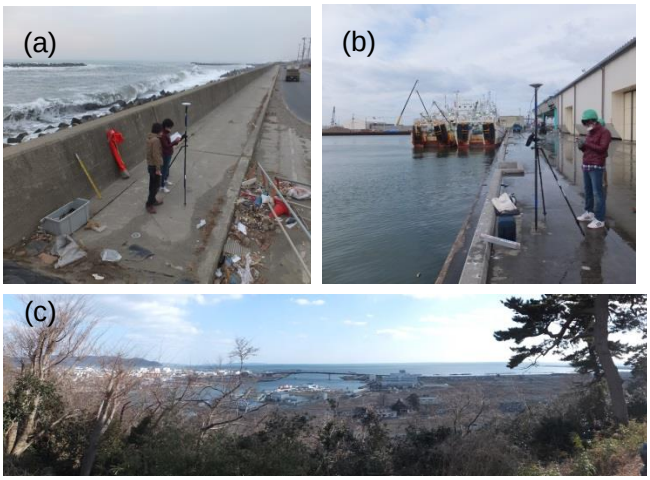

Fig.1 (a) (b) Scene of land survey, (c) Devastation of Ishinomaki, photo taken from Hiyoriyama Park (March, 2013)

3. Tsunami Run-up in Ishinomaki

A series of numerical simulations were performed to evaluate tsunami run-up over the lands of Ishinomaki Area immediately after the Great East Japan Earthquake happened on March 11, 2011. Actual water elevations measured off the coast of Miyagi and Fukushima by the GPS buoy system were employed as the offshore boundary of the largest domain (Fig.2). The other numerical settings are shown in Table.2.

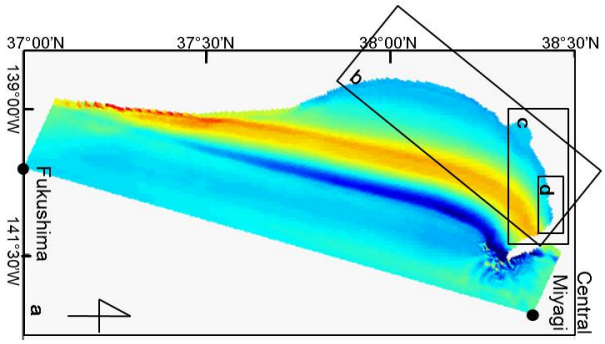

Fig.2 Computational domains. Smallest one (d) focuses on Ishinomaki with a fine resolution

Table2. Calculation Settings

item	
Calculating area	Largest mesh(540m square mesh)
	Second mesh(180m square mesh)
	Third mesh(60m square mesh)
	forth mesh(20m square mesh)
Wave	the 2011 earthquake of the Pacific coast of Tohoku and tsunami
Time step	Δt=0.1sec
Tide level condition	Mean sea-level of Tokyo Bay (T.P.+0.0m)
Computation time	2011/3/11 15:15～2011/3/11 17:00
Bathymetric data	Largest mesh: JODC 500m data
	Second mesh: JODC 500m data
	Third mesh: JODC 500m data
	Forth mesh: プレジャーボート・小型船用港湾案内
Ground levels	It creates from 5m mesh data of Geographical Survey Institute
Relative roughness	0.025 is uniformly set to a water area
	0.02 is uniformly set to a agricultual area
	0.06～0.15 is uniformly set to a housing area
	0.15～0.25 is uniformly set to a factory area

Table3. Locations in Ishinomaki at which comparison is made

Name	latitude	longitude	number
Ishinomaki gaikou	38.423	141.269	A
Ishinomaki port	38.413	141.324	B
Iharatsu	38.422	141.336	C
Mitsumata	38.429	141.273	D
Minamihama	38.416	141.305	E
Nakase	38.428	141.311	F
Ishinomaki Nippon paper	38.414	141.287	G
Ishinomaki sensyuu university	38.450	141.294	H
Shinhigashimaenuma	38.435	141.263	I
Yado	38.449	141.319	J
Nishiyamamachi	38.434	141.294	K
Midorimachi	38.418	141.336	L
Minatomachi	38.427	141.314	M

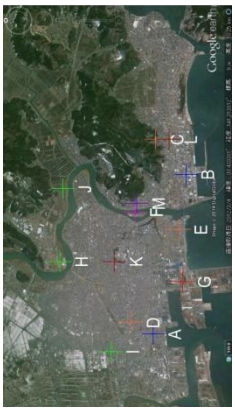

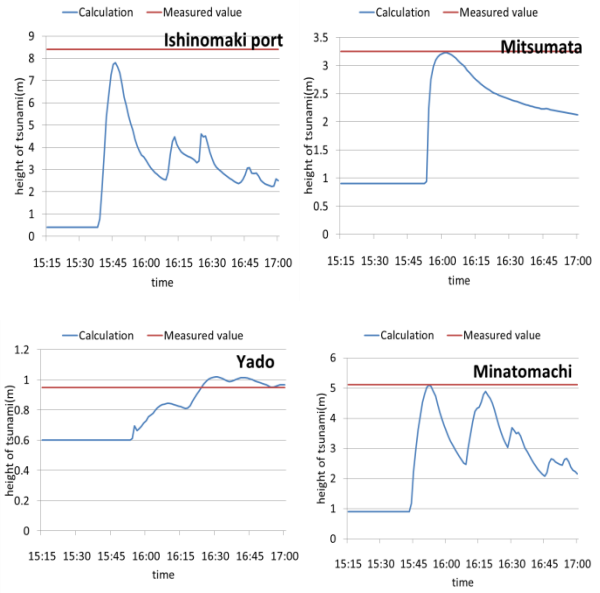

Fig.3 water levels (blue: simulation, red: measurement [3])

Tsunami inundation heights and area were compared between the simulation results and the measured data [3] at totally 13 points (Table.3), which are located in different land types such as port and factory areas (A, B, G, M), residential area (C, D, E, K, I, L), agricultural land (H, J) and river side (F).

Fig.3 shows the simulated water levels (blue) from the sea level at 15:00 on March 11th at selected points, along with the measured heights (red). All of the figures in Fig.3 show that the difference in maximum tsunami height between calculation and measurement is considerably small. According to Fig.4 which represents flood areas by both simulation and observation [3], the simulated tsunami reaches a maximum distance of 4.5 km from the coastline and shows a good agreement with the observed area.

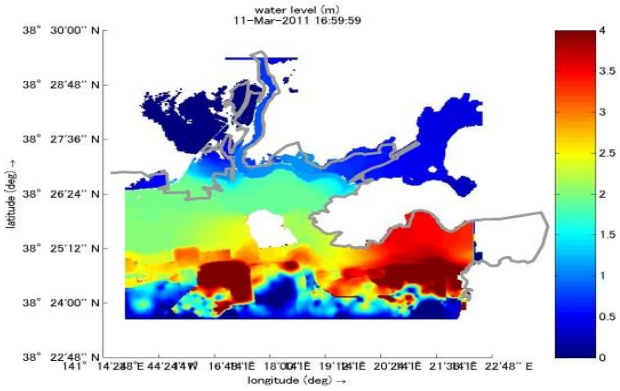

Fig.4 Inundation areas in Ishinomaki (colored area: present simulation, gray line: observation by the survey [3])

4. Conclusion

Numerical simulation is indispensable in order to estimate a future possible tsunami. In the present research, the numerical simulation was performed to assess the applicability of the model for the lands with complex terrain and multiple land use. The authors has corroborated that complex behavior of tsunamis over the lands can be adequately estimated by the numerical model, using the GSI terrain data modified by the high-precision GPS survey on coastal and river structures and the recorded tsunami data by the GPS buoy system as offshore boundary.

References

[1] Japan Meteorological Agency: http://www.jma.go.jp/jma/press/1106/03b/

[2]Geospatial Information Authority of Japan: http://www.gsi.go.jp/common/000059939.pdf

[3] Detailed Maps of the impacts of 2011 Japan Tsunami Vol.1: Aomori, Iwate and Miyagi, T. Haraguchi, A. Iwamatsu, 2011

Study on Application of Water Supply Curing System to Electro-chemical Repair

ID: 10-25210 Name: Shu YAMAMOTO Supervisor: Prof. Nobuaki OTSUKI

1. Introduction

"Water Supply Curing System[1)]" is one of the reliable methods for curing of concrete. This system can provide water film on the surface of concrete.

On the other hand, electro-chemical repair[2)] is one of repair methods which can repair reinforced concrete deteriorated due to steel corrosion. Applying these methods to reinforced concrete with steel corrosion, corrosion environment around steel bars, such as existence of chloride ion or low pH, can be recovered without concrete replacement or human error.

Here it is necessary to provide the external solution on concrete surface in the case of applying electro-chemical repair to reinforced concrete, however there are some problems in conventional water supplying systems such as panel system or cellulose fiber system. Panel system needs holes on concrete to keep the system, and the method can apply only to flat surface. Cellulose fiber system generates a lot of dust, and the appearance is not good during repairing.

If Water Supply Curing System can apply to electro-chemical repair, above problems can be solved. So the applicability of Water Supply Curing System to electro-chemical repair was investigated in this study. Especially below issues were investigated.

1) To clarify the influence of solution quantity and distance between anode and concrete on the resistance of chloride ion penetration after repairing (*mortar specimen*).
2) To investigate the applicability of Water Supply Curing System to electro-chemical repair (*real reinforced concrete beam taken from existing structure*).
3) To evaluate the repair effect of electro-chemical repair with Water Supply Curing System (*deteriorated reinforced concrete exposed for 40 years under marine environment*).

2. Experimental procedure

2.1 Specimen

1) Mortar specimen

The size of mortar specimens was 40mm× 40mm×160mm. They were used for investigation of influence of the solution quantity and distance between anode and specimen on repair effect.

2) Real reinforced concrete beam

The real reinforced concrete beam taken from existing structure was 13 m of length and its cross-section is I- shape.

3) Reinforced concrete exposed for 40 years

Concrete specimens with 150mm×300mm× 1800mm were repaired using Water Supply Curing System using the obtained condition in above two reinforced mortar or concrete. Specimens used here had been deteriorated under tidal zone for 40 years.

2.2 Evaluation

Effect of repair was evaluated from four points of view.

① Improvement of resistance to permeation of chloride ion
② Crack sealing effect
③ Desalination effect
④ Protecting effect against corrosion of steel bar

2.3 Repair method

1) Repair conditions

Table 1 shows conditions selected by previous research. Table 2 shows repair pattern applied to reinforced concrete specimen exposed for 40 years.

2) Supplying water by Water Supply Curing System

Picture.1 shows the view of Water Supply Curing System. Pump and hose supply water evenly from tank to concrete surface. Water flows between sheet and concrete surface. Suction machine makes negative pressure between sheet and concrete, and prevent fall of sheet. Suctioned water returns to tank.

Table 1 Repair conditions.

Solution	$Mg(CH_3COO)_2$ aq
Concentration	0.1mol/L
Current density	1.0A/m^2
Period	2weeks

Table 2 Repair pattern on RC exposed for 40 years.

No	System	Anode	Distance (mm)
1	WSCS	Titanium	0
2	WSCS	Carbon fiber	0
3	WSCS	Carbon fiber	10
4	WSCS	Conductive sheet	0
5	Submersion	Titanium	20

WSCS: Water Supply Curing System.

Picture 1 View of Water Supply Curing System.

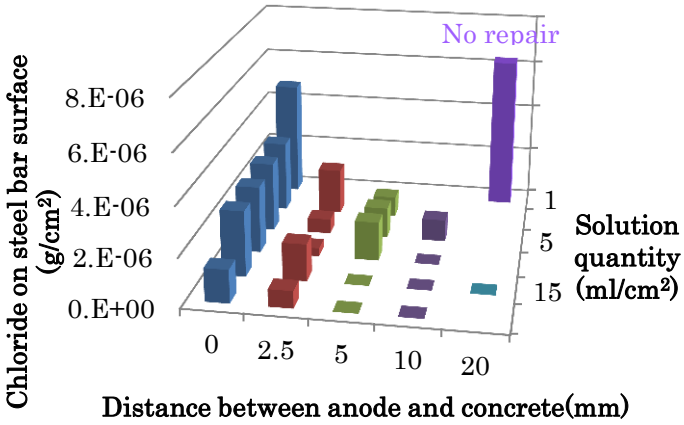

Fig.1 Decrease of chloride on steel bar surface after submersion (Mortar specimen)

3. Experimental result

3.1 Resistance to permeation of chloride ion

Fig.1 shows the decrease of chloride on steel bar surface by submersion in 3.5wt% salt water for a week after repairing, compared with no repair. As the solution quantity become larger, or distance between anode and concrete become larger, resistance to permeation of chloride ion become larger.

3.2 Application method

Water Supply Curing System was improved in two points shown below.

- Always pumping
- Increase the suction power

And the usable anode materials were selected from the viewpoint of applicability and price as shown in Table.3. In this way, Water Supply Curing System got applicability to electro-chemical repair.

3.3 Repair effect

Crack sealing effect of repair using Water Supply Curing System was almost same that of submersion condition when titanium was used as anode as shown in Fig.2. Even if carbon fiber was used, the equal effect was gotten by giving space between anode and concrete. That is thought in case of conductive sheet.

Fig.3 shows the increase of chloride quantity in solution during repairing, that means removed chloride quantity from the concrete. Desalination effect of repair using Water Supply Curing System is almost same that of submersion condition.

Fig.4 shows corrosion rate of main reinforcement and stirrup. Although default rates vary widely, protecting effect against corrosion of steel bar is gotten in repair using Water Supply Curing System like that of submersion condition.

Table.3 Selection of the most usable anode

Anode	Applicability	Price (yen/m^2)	Evaluation
Non-separated titanium	△	15000	△
Separated titanium	○	15000	○
Stainless	△	2000	△
Thick rubber	○	90000	×
Thin rubber	×	120000	×
Conductive sheet	×	500	×
Carbon fiber	○	6000	○

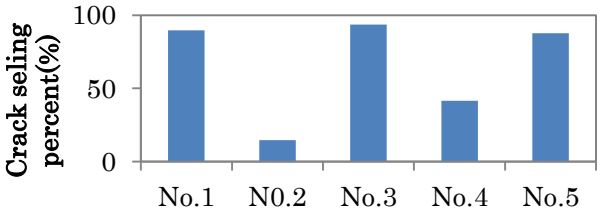

Fig.2 Crack sealing effect (Concrete specimen)

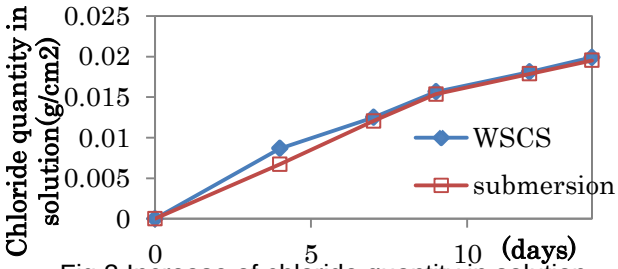

Fig.3 Increase of chloride quantity in solution (Concrete specimen)

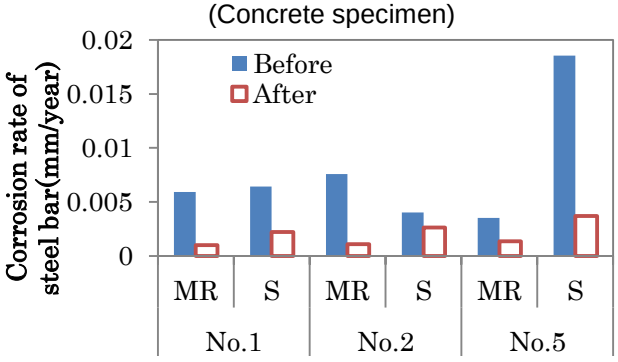

MR: Main Reinforcement, S: stirrup

Fig.4 Protecting effect against corrosion of steel bar (Concrete specimen)

4. Conclusions

From the results of present study, it can be said that Water Supply Curing System is applicable as the solution supply system of electro-chemical repair effectively. Also following conclusions were obtained.

1) Applicability of Water Supply Curing System to electro-chemical repair was confirmed using real reinforced concrete taken from existing structure, and then proper anode materials such as separated titanium or carbon fiber sheet was selected.
2) When titanium was used as anode, repair effect of Water Supply Curing System was almost same with that of submersion condition.
3) As the solution quantity become larger, or distance between anode and concrete become larger, resistance to permeation of chloride become larger.

5. Reference

1) Hazama Ando Corporation: Water Supply Curing System of Concrete Structure, “Aqua Curtain”;2013.4
2) Japan Society of Civil Engineers: Recommendation for Design and Construction of Electrochemical Corrosion Control Method; 2001.11